

**Block Copolymer Micellar Thin Films as Templates for the Production of
Tunable Inorganic Nanocluster Arrays and Their Applications**

by

RYAN DEREK BENNETT

Bachelor of Science in Chemical Engineering
Department of Chemical Engineering
University of Florida, Gainesville, Florida, 2002

Submitted to the Department of Chemical Engineering
in partial fulfillment of the requirements for the degree of

DOCTOR OF PHILOSOPHY IN CHEMICAL ENGINEERING

at the

MASSACHUSETTS INSTITUTE OF TECHNOLOGY

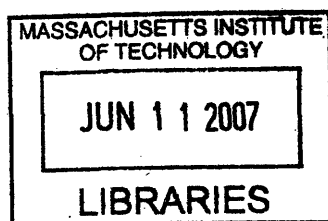
JUNE 2007

© 2007 Massachusetts Institute of Technology. All rights reserved.

Signature of Author: _____
Department of Chemical Engineering
May 24, 2007

Certified by: _____
Robert E. Cohen
St. Laurent Professor of Chemical Engineering
Thesis Advisor

Accepted by: _____
William M. Deen
Carbon P. Dubbs Professor of Chemical Engineering
Chairman, Committee for Graduate Students



ARCHIVES

Block Copolymer Micellar Thin Films as Templates for the Production of Tunable Inorganic Nanocluster Arrays and Their Applications

by

Ryan Derek Bennett

Submitted to the Department of Chemical Engineering on May 24, 2007
in partial fulfillment of the requirements for the degree of
Doctor of Philosophy in Chemical Engineering

Abstract

In the past decade, the use of self-assembling systems for the fabrication of materials on the nanometer scale has been an active area of research. Block copolymer thin films are a subclass of self-assembling systems that have received considerable attention due to their intrinsic nanometer feature size, their ease of synthesis, and their rich phase behavior. While block copolymer thin films have been utilized in a variety of applications, including the nanofabrication of substrates, the modification of surface properties, and the synthesis of photonic structures, this thesis will focus on using the self-assembling properties of block copolymer thin films to synthesize inorganic nanocluster arrays. These arrays have a wide range of possible applications in fields such as catalysis, data storage, and nanofabrication.

This thesis demonstrates a general route for using block copolymer micellar thin films as templates to synthesize tunable inorganic nanocluster arrays. The approach utilized amphiphilic block copolymers, such as poly(styrene-*block*-acrylic acid) and poly(styrene-*block*-2-vinylpyridine), to create micelles in solution that could be selectively loaded with metal ions and deposited onto a substrate to create quasi-hexagonal arrays of nanoclusters. Various strategies were successfully developed to tune the size and areal density of the nanoclusters, thereby affording a level of control that is unique relative to the standard routes for synthesizing inorganic nanocluster arrays. The strategies included the variation of the block copolymer molecular weight, the addition of polystyrene homopolymer into the micellar solution, and the mixing of different micellar solutions.

The block copolymer micellar system was utilized to create iron oxide nanoclusters, which were catalytically active in the thermal chemical vapor deposition growth of carbon nanotubes (CNTs). Through appropriate selection of the substrate and the reaction conditions, vertical CNT growth was achieved. By uniformly varying the areal density of iron oxide nanoclusters on the substrate surface, the morphology of the CNT films was manipulated from a tangled and sparse arrangement of individual CNTs, through a transition region with locally bunched and self-aligned CNTs, to rapid growth of thick vertical CNT films. Through a microcontact printing approach, nanocluster arrays were patterned on a micron scale to synthesize patterned vertical growth of CNTs. To demonstrate the generality of this approach, the block copolymer micellar system was also used to synthesize gold nanocluster arrays for fabricating DNA arrays via Supramolecular Nano-Stamping (SuNS).

Thesis Supervisor: Robert E. Cohen, St. Laurent Professor of Chemical Engineering

Acknowledgements

Throughout graduate school I have had the good fortune of interacting with an amazing collection of individuals. Without each of their unique contributions, my thesis as a whole would certainly not have been possible.

First and foremost, I would like to sincerely thank my advisor, Professor Robert E. Cohen. In any graduate education, the relationship between the advisee and the advisor is a key component of the learning process. Having been advised by Professor Cohen throughout my graduate career, I can say with certainty that I owe much of my success to the relationship that we have established. While Professor Cohen possesses all of the traits that one would look for in an advisor, his unbridled enthusiasm for research is what I believe makes him unique as an advisor. During my doctoral thesis project, there were many periods of excitement as well as difficulty. During these challenging periods, Professor Cohen's enthusiasm and encouragement were instrumental in my research progress. Professor Cohen has truly been a tremendous advisor for me and I feel extremely fortunate to have had the opportunity to work with him.

I would also like to thank my committee members, Professor Karen K. Gleason, Professor Paula T. Hammond, and Professor Ken Beers for their time and assistance throughout my graduate studies. My thesis has benefited significantly from their discussions and insightful suggestions.

This thesis was only possible due to the many collaborators that I was fortunate enough to work with. I would like to thank Professor Zhifeng Ren and Guangyong "Bear" Xiong from Boston College for agreeing to use our catalyst system in their carbon nanotube reactors, which resulted in the work presented in Chapter 2. I would also like to sincerely thank Anastasios John Hart for all of his help over the years. After meeting through a chance encounter, we managed to create a collaboration that has lasted more than two years and is still going strong today. John's immense knowledge of the carbon nanotube field and his many insightful suggestions were an invaluable part of my thesis work. The work with John makes up Chapters 4 and 5 of this thesis. I would also like to thank Professor Francesco Stellacci and Ozge Akbulut of the DMSE at MIT for their collaboration in creating DNA nanoarrays. This work appears in Chapter 6 of this thesis. I would also like to thank the group of "wild Indians" that made up the SAXS characterization collaboration, including Ben Wang, Eric Verploegen, and A. J. Hart. I am grateful for the opportunity to have been included in the collaboration and I always enjoyed our "brainstorming" sessions at the Muddy. This work appears in Appendix A of this thesis.

I would also like to thank the former and current members of the Cohen Group. From day one, I have had nothing but positive interactions with each and every member of the group. I'd like to acknowledge everyone who has had an immediate impact in my work, including Andy Miller, Adam Nolte, Daeyeon Lee, Ben Wang, Sharon Soong, Prem Pavor, Gary Chia, Roger Aronow, Yonathan Thio, Jeff Abes, Russell Gorga, Giovanna Machado, and Heejae Kim. I would also like to thank Yot Boontongkong, whose research I expanded upon during my thesis work. Working with each of these individuals on a daily basis has made my research project a truly enjoyable and rewarding experience.

I would also like express my gratitude to the various staff members at MIT that have helped me along the way. Thanks to Mike Frongillo, Dr. Anthony Garratt-Reed, Libby Shaw, and Tim McClure for their help on various instruments at MIT. I also appreciate the amazing administrative support that I received from Suzanne Easterly, Mary Wesolowski, Iris Chang, Jen Shedd, Annie Fowler, Greg Sands, and Mary Keith. I am also grateful for the help Carrie

Casado, Alina Haverty, and Danielle Delgado have given me.

Throughout my graduate experience I have been absolutely amazed by the people I have met and the friendships that have been formed. While the learning in the classroom was significant, I have no doubt that I have gained even more from interactions with my colleagues. Looking back, I certainly feel fortunate to have been a part of the Class of 2002 (best class ever??). The breadth of interests and the range of personalities within our class is truly remarkable.

I would like to begin by thanking the lunch crew of Beez, EA, Wally, Pockets, and Tmon; they have all been great friends who have shaped my graduate experience. Whether it was spades (and “No, Joe, No”), PMMA (and the plug of chance), or WC (and the Frosties), they have always kept me leaving lunch in the right frame of mind. Graduate school would not have been the same without the friendship of each of these people. I would also like to thank the bbhedge. It was the experience of a lifetime, and I truly thank everyone who made this possible. I would like to give special thanks to Wickman, KC, and the Monkey Test.

I would also like to give thanks to the many people who made graduate school a more enjoyable place over the years, including ACM (for dealing with sitting next to me for the past 3 years), Sharon, KWood, Mox (for co-founding the Cruisers), Shuga, Shannan, Jane, Jake, Theis, Sty, Corey (and his Sour Apple), BradC, Mike, Daryl, Sanj, Loose, Bernat, Beckham, Micah, Rocco, Deep Blue, Pregibon, Krogdome, EV, A.J. Hart, and the entire BPT. I also appreciate everyone who organized and participated in ChemE intramural activities, including the MIT Octathon Champions of 2005. I would also like to mention “The tradition unlike any other” (Ski Trip), which was a welcome relief during the cold winter months.

I met some amazing individuals outside of MIT who made my stay in Boston all the more enjoyable. These people include Kim, Will, Andrea, Gui, Ryan, Jenn, Andrea, Erin, and many others. I also want to thank everyone who has been a part of FNG over the years. After being introduced to ultimate a little late in life, I have had a fantastic time learning the game and playing with this group of people for the last 3 years.

I would like to express my love and gratitude for my parents, F. Vernon and Gayle Bennett. I have the utmost appreciation for everything my parents have done for me throughout my life. As I have grown older, I have become distinctly aware of the sacrifices my parents made to put my needs and interests ahead of their own. I am extremely grateful to have them as parents and I can only hope to become a fraction of the parent that they have been to me. I would also like to thank my sister, Ashley, who has continually supported and encouraged me along the way.

Finally, I would like to thank my wife, Yvonne. Words do not begin to describe my love and appreciation for her. This thesis would most certainly not have been possible without her. I feel truly blessed to have found someone with whom I can share the rest of my life. I look forward to the future knowing that Yvonne will be by my side.

TABLE OF CONTENTS

LIST OF FIGURES	7
LIST OF TABLES	12
<i>Chapter 1: Introduction</i>	13
1.1. Block Copolymers and Their Properties	13
1.2. Micellar Behavior of Block Copolymers.....	14
1.3. Patterning of Inorganic Nanoclusters via Block Copolymers	16
1.4. Applications for Inorganic Nanocluster Arrays.....	18
1.4.1. Catalysts for Carbon Nanotube Synthesis	18
1.4.2. Templates for Synthesizing DNA Nanoarrays	19
1.5. Thesis Outline.....	20
1.6. References.....	21
<i>Chapter 2: Using Block Copolymer Micellar Thin Films as Templates for the Production of Catalysts for Carbon Nanotube Growth</i>	27
2.1. Introduction	27
2.2. Experimental Section.....	29
2.2.1. Materials.....	29
2.2.2. Sample Preparation.....	30
2.2.3. Microscopy	33
2.3. Results.....	33
2.3.1. Catalytic Substrates	33
2.3.2. Carbon Nanotube Growth	36
2.4. Discussion.....	41
2.4.1. Catalytic Substrates	41
2.4.2. Carbon Nanotube Growth	42
2.5. Conclusion	47
2.6. References.....	48
<i>Chapter 3: Strategies for Controlling the Planar Arrangement of Block Copolymer Micelles and Inorganic Nanoclusters</i>	50
3.1. Introduction	50
3.2. Experimental Section.....	52
3.2.1. Materials.....	52
3.2.2. Sample Preparation.....	53
3.2.3. Microscopy and Spectroscopy.....	56
3.3. Results and Discussion	56
3.4. Conclusion	77
3.5. References.....	78
<i>Chapter 4: Controlling the Morphology of Carbon Nanotube Films by Varying the Areal Density of Catalyst Nanoclusters Using Block Copolymer Micellar Thin Films</i>	80
4.1. Introduction	80
4.2. Experimental Section.....	82
4.2.1. Materials.....	82
4.2.2. Preparation of Carbon Nanotube Growth Catalysts	83
4.2.3. Carbon Nanotube Growth Procedure	83
4.2.4. Characterization.....	84
4.3. Results and Discussion	84
4.4. Conclusion	99
4.5. References.....	101

<i>Chapter 5: Patterning of Block Copolymer Micellar Thin Films Using Microcontact Printing and Their Applications in Carbon Nanotube Synthesis</i>	103
5.1. Introduction	103
5.2. Experimental Section	106
5.2.1. Materials	106
5.2.2. Sample Preparation	107
5.2.3. Characterization	109
5.3. Results and Discussion	110
5.3.1. Microcontact Printing of Block Copolymer Micellar Thin Films	110
5.3.2. Carbon Nanotube Growth from Patterned Catalysts	119
5.4. Conclusion	123
5.5. References	124
<i>Chapter 6: DNA Printing Using Au Nanocluster Arrays Synthesized via Block Copolymer Micellar Thin Films</i>	127
6.1. Introduction	127
6.2. Experimental Section	128
6.2.1. Materials	128
6.2.2. Sample Preparation	129
6.2.3. DNA Printing Procedure	130
6.3. Results and Discussion	132
6.4. Conclusion	142
6.5. References	143
<i>Chapter 7: Conclusions</i>	145
7.1. Summary of Thesis Contributions	145
7.2. Recommendations for Future Work	147
<i>Appendix A: Characterization of Carbon Nanotube Thin Films Synthesized from Block Copolymer Micellar Thin Film Catalysts using Small Angle X-Ray Scattering</i>	151
<i>Appendix B: Synthesis of Zinc Oxide Nanowires from Au Nanoparticle Arrays Created Using PS-b-PAA Micellar Thin Films</i>	159
<i>Appendix C: Patterning of Block Copolymer Micelles and Inorganic Nanoclusters via the Self-Assembly of PS-b-PMMA</i>	163
<i>Appendix D: Effects of Block Copolymer Micellar Thin Film Thickness on Inorganic Nanocluster Morphology</i>	172
<i>Appendix E: Comparisons Between the Loading of PS-b-PAA Micelles in Aqueous or Toluene Solution</i>	177
<i>Appendix F: Contrast of Various Metal Salts Loaded in PS-b-PAA Micellar Thin Films in TEM Imaging Using Si₃N₄ Substrates</i>	179

List of Figures

Figure 1-1. Structure of repeat units for poly(styrene- <i>block</i> -acrylic acid) (PS- <i>b</i> -PAA) and poly(styrene- <i>block</i> -2-vinyl pyridine) (PS- <i>b</i> -P2VP).....	16
Figure 2-1. AFM height image of non-cavitated PS- <i>b</i> -PAA thin film on a silicon nitride substrate.	31
Figure 2-2. Diagram illustrating the cavitation step caused by submerging the PS- <i>b</i> -PAA thin films in NaOH _(aq) solution.....	32
Figure 2-3. TEM image of Pb nanocluster array created from a non-cavitated thin film.	34
Figure 2-4. TEM images of iron oxide nanoclusters synthesized using: a) cavitated template; b) non-cavitated template.....	35
Figure 2-5. SEM images of 30 min CNT growth on an iron oxide nanocluster array created from a cavitated template: a) area of low CNT density on substrate; b) area of high CNT density on substrate.....	37
Figure 2-6. SEM image of 60 min CNT growth on an iron oxide nanocluster array created from a cavitated template: a) area of low CNT density on substrate; b) area of high CNT density on substrate.....	39
Figure 2-7. TEM images of 60 min CNT growth on an iron oxide nanocluster array created from a cavitated template.....	40
Figure 2-8. High-resolution TEM image of a multi-wall CNT grown from an iron oxide nanocluster on a silicon substrate.	41
Figure 2-9. TEM image of a 10 min CNT growth using iron oxide nanoclusters synthesized from a cavitated template on a silicon nitride substrate.....	46
Figure 3-1. Diagram of synthesis procedures for modification of block copolymer micellar thin films.	56
Figure 3-2. TEM images of iron oxide nanocluster arrays synthesized from micellar thin films using PS- <i>b</i> -PAA (16.4/4.5) with a FeCl ₃ loading ratio of: (a) 0.3; (b) 5.4; (c) 15.	58
Figure 3-3. Fe 2p XPS spectra for iron oxide nanocluster arrays synthesized from micellar thin films using PS- <i>b</i> -PAA (16.4/4.5) with a FeCl ₃ loading ratio of 5.4.....	60
Figure 3-4. O 1s XPS spectra for iron oxide nanocluster arrays synthesized from micellar thin films using PS- <i>b</i> -PAA (16.4/4.5) with a FeCl ₃ loading ratio of 5.4.	60
Figure 3-5. TEM images of iron oxide nanocluster arrays synthesized from micellar thin films with a FeCl ₃ loading ratio of 5.4 and PS- <i>b</i> -PAA with a molecular weight of: (a) 11/1.2; (b) 16.4/4.5; (c) 66.5/4.5.....	62
Figure 3-6. TEM images of iron oxide nanocluster arrays synthesized from micellar thin films using PS- <i>b</i> -PAA (16.4/4.5) with a FeCl ₃ loading ratio of 5.4 and a [PS : PS- <i>b</i> -PAA] equal to: (a) 0 (no PS homopolymer); (b) 4; (c) 10.....	66
Figure 3-7. TEM image of Pb-containing nanocluster array formed from combining a PbAc ₂ -loaded micelle solution with an unloaded micelle solution in a 1:1 volume ratio for 1 min and then spin casting onto a substrate.	68
Figure 3-8. Characterization of a nanocluster array formed from PS- <i>b</i> -PAA (16.4/4.5) copolymer with a FeCl ₃ loading ratio of 5.4: a) Bright field TEM image (scale bar ~ 100 nm); b) Annular dark field image obtained using STEM; c) Elemental Fe map obtained using EDX analysis with STEM; d) EDX spectra from nanocluster obtained using STEM.	70

Figure 3-9. Annular dark field image of multi-species nanocluster array formed by combining an FeCl ₃ -loaded micellar solution (loading ratio ~ 0.3) with a PbAc ₂ -loaded micellar solution (loading ratio ~ 0.9) for 2 min, along with spectrums from EDX analysis. ..	72
Figure 3-10. Annular dark field image of multi-species nanocluster array formed by combining an FeCl ₃ -loaded micellar solution (loading ratio ~ 0.3) with a PbAc ₂ -loaded micellar solution (loading ratio ~ 0.9) for 120 hr, along with EDX spectrums from individual nanoclusters.	73
Figure 3-11. Comparison of the composition of multi-species nanocluster arrays formed by combining an FeCl ₃ -loaded micellar solution (loading ratio ~ 0.3) with a PbAc ₂ -loaded micellar solution (loading ratio ~ 0.9) for 2 min vs. 120 hr before spin-casting.	74
Figure 3-12. Comparison of the composition of multi-species nanocluster arrays formed by combining an FeCl ₃ -loaded micellar solution (loading ratio ~ 0.3) with a PbAc ₂ -loaded micellar solution (loading ratio ~ 0.9) in a volume ratio of 1:9, 1:1, and 9:1..	76
Figure 3-13. Annular dark field image (scale bar = 70 nm) of multi-species nanocluster array formed by adding FeCl ₃ (loading ratio ~ 2.1) directly into a previously PbAc ₂ -loaded micellar solution (loading ratio ~ 0.9), along with EDX spectrums from individual nanoclusters.	77
Figure 4-1. TEM image of iron oxide nanoclusters on a Si ₃ N ₄ window grid prior to CNT growth.	85
Figure 4-2. SEM image of a CNT growth using 16 nm diameter iron oxide nanoclusters on Al ₂ O ₃ -coated Si with a flow rate of 100/500/200 sccm of C ₂ H ₄ /H ₂ /Ar at 750°C, where the inset shows a higher resolution SEM image demonstrating that the iron oxide nanoclusters do not coalesce during the growth process.	87
Figure 4-3. SEM image of a CNT growth using 16 nm diameter iron oxide nanoclusters on Al ₂ O ₃ -coated Si with a flow rate of 200/500/200 sccm of C ₂ H ₄ /H ₂ /Ar at 750°C (45° tilt).....	88
Figure 4-4. SEM image (85° tilt) of vertical CNT growth from 16 nm iron oxide nanocluster arrays created from a micellar monolayer of uniform thickness on Al ₂ O ₃ -coated Si after C ₂ H ₄ /H ₂ /Ar flow rates of 200/500/0 sccm at 750°C.....	91
Figure 4-5. Effects of varying iron oxide nanocluster areal density on morphology of CNT films.	94
Figure 4-6. HRTEM image of a typical MWCNT grown from micellar thin film catalysts..	96
Figure 4-7. Diameter distribution of CNTs grown from 16 nm iron oxide nanoclusters with an areal density of $6 \times 10^{10} \text{ cm}^{-2}$ on Al ₂ O ₃ -coated Si in 200/500/0 sccm C ₂ H ₄ /H ₂ /Ar at 750°C.....	97
Figure 4-8. SEM image (85° tilt) of the side view of a vertical CNT film grown from 16 nm iron oxide nanoclusters with an areal density of $6 \times 10^{10} \text{ cm}^{-2}$ on Al ₂ O ₃ -coated Si in 200/500/0 sccm C ₂ H ₄ /H ₂ /Ar at 750°C.	99
Figure 5-1. Schematic illustration of the μ CP of block copolymer micellar thin films using a PDMS stamp.	109
Figure 5-2. Optical microscope images of PS- <i>b</i> -PAA micellar thin films patterned using μ CP with a PDMS stamp with a feature width and periodicity of: (a) 1 μm and 2 μm , (b) 4.5 μm and 9 μm , and (c) 8 μm and 16 μm	111

Figure 5-3. Optical microscope images of PS- <i>b</i> -PAA micellar thin films patterned using μ CP with an applied pressure of 600 kPa and a PDMS stamp with a channel width of 5 μ m and a periodicity of 10 μ m.	113
Figure 5-4. AFM characterization of a PS- <i>b</i> -PAA micellar thin film patterned using a PDMS stamp having a channel width of 7 μ m and a periodicity of 14 μ m.	115
Figure 5-5. Optical microscope images of PS- <i>b</i> -PAA micellar thin films patterned using μ CP with a PDMS stamp of cylindrical posts with a removal velocity of 1 mm s ⁻¹ and with a diameter and periodicity of: (a) 4 μ m and 6 μ m, (b) 4 μ m and 10 μ m, and (c) 3 μ m and 18 μ m.	116
Figure 5-6. (a) Optical microscope image of a PS- <i>b</i> -PAA micellar thin film patterned using μ CP with an applied pressure of 600 kPa using a PDMS stamp of cylindrical posts with diameters of 4 μ m and a periodicity of 8 μ m and a removal velocity of 0.2 mm s ⁻¹ . (b) Optical microscope image of a PS- <i>b</i> -PAA micellar thin film patterned using μ CP with an applied pressure of 600 kPa using a PDMS stamp of cylindrical posts with diameters of 4 μ m and a periodicity of 10 μ m and a removal velocity of 1 mm s ⁻¹	118
Figure 5-7. SEM micrographs of vertically-grown MWCNT structures grown from an FeCl ₃ -loaded PS- <i>b</i> -PAA micellar thin film patterned onto an Al ₂ O ₃ -coated Si substrate using a μ CP approach with a channeled PDMS stamp with a width of 5 μ m and a periodicity of 10 μ m.	121
Figure 5-8. SEM micrographs of vertically-oriented MWCNT structures grown from an FeCl ₃ -loaded PS- <i>b</i> -PAA micellar thin film patterned onto an Al ₂ O ₃ -coated Si substrate using a μ CP approach with a PDMS stamp with cylindrical posts having diameters of 4 μ m and a periodicity of 8 μ m.	123
Figure 6-1. Diagram of DNA printing using block copolymer templated Au nanoclusters via SuNS.	131
Figure 6-2. TEM image of a gold nanocluster array created from PS- <i>b</i> -P2VP (81/21) with a gold loading ratio of 0.35.	132
Figure 6-3. AFM height image of: a) DNA hybridized gold nanoclusters made from PS- <i>b</i> -P2VP (81/21) on a Cr-coated Si substrate, and b) printed DNA strands on a gold substrate following dehybridization.	133
Figure 6-4. Radial distribution function of DNA hybridized gold nanoclusters on a Cr-coated Si substrate (left image) and printed DNA strands on a gold substrate following dehybridization (right image).	134
Figure 6-5. Diagram of possible route for synthesizing more complex DNA nanoarrays using block copolymer templated gold nanocluster arrays.	135
Figure 6-6. TEM images of gold nanocluster arrays created from PS- <i>b</i> -P2VP (325/92) with a gold loading ratio of: a) 0.1, b) 0.35, and c) 1.0.	137
Figure 6-7. TEM images of gold nanocluster arrays created from: a) PS- <i>b</i> -P2VP (16/3.5), b) PS- <i>b</i> -P2VP (81/21), and c) PS- <i>b</i> -P2VP (325/92) with a gold loading ratio of 0.35.	139
Figure 6-8. TEM images of gold nanocluster arrays created from PS- <i>b</i> -P2VP (325/92) with a gold loading ratio of 0.35 and a PS homopolymer (M _n = 115k) loading ratio of: a) No homopolymer added, and b) 20:1 [PS: PS- <i>b</i> -P2VP].	140
Figure 6-9. AFM height image of: a) ssDNA-hybridized gold nanoclusters on a Cr-coated Si substrate, and b) printed DNA strands on a gold substrate following dehybridization.	141

Figure 6-10. TEM images of gold nanocluster arrays created from PS- <i>b</i> -P2VP (81/21) with a gold loading ratio of 0.35 and H ₂ O loading ratio (number of H ₂ O molecules relative to the number of pyridine rings) of: a) No H ₂ O added, and b) 100:1.	142
Figure A-1. Diagram of the experimental setup for analyzing CNT thin films using SAXS characterization.	152
Figure A-2. SAXS intensities as a function of scattering vector for Sample 1 obtained by integrating over +/- 10 degree conical slices around $\phi = 180$ deg.	153
Figure A-3. SAXS intensities as a function of scattering vector for Sample 2 obtained by integrating over +/- 10 degree conical slices around $\phi = 180$ deg.	154
Figure A-4. Summary of mean and standard deviation of CNT diameters at varying distances above the substrate (<i>h</i>) as measured by SAXS and compared against TEM measurements.	155
Figure A-5. Hermans' orientation parameter (<i>f</i>) as a function of distance from substrate (<i>h</i>).	156
Figure A-6. Representative SEM micrographs of MWCNT films.	157
Figure B-1. TEM image of Au nanocluster arrays created from PS- <i>b</i> -PAA micellar thin film submerged in a 7 mM AuCl ₃ aqueous solution.	160
Figure B-2. SEM image of ZnO nanowires grown from PS- <i>b</i> -PAA templated Au nanoclusters on a Si substrate.	161
Figure B-3. SEM image of ZnO nanowires vertically grown from PS- <i>b</i> -PAA templated Au nanoclusters on a sapphire (110) substrate.	162
Figure C-1. Diagram illustrating the proposed utilization of the self assembly of PS- <i>b</i> -PMMA to pattern PS- <i>b</i> -PAA micelles on a nanometer length scale.	164
Figure C-2. AFM height image of a PS(170k)- <i>b</i> -PMMA(168k) thin film after spin casting onto a Si substrate.	164
Figure C-3. AFM height image of a PS(170k)- <i>b</i> -PMMA(168k) thin film after spin casting onto a Si substrate and annealing in toluene for: a) 3.5 hours, b) 19 hours.	165
Figure C-4. AFM height (a) and phase (b) images of a PS(170k)- <i>b</i> -PMMA(168k) thin film loaded with PS- <i>b</i> -PAA iron loaded micelles with a ratio of [PS- <i>b</i> -PMMA / PS- <i>b</i> -PAA] = 25 after spin casting onto a Si substrate.	167
Figure C-5. AFM height (a) and phase (b) images of a PS(170k)- <i>b</i> -PMMA(168k) thin film loaded with PS- <i>b</i> -PAA iron loaded micelles with a ratio of [PS- <i>b</i> -PMMA / PS- <i>b</i> -PAA] = 10 after spin casting onto a Si substrate.	168
Figure C-6. AFM height (a) and phase (b) images of a PS(170k)- <i>b</i> -PMMA(168k) thin film loaded with PS- <i>b</i> -PAA iron loaded micelles with a ratio of [PS- <i>b</i> -PMMA / PS- <i>b</i> -PAA] = 5 after spin casting onto a Si substrate.	170
Figure C-7. AFM phase image of a PS(170k)- <i>b</i> -PMMA(168k) thin film loaded with PS- <i>b</i> -PAA iron loaded micelles with a ratio of [PS- <i>b</i> -PMMA / PS- <i>b</i> -PAA] = 5 after spin casting onto a Si substrate and annealing in acetone for 3.5 hours.	171
Figure D-1. TEM image of iron oxide nanoclusters synthesized from a monolayer of PS- <i>b</i> -PAA with a FeCl ₃ loading ratio of 0.3.	173
Figure D-2. TEM image of iron oxide nanoclusters synthesized from a bilayer of PS- <i>b</i> -PAA with a FeCl ₃ loading ratio of 0.3.	173

Figure D-3. TEM image of iron oxide nanoclusters synthesized from a PS- <i>b</i> -PAA micellar thin film with a thickness of at least four monolayers and a FeCl ₃ loading ratio of 0.3.	174
Figure D-4. TEM image of gold nanoclusters synthesized from a PS- <i>b</i> -P2VP monolayer micellar thin film with a HAuCl ₄ loading ratio of 0.35.	175
Figure D-5. TEM image of gold nanoclusters synthesized from a PS- <i>b</i> -P2VP micellar thin film with a thickness greater than four monolayers and a HAuCl ₄ loading ratio of 0.35.	176
Figure E-1. TEM image of iron oxide nanocluster synthesized by submerging a PS- <i>b</i> -PAA micellar thin film into 0.5 mM FeCl ₃ for 60 min.	177
Figure E-2. TEM image of iron oxide nanocluster synthesized by submerging a PS- <i>b</i> -PAA micellar thin film into 5.0 mM FeCl ₃ for 19 hours.	178

List of Tables

Table 3-1. Effects of varying metal loading ratio on diameter, center-to-center spacing, and areal density of iron oxide nanocluster arrays.	58
Table 3-2. Effects of varying the molecular weight of PS- <i>b</i> -PAA on diameter, center-to-center spacing, and areal density of iron oxide nanocluster arrays.	62
Table 3-3. Effects of varying the ratio of PS homopolymer molecules per PS- <i>b</i> -PAA molecule on the areal density of iron oxide nanocluster arrays synthesized from micellar thin films using PS- <i>b</i> -PAA (16.4/4.5) with a FeCl ₃ loading ratio of 5.4.....	66
Table 5-1. Effects of varying the feature width and periodicity of the PDMS stamp on the width and periodicity of the resulting PS- <i>b</i> -PAA micellar thin film features.	111
Table 5-2. Effects of varying the diameter and periodicity of cylindrical posts on a PDMS stamp on the diameter and periodicity of the resulting patterned PS- <i>b</i> -PAA micellar thin film.....	117

Chapter 1 Introduction

1.1 Block Copolymers and Their Properties

Block copolymers are generally defined as macromolecules that contain two or more polymer chains that are bound together through covalent bonds. The simplest block copolymer is the diblock copolymer, which consists of two different polymer chains covalently attached at their ends. More complicated architectures include triblock copolymers and mixed arm block copolymers, where more than three polymer chains are covalently attached at a common branching point.

The block copolymer field originated with the discovery of termination-free anionic polymerizations, which allowed for the sequential addition of monomers to “living” polymer chains, thereby leading to block copolymers¹. Many different synthesis routes are now used to produce a wide variety of block copolymers². In the last decade the main advance in block copolymer synthesis has been the discovery of living radical polymerization techniques such as atom transfer radical polymerization³, which has allowed for the synthesis of many new block copolymer species.

Block copolymers have received significant attention over the last few decades because of their ability to self-assemble on the nanometer length scale⁴⁻⁶. This self-assembly is caused by both the incompatibility of the two polymer blocks and their covalent connectivity. The phase behavior of bulk block copolymer films has been extensively studied⁷⁻¹⁰, and the three primary morphologies of lamellae, hexagonally-

packed cylinders, and body-centered cubic spheres are now well established. The phase behavior of these systems can be controlled by varying: the overall degree of polymerization of the block copolymer, the fraction of each component within the block copolymer, and the segment-segment (Flory – Huggins) interaction parameter⁷, χ .

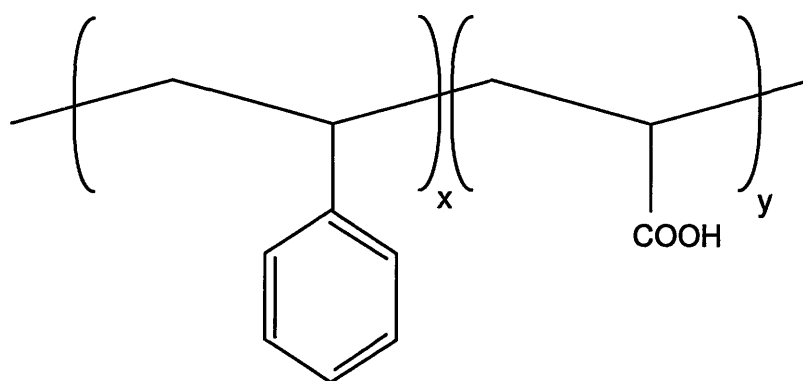
In order to take advantage of the self-assembly of block copolymers to create nanoscale structures, block copolymer thin films have often been used. In the seminal work by Park *et al.*¹¹, a self-assembled block copolymer thin film was utilized to create dense periodic arrays of holes and dots on a substrate on a nanometer length scale. Since then considerable research has been performed using block copolymer thin films as templates for the production of various nanoscale features including nanowires¹²⁻¹⁴, magnetic storage media¹⁵, nanopores¹⁶, and silicon capacitors¹⁷.

1.2 Micellar Behavior of Block Copolymers

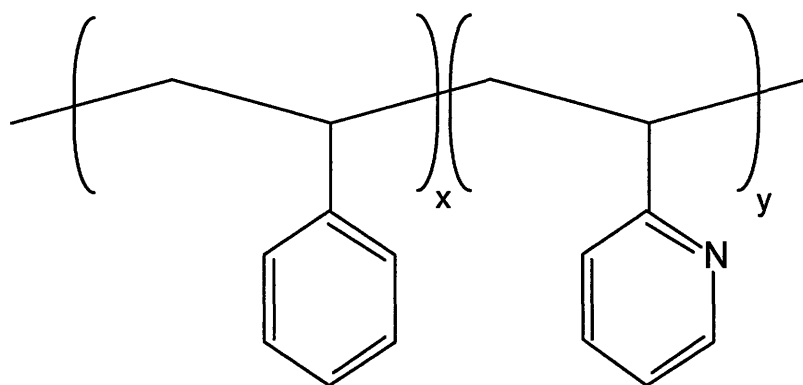
An interesting subclass of block copolymers are amphiphilic block copolymers, in which one of the polymer blocks is hydrophilic and the other polymer block is hydrophobic. When amphiphilic block copolymers are added to an organic solvent, the block copolymer forms micelles with hydrophilic cores and hydrophobic shells in a manner similar to low molecular weight surfactant molecules¹⁸. Research has shown that the micellization of these block copolymers in an organic medium is an enthalpically-driven process¹⁹. Although there is an unfavorable entropic contribution due to the micelle formation, this is outweighed by the favorable enthalpic contribution due to replacing hydrophilic polymer/solvent interactions with hydrophilic polymer/hydrophilic polymer and solvent/solvent interactions. While block copolymer micelles and small

molecule surfactant micelles both show narrow size distributions, block copolymer micelles have a significantly lower critical micelle concentration and have considerably slower exchange kinetics relative to small molecule surfactant micelles²⁰. On a reasonable time scale, the block copolymer micelles don't have a dynamic equilibrium with the single chains in solution and can be regarded as "frozen" structures. The slow exchange kinetics will prove to be crucial in utilizing block copolymer micelles to create thin films.

Another valuable feature of block copolymer micelles is the ability to systematically vary the size of the micellar core over a wide range. Experimental studies using small angle x-ray scattering (SAXS) have shown that the block copolymer micellar core scales as $N_{\text{core}}^{3/5}$ in organic media²⁰⁻²³, where N_{core} is the number of repeat units of the block copolymer segment that constitutes the core of the micelles. This scaling relationship has been corroborated by theoretical work on the size variation of block copolymer micelles²⁴⁻²⁵.



Poly(styrene-*block*-acrylic acid)



Poly(styrene-*block*-2-vinyl pyridine)

Figure 1-1. Structure of repeat units for poly(styrene-*block*-acrylic acid) (PS-*b*-PAA) and poly(styrene-*block*-2-vinyl pyridine) (PS-*b*-P2VP).

The unique properties of block copolymer micelles have led to a wide range of possible applications for these systems. There has been strong interest in using block copolymer micelles as controlled drug delivery systems for diagnostic agents and in gene therapy²⁶⁻³⁴. Considerable research has also focused on using block copolymer micelles for surface modification^{4,35-42} and for the synthesis of inorganic nanoclusters⁴³⁻⁶⁰. This thesis will focus on utilizing the unique capabilities of block copolymer micelles to create tunable inorganic nanocluster arrays using the amphiphilic block copolymers poly(styrene-*block*-acrylic acid) (PS-*b*-PAA) and poly(styrene-*block*-2-vinylpyridine) (PS-*b*-P2VP). The repeat units for these block copolymers are shown in Figure 1-1.

1.3 Patterning of Inorganic Nanoclusters via Block Copolymers

Inorganic nanoclusters are simply small aggregates of inorganic atoms or molecules with diameters less than 100 nm. These inorganic nanoclusters have a very

large surface area to volume ratio, and they have been shown to exhibit properties that are characteristic of neither atoms nor bulk material⁶¹. These nanoclusters have been shown to exhibit interesting catalytic, non-linear optic, magnetic, and semiconductor properties⁶².

Block copolymers are ideal templates for the production of inorganic nanocluster arrays⁴³⁻⁵³. The approaches used to synthesis the inorganic nanoclusters can be separated into two basic routes. The first involves binding inorganic species to a monomer prior to polymerization or micellization⁴³, while the second involves binding the inorganic species into pre-formed block copolymer domains⁴⁴⁻⁵³. The disadvantages for the former route include the lack of monomers containing inorganic species and the difficulties in polymerizing these monomers using a living polymerization method. Because of these disadvantages, this thesis will focus primarily on loading the inorganic species into pre-formed block copolymer domains.

The initial demonstration of the loading of inorganic species into pre-formed block copolymer domains was used to create silver⁴⁴⁻⁴⁶, gold⁴⁴, and zinc⁴⁷ nanoclusters within a bulk block copolymer substrate. This procedure for producing inorganic nanoclusters relied on free carboxylate groups within one domain of the block copolymer to sequester inorganic ions from an aqueous inorganic salt solution⁴⁸⁻⁴⁹. Further work demonstrated the generality of the approach by synthesizing other inorganic nanoclusters, including palladium, platinum, copper, and lead⁴⁹. More recently other chemical functional groups, such as pyridine, have been used to sequester inorganic species to create gold⁵⁰⁻⁵², cobalt⁵³, rhodium⁵⁰, and platinum⁵⁰ nanoclusters.

Although the above routes demonstrated a route for synthesizing patterned inorganic nanoclusters, the uses of the resulting nanoclusters are limited because of their sequestration within a three-dimensional matrix of block copolymer. Recently the procedures developed for inorganic nanocluster synthesis have been combined with amphiphilic block copolymer micelles to create two-dimensional patterned arrays of inorganic nanoclusters on a substrate⁵⁴⁻⁵⁸. Two main routes have been developed: nanocluster formation within the block copolymer micelles in solution⁵⁴⁻⁵⁷, and the selective loading of inorganic ions into specific domains within a pre-formed block copolymer micellar thin film⁵⁸. These routes have led to the synthesis of “quasi”-hexagonal arrays of silver⁵⁸, lead⁵⁸, gold⁵⁵⁻⁵⁷, and titanium oxide⁵⁴ nanoclusters on a substrate surface. The applications for these block copolymer micellar-based nanocluster arrays have included ZnO nanowire synthesis⁵⁹, protein binding⁶⁰, and nanolithography⁵⁶.

1.4 Applications for Inorganic Nanocluster Arrays

1.4.1 Catalysts for Carbon Nanotube Synthesis

Carbon nanotubes (CNTs) have received considerable attention since their discovery in 1991⁶³, and their unusual set of mechanical, electrical, and thermal properties have led to possible opportunities in a wide range of applications including nanoelectronics⁶⁴, field emission⁶⁵, and hydrogen storage⁶⁶. While there are several different routes to synthesize CNTs, this review will focus on synthesis via chemical vapor deposition (CVD) because of its flexibility and its suitability for a wide range of applications⁶⁷. In general, the CVD synthesis technique requires: a carbon feedstock, catalytic nanoclusters, and heat⁶⁷. Although the mechanism for growth is still unclear, it

is believed that the general mechanism involves the carbon feedstock decomposing and dissolving into the metal nanoclusters at high temperature, followed by the precipitation of the carbon from the nanocluster to form the CNT⁶⁸. Because each nanoparticle catalyzes one CNT, the ability to control the size and patterning of surface-bound inorganic nanoclusters is an essential task.

The most common route for synthesizing metal nanocluster arrays for CNT growth involves sputtering or evaporating a thin metal film onto a substrate^{69,70}, which subsequently dewets to form nanoclusters at an elevated growth temperature prior to growth⁷¹⁻⁷³. While these catalysts are easily prepared, these approaches are not easily able to create nanoclusters with monodisperse diameters and quantifiable areal densities. Many approaches have been utilized in order to synthesize nanoclusters with monodisperse diameters or controllable areal densities⁷⁴⁻⁸⁰, but none of the approaches offer the ability to create monodisperse diameter nanoclusters with independently tunable diameters and areal densities.

1.4.2 *Templates for Synthesizing DNA Nanoarrays*

DNA microarrays are an increasingly important biological tool that have been used for a host of applications including examining gene expression⁸¹, fundamentally studying cancer and genetic diseases^{82,83}, and for the screening of drugs based on their interactions with DNA⁸⁴. The two commercial routes for creating DNA microarrays involve either *in situ* synthesis or *ex situ* spotting^{85,86}. *In situ* synthesis involves the addition of a nucleotide to a growing oligonucleotide that has been spatially arranged on a substrate via a photolithographic mask⁸⁵. This process has the advantage of design flexibility, but the synthesis cycle consists of multiple steps and the length of the

oligonucleotide is limited to approximately 60 basepairs^{86,87}. The other alternative is to spot pre-synthesized oligonucleotides to a substrate using either contact printing or by projection via nozzles⁸⁸. The *ex situ* method doesn't limit the size of the oligonucleotides, but the cost of creating the DNA microarrays scales with the size of the substrate. Both of these routes are subject to an accumulation of errors due to their sequential processing and are not suited for creating more complex microarrays⁸⁶.

Recently Stellacci and coworkers^{89,90} presented a novel printing technique, known as Supramolecular Nano-Stamping (SuNS), that replicated single-stranded DNA (ssDNA) arrays through a hybridization – contact – dehybridization cycle. The SuNS method generally relies on modified DNA to form bonds with the target substrate. To illustrate the technique, a lithographically-patterned gold substrate was used to bind hexylthiol-modified DNA before printing onto a gold substrate⁸⁹. By combining the tunable gold nanocluster arrays synthesized from block copolymer micellar thin films with the SuNS technique, significant advances in DNA array synthesis may be achievable.

1.5 Thesis Outline

Based on the discussions outlined in this chapter, the goal of this research is to demonstrate that block copolymer micellar thin films can usefully facilitate the synthesis of tunable inorganic nanocluster arrays for a variety of possible applications. Chapter 2 first demonstrates the capability of creating iron oxide nanocluster arrays using block copolymer micellar thin films. These iron oxide nanocluster arrays are then used as catalysts for the growth of CNTs in a CVD reaction. Chapter 3 focuses on demonstrating

the tunability of arrays synthesized via block copolymer micellar thin films. A variety of routes are used to tune the size and spacing of the inorganic nanoclusters, including the variation of the block copolymer molecular weight, the variation of the metal salt added to solution, the addition of PS homopolymer, and the mixing of different micellar solutions. Chapter 4 combines the progress from Chapters 2 and 3 to demonstrate that the morphology of CNT thin films can be controlled by varying the properties of the inorganic nanocluster arrays synthesized via block copolymer micellar thin films. Chapter 5 demonstrates a route for patterning block copolymer micellar thin films on a micron-length scale via a micro-contact printing procedure. The patterned inorganic nanocluster arrays are then shown to be effective catalysts for producing patterned CNT structures. To demonstrate the generality of the block copolymer micellar approach, Chapter 6 shows that tunable gold nanocluster arrays synthesized using this approach can be used to create DNA nanoarrays. Finally, this thesis closes with conclusions and recommendations for future work in Chapter 7.

1.6 References

1. M. Szwarc, *Nature* **1956**, 178, 1168.
2. Hillmyer, M. *Current Opinions in Solid State & Matter Science* **1999**, 4, 559.
3. Davis, K. A.; Matyjaszewski, K. *Macromolecules* **2001**, 34, 2101.
4. Hamley, I. W. *The Physics of Block Copolymers*; Oxford University Press: New York, New York, 1998.
5. Riess, G. *Progress in Polymer Science*, **2003**, 28, 1107 – 1170.
6. Hamley, I. W. *Nanotechnology*, **2003**, 14, R39 – R54.
7. Bates, F. S.; Fredrickson, G. H. *Annual Review of Physical Chemistry* **1990**, 41, 525.

8. Fredrickson, G. H.; Bates, F. S. *Annual Review of Material Science* **1996**, 26, 501.
9. Hashimoto, T.; Sakamoto, N.; Koga, T. *Physical Review E*, **1996**, 54, 5832.
10. Khandpur, A. K.; Foerster, S.; Bates, F. S.; Hamley, I. W.; Ryan, A. J.; Bras, W.; Almdal, K.; Mortensen, K. *Macromolecules* **1995**, 28, 8796 – 8806.
11. Park, M.; Harrison, C.; Chaikin, P.; Register, R. A.; Adamson, D. H. *Science* **1997**, 276, 1401.
12. Thurn-Albrecht, T.; Schotter, J.; Kastle, G. A.; Emley, N.; Shibauchi, T.; Krusin-Elbaum, L.; Guarini, K.; Black, C. T.; Tuominen, M. T.; Russell, T. P. *Science* **2000**, 290, 2126 – 2129.
13. Kim, H.-C.; Jia, X.; Stafford, C. M.; Kim, D. H.; McCarthy, T. J.; Tuominen, M.; Hawker, C. J.; Russell, T. P. *Advanced Materials* **2001**, 13, 795 – 797.
14. Lopes, W. A.; Jaeger, H. M. *Nature* **2001**, 414, 735 – 738.
15. Cheng, J. Y.; Ross, C. A.; Chan, V. Z.-H.; Thomas, E. L.; Lammertink, R. G. H.; Vancso, G. J. *Advanced Materials* **2001**, 13, 1174 – 1178.
16. Chan, V. Z.-H.; Hoffman, J.; Lee, V. Y.; Iatrou, H.; Avgeropoulos, A.; Hadjichristidis, N.; Miller, R. D.; Thomas, E. L. *Science* **1999**, 286, 1716 – 1719.
17. Black, C. T.; Guarini, K. W.; Milkove, K. R.; Baker, S. M.; Russell, T. P.; Tuominen, M. T. *Applied Physics Letters* **2001**, 79, 409 – 411.
18. Alexandridis, P.; Lindman, B. *Amphiphilic Block Copolymers: Self-Assembly and Applications*; Elsevier Science B. V.: Amsterdam, The Netherlands, 2000.
19. Price, C. In *Developments in Block Copolymers*; Goodman, I., Ed.; Applied Science Publishers: London, 1982: Volume 1, 39 – 79.
20. Moffitt, M.; Khougaz, K.; Eisenberg, A. *Accounts of Chemical Research* **1996**, 29, 95 – 102.
21. Nguyen, D.; Williams, C. E.; Eisenberg, A. *Macromolecules*, **1994**, 27, 5090.
22. Nguyen, D.; Varshney, S. K.; Williams, C. E.; Eisenberg, A. *Macromolecules*, **1994**, 27, 5086.
23. Khougaz, K.; Nguyen, D.; Williams, C. E.; Eisenberg, A. *Canadian Journal of Chemistry*, **1995**, 73, 2086 – 2093.
24. Zhulina, E. B.; Birshstein, T. M. *Vysokomolekulyarnye Soedineniya Seriya A*, **1985**, 27, 511.

25. Halperin, A. *Macromolecules*, **1989**, 22, 3806.
26. Kabanov, A. V.; Alakhov, V. Y. In *Amphiphilic Block Copolymers: Self-Assembly and Applications*; Elsevier Science B. V.: Amsterdam, The Netherlands, 2000. 347 – 376.
27. Kabanov, A. V.; Batrakova, E. V.; Alakhov, V. Y. *Journal of Controlled Release* **2002**, 82, 189 – 212.
28. Kakizawa, Y.; Kataoka, K. *Advanced Drug Delivery Reviews* **2002**, 54, 203 – 222.
29. Malmsten, M. In *Amphiphilic Block Copolymers: Self-Assembly and Applications*; Elsevier Science B. V.: Amsterdam, The Netherlands, 2000. 319 – 346.
30. Arshady, R., editor. *Polymers in Medicine and Biotechnology*; Citus Books, London, 2002.
31. Torchilin, V. P. *Journal of Controlled Release* **2001**, 73, 137 – 172.
32. Kwon, G. S.; Okano, T. *Advanced Drug Delivery Reviews* **1996**, 21, 107 – 116.
33. Trubetskoy, V. S. *Advanced Drug Delivery Reviews* **1999**, 37, 81 – 88.
34. Liu, M.; Kono, K.; Frechet, J. M. J. *Journal of Controlled Release* **2000**, 65, 121 – 131.
35. Tirrell, M. In *Solvents and Self-Organization of Polymer*; Dordrecht: Kluwer Academic Publisher: 1996. 281 – 308.
36. Munch, M. R.; Gast, A. P. *Macromolecules* **1990**, 23, 2313 – 2320.
37. Xu, R.; d'Oliveira, J. M. R.; Winnik, M. A. Riess, G.; Croucher, M. D. *Journal of Applied Polymer Science: Applied Polymer Symposium* **1992**, 51, 135 – 149.
38. Breulman, M.; Forster, S.; Antonietti, M. *Macromolecular Chemistry and Physics* **2000**, 201, 204 – 211.
39. Thyebault, H.; Riess, G. *Agglomeration Process of Latex, Application of the Agglomerated Latex for the Modification of Thermoplastic Matrices in Order to Increase Their Impact Resistance*. European Patent 0,249,554.
40. Cabane, B.; Dupliessix, R. *Colloids and Surfaces* **1985**, 13, 19 – 33.
41. Clarke, C. J.; Lennox, R. B.; Eisenberg, A.; Rafailovich, M. H.; Sokolov, J. In *Solvents and Self-Organization of Polymer*; Dordrecht: Kluwer Academic Publisher: 1996. 73 – 81.

42. Huang, W.; Baker, G. L.; Bruening, M. L. *American Chemical Society Preprints (Division of Polymer Chemistry)* **2002**, *43*, 638 – 639.
43. Chan, Y. N. C.; Craig, G. S. W.; Schrock, R. R.; Cohen, R. E. *Chemistry of Materials*, **1992**, *4*, 885.
44. Chan, Y. N. C.; Schrock, R. R.; Cohen, R. E. *Chemistry of Materials* **1992**, *4*, 24.
45. Chan, Y. N. C.; Schrock, R. R.; Cohen, R. E. *Journal of the American Chemical Society* **1992**, *114*, 7295.
46. Sohn, B. H.; Cohen, R. E. *Acta Polymerica* **1996**, *47*, 340.
47. Yue, J.; Sankaran, V.; Cohen, R. E.; Schrock, R. R. *Journal of the American Chemical Society* **1993**, *115*, 4409.
48. Yue, J.; Cohen, R. E. *Supramolecular Science* **1995**, *1*, 117.
49. Clay, R. T.; Cohen, R. E. *Supramolecular Science* **1995**, *2*, 183.
50. Seregina, M. V.; Bronstein, L. M.; Platonova, O. A.; Chernyshov, D. M.; Valetsky, P. M.; Hartmann, J.; Wenz, E.; Antonietti, M. *Chemistry of Materials* **1997**, *9*, 923.
51. Bronstein, L. M.; Sidorov, S. N.; Valetsky, P. M.; Hartmann, J.; Colfen, H.; Antonietti, M. *Langmuir* **1999**, *15*, 6256.
52. Antonietti, M.; Wenz, E.; Bronstein, L.; Seregina, M. *Advanced Materials* **1995**, *7*, 1000.
53. Platanova, O. A.; Bronstein, L. M.; Solodovnikov, S. P.; Yanovskaya, I. M.; Obolonkova, E. S.; Valetsky, P. M.; Wenz, E.; Antonietti, M. *Colloid and Polymer Science* **1997**, *275*, 426.
54. Spatz, J.; Mossmer, S.; Moller, M.; Kocher, M.; Neher, D.; Wegner, G. *Advanced Materials* **1998**, *10*, 473.
55. Spatz, J. P.; Roescher, A.; Moller, M. *Advanced Materials* **1996**, *8*, 337.
56. Spatz, J. P.; Herzog, T.; Mossmer, S.; Ziemann, P.; Moller, M. *Advanced Materials* **1999**, *11*, 149.
57. Koslowski, B.; Strobel, S.; Herzog, T.; Heniz, B.; Boyen, H. G.; Notz, R.; Ziemann, P.; Spatz, J. P. *Journal of Applied Physics* **2000**, *87*, 7533.
58. Boontongkong, Y.; Cohen, R. E. *Macromolecules* **2002**, *35*, 3647 – 3652.

59. Haupt, M.; Ladenburger, A.; Sauer, R.; Thonke, K.; Glass, R.; Roos, W.; Spatz, J. P.; Rauscher, H.; Riethmuller, S.; Moller, M. *Journal of Applied Physics* **2003**, *93*, 6252 – 6257.
60. Spatz, J. P.; Mossmer, S.; Hartmann, C.; Moller, M.; Herzog, T.; Krieger, M.; Boyen, H. G.; Ziemann, P.; Kabius, B. *Langmuir* **2000**, *16*, 407 – 415.
61. Henglein, A. *Chemical Reviews* **1989**, *89*, 1861 – 1873.
62. Bradley, J. S. In *Cluster and Colloids: From Theory to Application*; Weinheim: Wiley / VCH: 1994.
63. Iijima, S. *Nature* **1991**, *354*, 56 – 58.
64. Tans, S. J.; Verschueren, A. R. M.; Dekker, C. *Nature* **1998**, *393*, 49 – 52.
65. DeHeer, W. A.; Chatelain, A.; Ugarte, D. *Science* **1995**, *270*, 1179 – 1180.
66. Dillon, A. C.; Jones, K. M.; Bekkedahl, T. A.; Kiang, C. H.; Bethune, D. S.; Heben, M. J. *Nature*, **1997**, *386*, 377 – 379.
67. Teo, K. B. K.; Singh, C.; Chhowalla, M.; Milne, W. I. In *Encyclopedia of Nanoscience and Nanotechnology*; American Scientific Publishers: Stevenson Ranch, California: 2003.
68. Baker, R. T. K.; Barber, M. A.; Harris, P. S.; Feates, F. S.; Waite, R. J. *Journal of Catalysis* **1972**, *26*, 51.
69. Delzeit, L.; Nguyen, C. V.; Chen, B.; Stevens, R.; Cassell, A.; Han, J.; Meyyappan, M. *Journal of Physical Chemistry B* **2002**, *106*, 5629-5635.
70. Hart, A. J.; Slocum, A. H.; Royer, L. *Carbon* **2006**, *44*, 348-359.
71. Lacerda, R. G.; Teo, K. B. K.; Teh, A. S.; Yang, M. H.; Dalal, S. H.; Jefferson, D. A.; Durrell, J. H.; Rupesinghe, N. L.; Roy, D.; Amaratunga, G. A. J.; Milne, W. I.; Wyczisk, F.; Legagneux, P.; Chhowalla, M. *Journal of Applied Physics* **2004**, *96*, 4456-4462.
72. Hofmann, S.; Cantoro, M.; Kleinsorge, B.; Casiraghi, C.; Parvez, A.; Robertson, J.; Ducati, C. *Journal of Applied Physics* **2005**, *98*, 34308-34301.
73. Futaba, D.; Hata, K.; Namai, T.; Yamada, T.; Mizuno, K.; Hayamizu, Y.; Yumura, M.; Iijima, S. *Journal of Physical Chemistry B* **2006**, *110*, 8035.
74. Tu, Y.; Huang, Z. P.; Wang, D. Z.; Wen, J. G.; Ren, Z. F. *Appl. Phys. Lett.* **2002**, *80*, 4018-4020.

75. Cheung, C. L.; Kurtz, A.; Park, H.; Lieber, C. M. *J. Phys. Chem. B*, **2002**, *106*, 2429-2433.
76. Choi, H. C.; Kundaria, S.; Wang, D. W.; Javey, A.; Wang, Q.; Rolandi, M.; Dai, H. J. *Nano Lett.* **2003**, *3*, 157-161.
77. Li, Y. M.; Kim, W.; Zhang, Y. G.; Rolandi, M.; Wang, D. W.; Dai, H. J. *J. Phys. Chem. B* **2001**, *105*, 11424-11431.
78. Hinderling, C.; Keles, Y.; Stockli, T.; Knapp, H. F.; de los Arcos, T.; Oelhafen, P.; Korczagin, I.; Hempenius, M. A.; Vancso, G. J.; Pugin, R.; Heinzelmann, H. *Adv. Mater.* **2004**, *16*, 876-879.
79. Huh, Y.; Green, M. L. H.; Kim, Y. H.; Lee, J. Y.; Lee, C. J. *Applied Surface Science* **2005**, *249*, 145-150.
80. Zhang, L.; Tan, Y.; Resasco, D. *Chemical Physics Letters* **2006**, *422*, 198-203.
81. Lockhart, D. J.; Dong, H.; Byrne, M. C.; Follettie, M. T.; Gallo, M. V.; Chee, M. S.; Mittmann, M.; Wang, C.; Kobayashi, M.; Horton, H.; Brown, E. L. *Nature Biotechnology* **1996**, *14*, 1675 – 1680.
82. Hacia, J. G.; Brody, L. C.; Chee, M. S.; Fodor, S. P.; Collins, F. S. *Nature Genetics* **1996**, *14*, 441 – 447.
83. Golub, T. R.; Slonim, D. K.; Tamayo, P.; Huard, C.; Gaasenbeek, M.; Mesirov, J. P.; Coller, H.; Loh, M. L.; Downing, J. R.; Caligiuri, M. A.; Bloomfield, C. D.; Lander, E. S. *Science* **1999**, *286*, 531 – 537.
84. Stegmaier, K.; Ross, K. N.; Colavito, S. A.; O'Malley, S.; Stockwell, B. R.; Golub, T. R. *Nature Genetics* **2004**, *36*, 257 – 263.
85. Pirrung, M. C. *Chemical Review* **1997**, *97*, 473 – 488.
86. Pirrung, M. C. *Angewandte Chemie, International Edition* **2002**, *41*, 1276 – 1289.
87. Lombardi, S. *PharmaGenomics* **2004**, *4*, S25
88. Okamoto, T.; Suzuki, T.; Yamamoto, N. *Nature Biotechnology* **2000**, *18*, 438 – 441.
89. Yu, A. A.; Savas, T. A.; Taylor, G. S.; Guiseppe-Elie, A.; Smith, H. I.; Stellacci, F. *Nano Letters* **2005**, *5*, 1061 – 1064.
90. Yu, A. A.; Savas, T. A.; Cabrini, S.; diFabrizio, E.; Smith, H. I.; Stellacci, F. *Journal of the American Chemical Society* **2005**, *127*, 16774 – 16775.

Chapter 2 Using Block Copolymer Micellar Thin Films as Templates for the Production of Catalysts for Carbon Nanotube Growth*

2.1 Introduction

Carbon nanotubes (CNTs) have been the focus of intense research since their discovery in 1991¹, and many potential applications, such as field emission², hydrogen storage³, and microelectronics⁴, seek to exploit the unusual set of mechanical, structural, and electronic properties that CNTs possess. Although there are multiple methods for synthesizing CNTs, chemical vapor deposition (CVD) is the most widely used because of its ease of operation and its scale-up capability. In CVD, metal nanoparticles (namely iron, cobalt, and nickel) are required to catalyze the growth of CNTs, so the ability to control the size and patterning of surface-bound metal nanoparticles is an essential task.

One of the most common routes for creating the surface arrays of metal nanoparticles involves, as a first step, depositing a thin layer of metal on a surface using magnetron sputtering or evaporation⁵⁻⁷. Upon heating, the metal thin film forms metal nanoparticles, which are then capable of catalyzing the growth of CNTs. Although this method is straight forward, it offers little control over the size or spacing of the metal nanoparticles, and patterned nanoparticle arrays are not achievable.

Alternative procedures for creating metal nanoparticles have been developed recently in an attempt to gain better control over the size and spacing of the metal

* Portions of this chapter have been previously published in Bennett, R.D., Xiong, G.Y., Ren, Z.F., Cohen, R.E. *Chemistry of Materials* 2004, 16, 5589 – 5595.

nanoparticles. Ren and co-workers⁸ have used polystyrene nanosphere masks to deposit large periodic arrays of nickel nanoparticles with diameters between 50 – 100 nm. Ren and co-workers⁹ have also used electrochemical deposition to create Ni nanoparticles with controlled site density between about $10^6 - 10^8$ nanoparticles per cm^2 , although the nanoparticles are randomly located and have diameters ranging from less than 50 nm to greater than 200 nm. Lieber and co-workers¹⁰ created nearly monodisperse diameter iron nanoclusters with diameters between 3 – 13 nm in organic solvents by thermal decomposition of iron pentacarbonyl, and then deposited the nanoparticles onto a silicon substrate. In another approach, Dai and co-workers¹¹ created iron oxide nanoparticles with diameters of 1 – 2 nm by soaking silicon oxide substrates in a solution of hydroxylamine and FeCl_3 . Dai and co-workers¹² have also used the iron-storage protein, ferritin, to create discrete iron oxide nanoparticles which are catalytically active towards single wall CNT growth. Hinderling *et al*¹³ used a specially synthesized polystyrene-*block*-polyferrocenyldimethylesilane diblock copolymer to produce 30 nm iron oxide nanoparticles on silicon substrates that could be subsequently used to catalyze carbon nanotube growth.

In this chapter we demonstrate a simple approach that uses block copolymer micelles as a template to create large area arrays of metal nanoclusters capable of catalyzing the growth of multi-wall CNTs. Our route for producing metal nanocluster arrays relies on the ability of amphiphilic block copolymers, such as poly(styrene-*block*-acrylic acid) (PS-*b*-PAA), to form micelles in solution which are capable of self-organizing into partially ordered structures on surfaces¹⁴. Owing to the slow exchange kinetics in block copolymer micelles, we are able to transfer the micelles from colloidal

solution onto a substrate using a spin-casting process. This allows for the creation of quasi-hexagonal arrays of PAA spheres within a PS matrix. As shown previously^{14, 15}, by submerging the polymer thin films in an aqueous metal salt solution, the carboxylic acid groups in the PAA domains can be utilized in an ion-exchange protocol to selectively sequester a variety of metal cations. The polymer can then be removed using thermal degradation or oxygen plasma etching, resulting in arrays of metal-containing nanoclusters that are nearly monodisperse in size and patterned at a density of approximately 10^{11} particles per cm^2 . In principle, this route for synthesizing metal nanoclusters offers the capability of tuning the size and spacing between the metal nanoclusters by altering the molecular weight of the block copolymer¹⁶, which would lead to control over the size and spacing of the CNTs formed. Appropriate masking or stamping transfer techniques allow for the straightforward production of patterned arrays of the micellar block copolymer templates and, therefore, of the CNTs produced subsequently.

In this chapter we examine the effectiveness of block-copolymer-templated metal nanocluster arrays in catalyzing the growth of multi-wall CNTs in a thermal CVD process. We present scanning electron microscope (SEM) and transmission electron microscope (TEM) images of the as-grown CNTs still attached to their growth substrate, as well as high resolution TEM images of the multi-wall CNTs.

2.2 Experimental Section

2.2.1 Materials

Poly(styrene-*block*-acrylic acid) (PS-*b*-PAA) ($M_n(\text{PS}) = 16,400$ g/mol, $M_n(\text{PAA}) = 4,500$ g/mol, PDI = 1.05) was used as received from Polymer Source, Inc. The following chemicals were also used as received: anhydrous iron(III) chloride (FeCl_3) obtained from Sigma-Aldrich Co., lead(II) acetate trihydrate (PbAc_2) obtained from Sigma-Aldrich Co., sodium hydroxide (98.9%) (NaOH) obtained from Mallinckrodt, toluene (HPLC grade, 99.8%) obtained from Sigma-Aldrich Co. The silicon nitride membrane window substrates were purchased from Structure Probe, Inc. Each substrate (surface area ~ 4.5 mm²) consists of a 100 nm thick amorphous, low-stress Si_3N_4 membrane supported on a 0.2 mm thick silicon wafer that has been back-etched in the center to create the electron transparent Si_3N_4 window (surface area $\sim .2$ mm²). The use of the electron-transparent silicon nitride substrates allows for direct TEM characterization without disturbing the spin-cast films. Polished silicon wafers of $\langle 100 \rangle$ orientation from Nestec, Inc. were also used as received. Each substrate was rinsed with toluene prior to film casting. All aqueous solutions were made using deionized water (>18 M Ω cm, Millipore Milli-Q). Lacey carbon films were used as received from Electron Microscopy Sciences.

2.2.2 Sample Preparation

The sample preparation follows a procedure developed previously¹⁴, with adjustments (discussed below) to improve substrate wetting and consequently, the surface coverage of the metal nanoclusters. The block copolymer was mixed with toluene at a concentration of 12.5 – 15 mg/mL, resulting in a slightly cloudy solution. By heating the solution to $\sim 145^\circ\text{C}$ for 20 min, the solution became clear, and remained clear after cooling to room temperature. Previous work¹⁴ demonstrated that this transition in solution

optical properties corresponds to a change from cylindrical to spherical block copolymer micelles. Thin films were then created by spin-casting the micellar solution onto the substrates. The resulting morphology can be seen in Figure 2-1. The film thicknesses were approximately 20 nm, as determined by atomic force microscope (AFM). Residual toluene was then removed under vacuum.

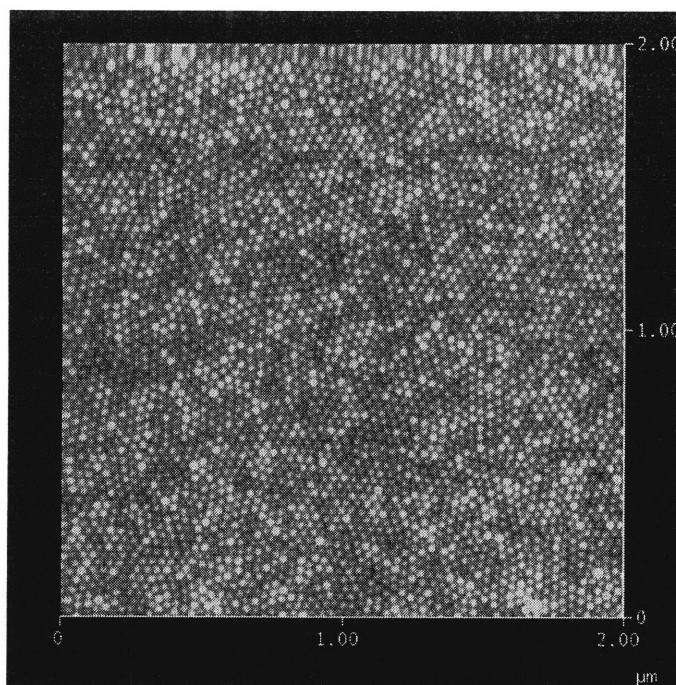


Figure 2-1. AFM height image of non-cavitated PS-*b*-PAA thin film on a silicon nitride substrate.

Two different methods were used to load the metal species into the polymer thin films. In the first, the polymer thin films were submerged in a 0.007 M $\text{NaOH}_{(\text{aq})}$ solution for 16 hr (subsequently referred to as a “cavitated” template). When the thin film is exposed to the $\text{NaOH}_{(\text{aq})}$ solution, the PAA domains swell¹⁷, and because this can not be accommodated by the glassy PS matrix, the swelling leads to the rupture of the PAA domains to the surface. This cavitation step is illustrated in Figure 2-2, and was discussed

in detail previously by Boontongkong *et al*¹⁴. These cavitated polymer thin films were then rinsed in deionized water for 1 min, submerged in a 0.5 mM FeCl₃ solution for 5 min, and then rinsed in deionized water for 2 min. The second route bypassed the cavitation step; the spin-coated films (subsequently referred to as a “non-cavitated” template) were submerged directly into 0.5 mM FeCl₃ for 60 min, and then rinsed for 2 min in deionized water. For the cavitated thin films, the Fe³⁺ ions in solution exchange directly with the Na⁺ ions of the carboxylic acid groups, while in the non-cavitated thin films the Fe³⁺ ions diffuse through a thin PS layer before exchanging with the H⁺ ions from the carboxylic acid groups. After the metal loading steps, the substrates were heated in air at 550°C for 20 min to degrade the polymer and to convert the iron ions into iron oxide nanoclusters. The resulting nanocluster arrays were then characterized using TEM and AFM. A control substrate was also created by following the sample preparation steps listed above while omitting the iron ion loading step.

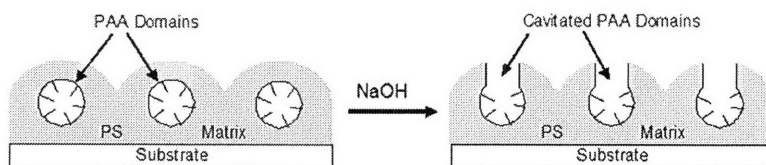


Figure 2-2. Diagram illustrating the cavitation step caused by submerging the PS-*b*-PAA thin films in NaOH_(aq) solution.

The nanocluster arrays were then used as catalytic substrates for the synthesis of CNTs using thermal CVD in a quartz-tube reactor. The chamber was pumped down to 0.1 Torr before raising the temperature to 750°C. Once the reactor reached 750°C, NH₃ gas was delivered to the reactor at 80 sccm for 10 min, and then C₂H₂ (feed gas) was

added at 20 sccm for the duration of the growth. Growth times of 10, 30, and 60 min were used. After the growth, the samples were allowed to cool to 250°C under vacuum, and then removed from the reactor. Specimens for high resolution TEM were prepared by sonicating the substrates containing CNTs in isopropanol for 20 minutes, and then solvent casting the CNTs onto lacey carbon films.

2.2.3 Microscopy

TEM was performed on a JEOL 200CX operating at 200 kV, a JEOL 2000FX operating at 200 kV, and a JEOL 2010 operating at 200 kV. SEM was performed on a JEOL 6320 FEG-SEM operating at 5 kV. AFM was performed on a Digital Instruments Dimension 3000 Nanoscope IIIA scanning probe microscope operating in Tapping mode using a silicon cantilever (nominal tip radius of 5 – 10 nm).

2.3 Results

2.3.1 Catalytic Substrates

The AFM image of Figure 2-1 shows the nanoscale surface topology that results when the PS-*b*-PAA solution is spin-coated onto a silicon nitride substrate. This image shows the presence of spherical objects with an average diameter of 18 nm. As illustrated in Figure 2-2, the PAA domains are expected¹⁴ to have a somewhat smaller diameter than the AFM image suggests. This was confirmed by staining the PAA domains using a PbAc₂ solution, as shown in the TEM image in Figure 2-3. The stained PAA domains have diameters of approximately 12 – 14 nm. Figure 2-3 also demonstrates the quasi-

hexagonal array of the PAA domains within the PS matrix. This spatial arrangement is maintained over >95% of the substrate surface.

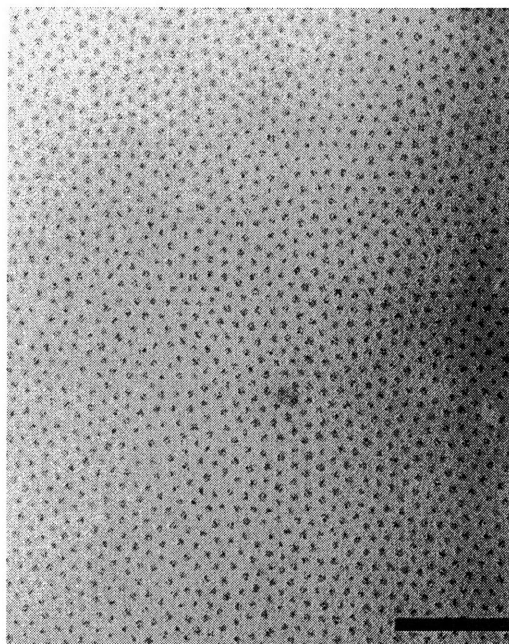


Figure 2-3. TEM image of Pb nanocluster array created from a non-cavitated thin film, Scale bar = 200 nm. Lead was used in place of iron because it offers enhanced contrast in the TEM. In addition, it demonstrates the general receptivity of the PS-*b*-PAA block copolymer to a variety of metal cations^{14,15}.

In this work, nanocluster arrays for CNT growth were produced using both cavitated and non-cavitated thin films as templates. In both of these synthesis routes, similar iron oxide nanocluster arrays were produced. Figure 2-4a shows a TEM image of an iron-containing nanocluster array produced by loading a cavitated thin film with iron and then thermally degrading the polymer in air at 550°C for 20 min. The heating step removes the polymer and leaves behind iron-containing nanoclusters with diameters of 7.5 ± 0.8 nm and center-to-center spacings of 30 – 35 nm. The areal density is

approximately 10^{11} nanoclusters per cm^2 and the nanocluster patterning is retained over nearly the entire substrate during the heating step. For the iron oxide nanocluster arrays synthesized from non-cavitated arrays, it should be noted that approximately 75 – 80 % of the substrate surface shows nanoclusters arranged in the quasi-hexagonal array similar to Figure 2-4a, while 20 – 25 % of the substrate has nanoclusters which are completely disordered, as shown in Figure 2-4b. For reasons not yet understood, this loss of ordering on the substrate surface is seen only in the nanocluster arrays produced using the 550°C heat treatment on non-cavitated thin films, and not in the nanocluster arrays created using cavitated thin films.

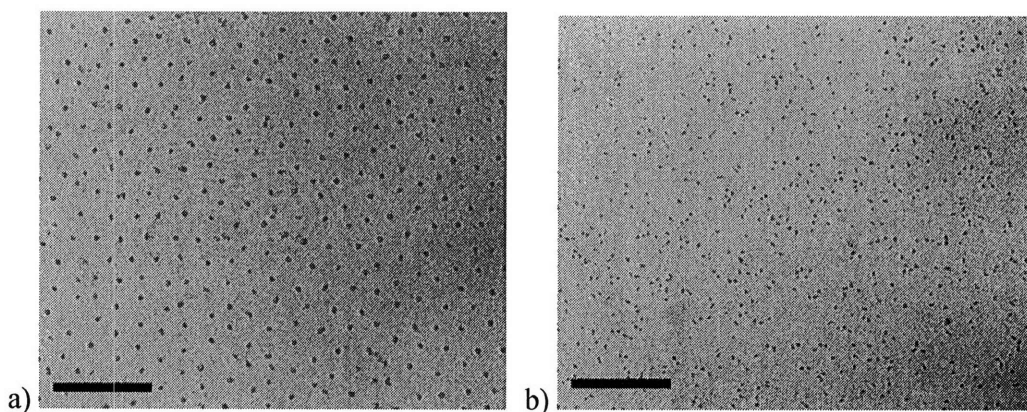


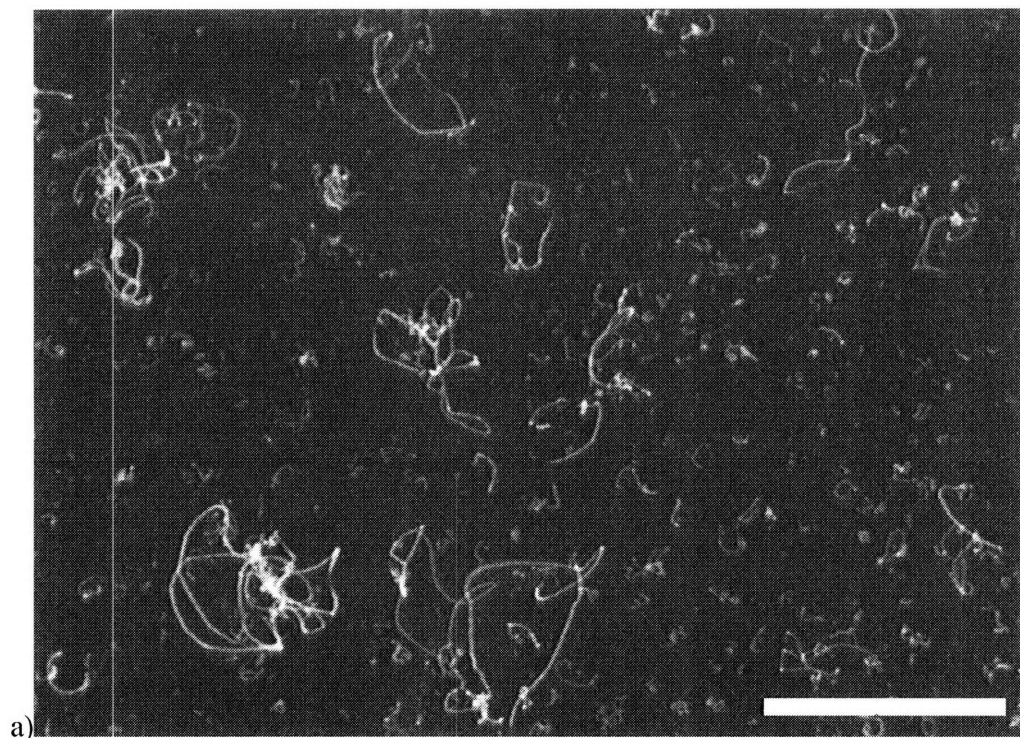
Figure 2-4. TEM images of iron oxide nanoclusters synthesized using: a) cavitated templates, Scale bar = 150 nm; b) non-cavitated templates, Scale bar = 200 nm.

Oxygen plasma etching is an alternative route to thermal degradation to remove the polymer from the substrate surfaces. In the plasma etched samples, the nanoclusters retained their quasi-hexagonal packing over the entire sample surface in all cases. The average diameter of the nanoclusters on the plasma-etched substrates was 10 ± 0.7 nm,

the center-to-center spacing was between 29 – 36 nm, and the density was approximately 10^{11} nanoclusters per cm^2 .

2.3.2 Carbon Nanotube Growth

We carried out CNT growth experiments to determine the catalytic activity of our iron-containing nanocluster arrays in multi-wall CNT (MWCNT) synthesis. Growth times of 10, 30, and 60 min were used. SEM images from the growth process are shown in Figure 2-5 (30 min growth) and Figure 2-6 (60 min growth). In many of the samples, the density of CNT varies on the substrate, so both high and low density regions of CNTs are shown for each sample.



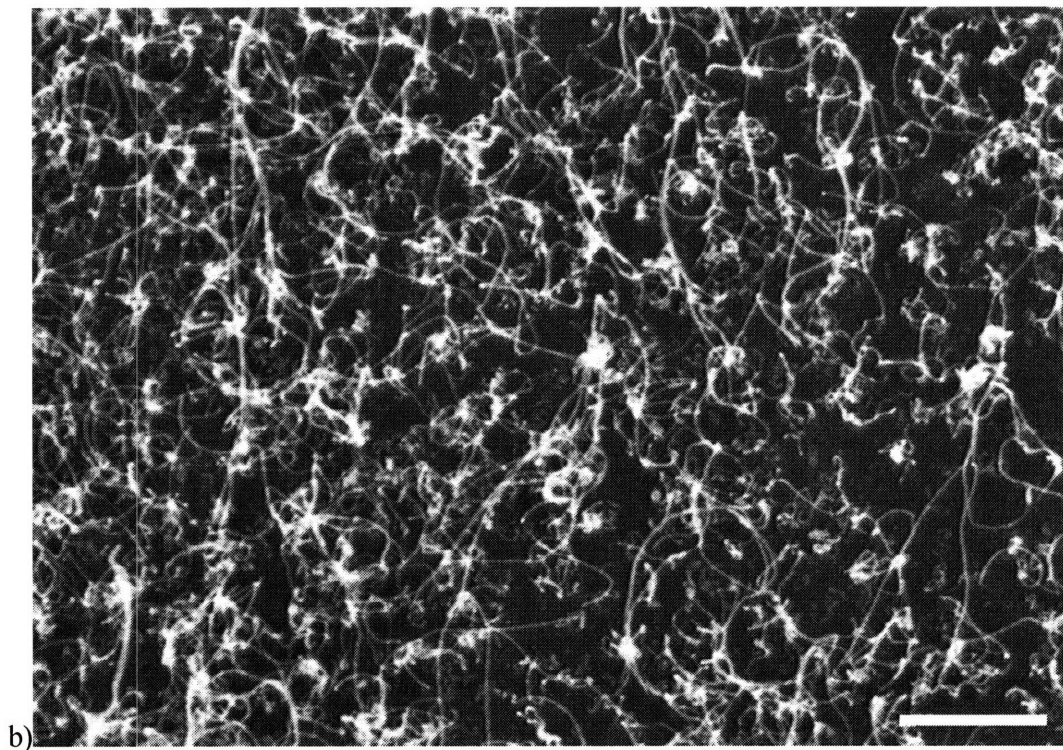
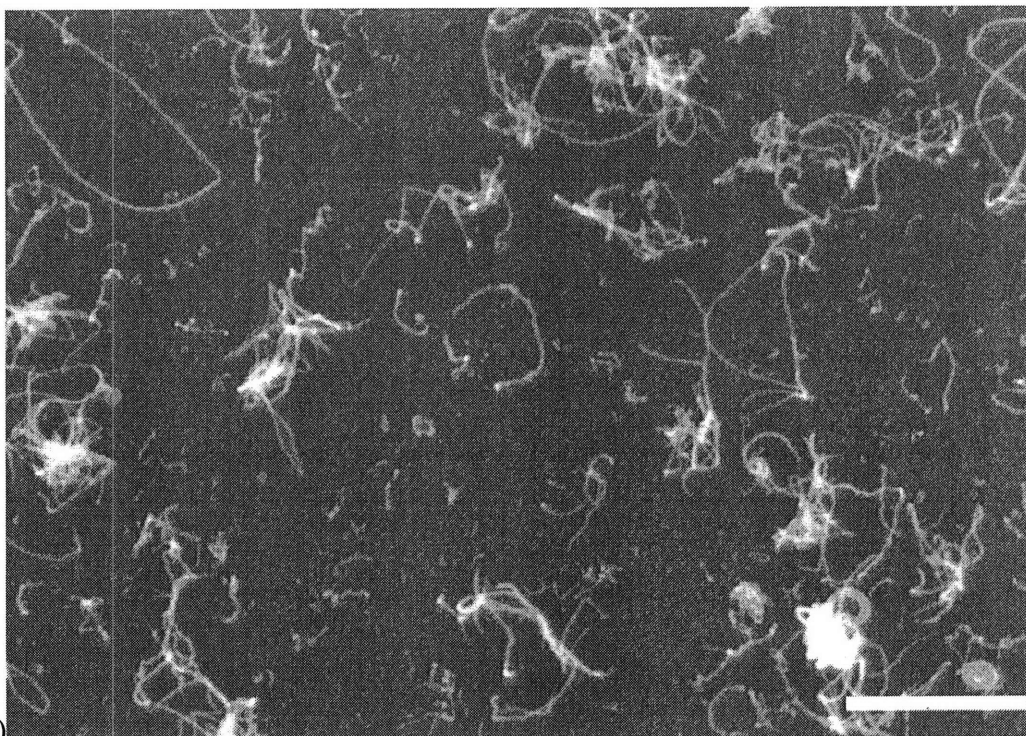
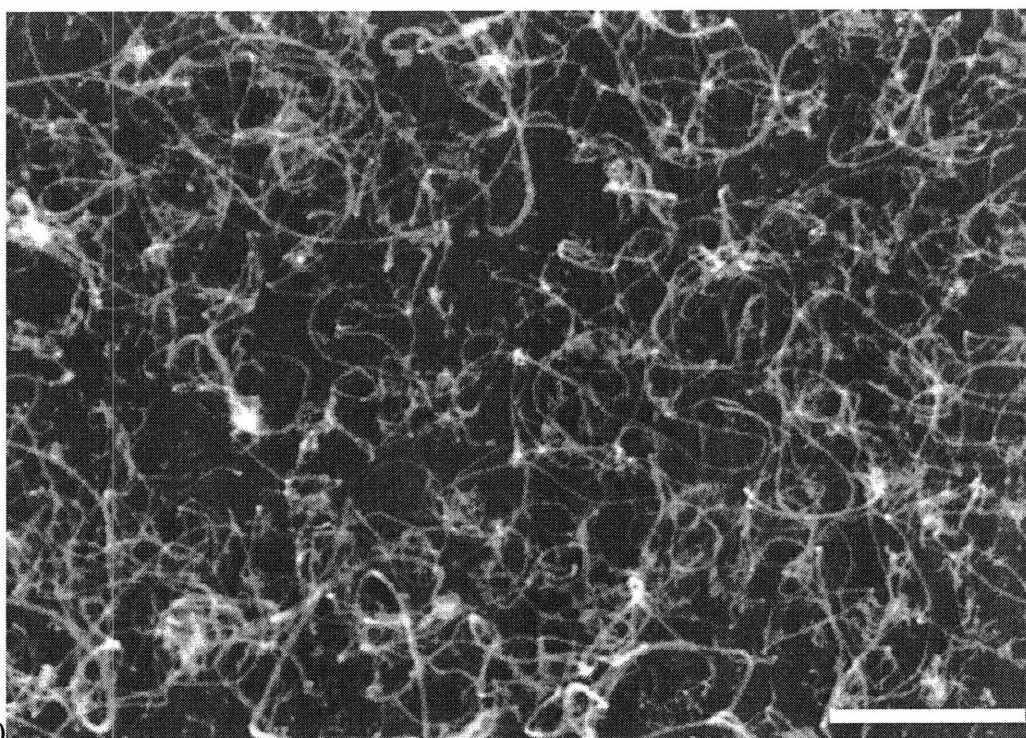


Figure 2-5. SEM images of 30 min CNT growth on an iron oxide nanocluster array created from a cavitated template: a) area of low CNT density on substrate, scale bar = 1 μm ; b) area of high CNT density on substrate, scale bar = 500 nm.



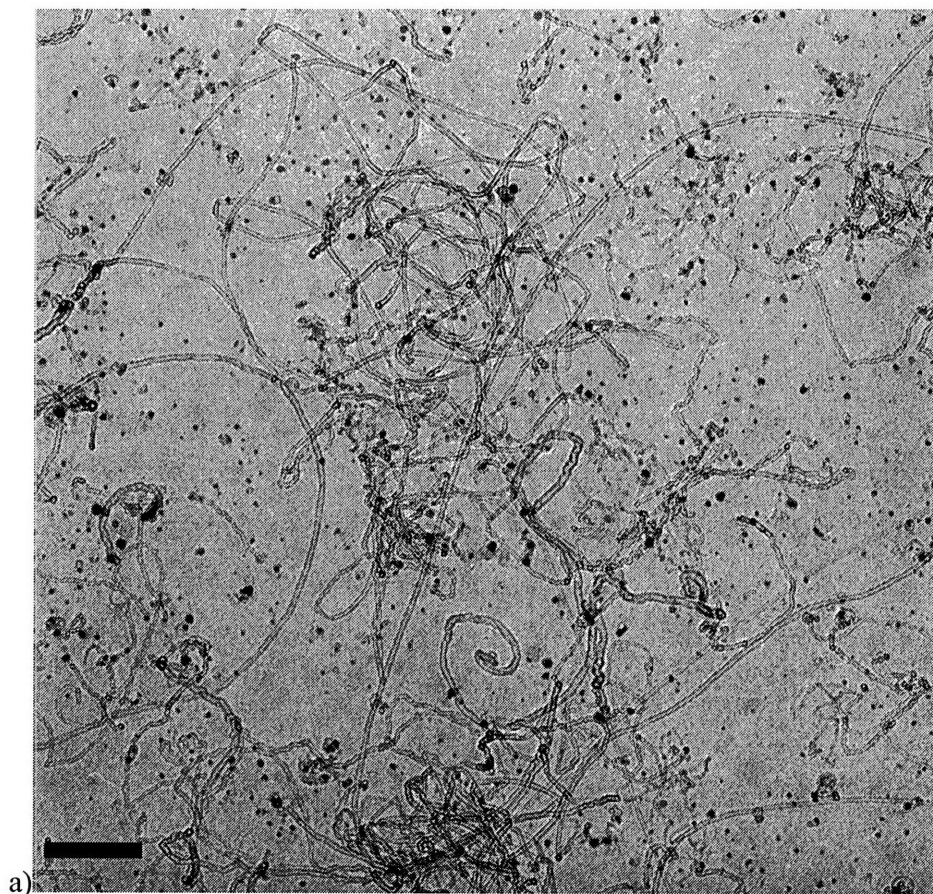
a)



b)

Figure 2-6. SEM image of 60 min CNT growth on an iron oxide nanocluster array created from a cavitated template: a) area of low CNT density on substrate, scale bar = 500 nm; b) area of high CNT density on substrate, scale bar = 500 nm.

Figure 2-7 shows TEM images of the iron-containing nanoclusters and the MWCNTs as grown on the substrate surface. Figure 2-8 shows a high resolution TEM image of a MWCNT synthesized from iron oxide nanoclusters that were created using the block copolymer micellar thin film template on a silicon wafer. After using high resolution TEM to image a random sampling of the synthesized MWCNTs, we determined that the MWCNTs have ~ 8 graphitic layers.



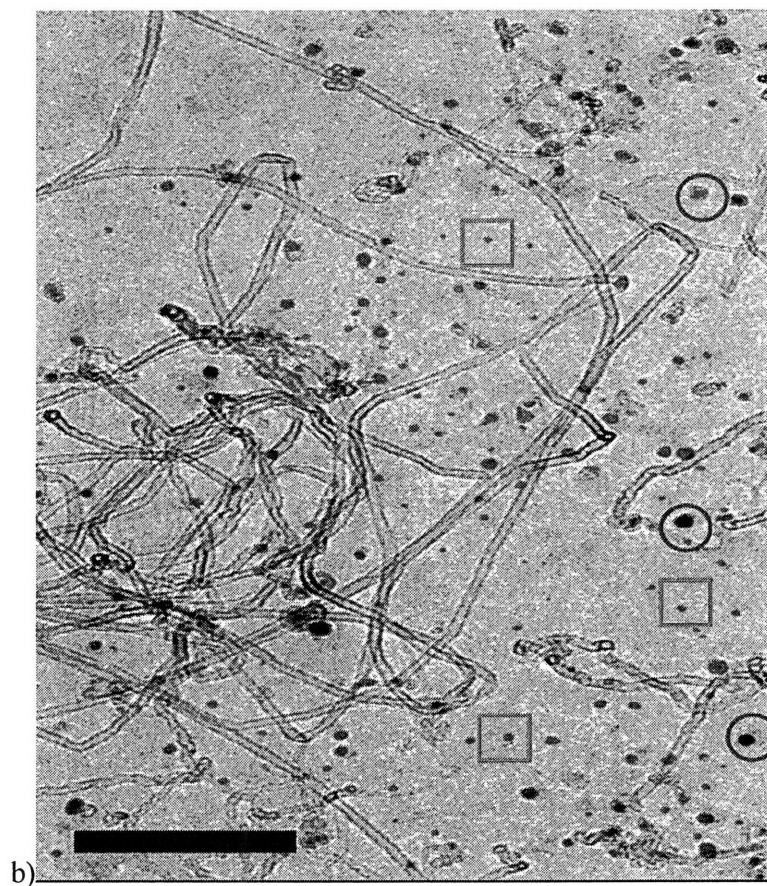


Figure 2-7. TEM images of 60 min CNT growth on an iron oxide nanocluster array created from a cavitated template on a silicon nitride substrate. In a) the Scale bar = 200 nm. In b) circles emphasize examples of nanoclusters with increased diameters after CVD growth (12 – 14 nm), while squares indicate nanoclusters with diameters similar to the pre-CVD nanocluster diameter (7 – 9 nm). Scale bar = 250 nm.

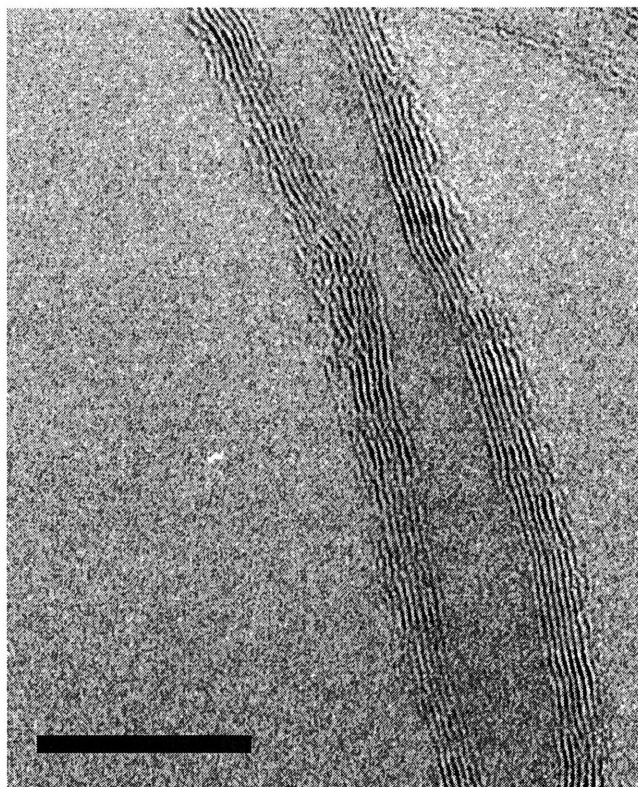


Figure 2-8. High-resolution TEM image of a multi-wall CNT grown from an iron oxide nanocluster on a silicon substrate, Scale bar = 10 nm.

2.4 Discussion

2.4.1 Catalytic Substrates

As mentioned in the sample preparation procedure, alterations were made to the original procedure developed by Boontongkong¹⁴ in order to improve the thin film surface coverage and the subsequent surface coverage of the nanocluster arrays. One adjustment involved increasing the concentration of the block copolymer solution from 2.5 mg/mL to 12.5 mg/mL. By increasing the block copolymer concentration, samples with complete surface coverage were created. Other adjustments were reducing the

molarity of the NaOH solution and decreasing the time the sample was submerged, thereby creating a thin film that retained near complete surface coverage after cavitation.

As shown in Figure 2-4b, some areas of the nanocluster arrays produced from non-cavitated templates contain iron oxide nanoclusters that lose their quasi-hexagonal order. This occurs during the 20 minute 550°C heating step that is used to degrade the organic material of the cluster-containing block copolymer template. Evidently for the case of non-cavitated templates, the elevated temperatures allow for increased surface mobility of the iron-containing nanoclusters, but do not lead to significant amounts of coalescence or ripening of the clusters. The surface densities in Figure 2-4a and 2-4b are both equal to $\sim 10^{11}$ particles per cm^2 and the mean diameter is ~ 7.5 nm in both cases. As mentioned previously, oxygen plasma etching is an alternative route to remove the polymer without the loss of the nanocluster order on the surface.

Figure 2-3, a TEM image of a lead-decorated block copolymer template, serves as a reminder of the useful generality^{14,15} of the metal cation loading scheme for the case of our PS-*b*-PAA block copolymer templates. The same templates employed in the present Fe-based study can be loaded with Ni, Co, and with any combination of these three magnetic metals. There is no need for synthesizing a new metal-containing block copolymer¹³ to study catalytic behavior of these various metals and alloys in CNT growth.

2.4.2 Carbon Nanotube Growth

After characterizing the substrates using both SEM and TEM, it is evident that the proposed block copolymer approach to synthesizing iron-containing nanoclusters, including the use of both cavitated and non-cavitated thin films, is a viable route for the

production of catalysts for CNT growth. We discovered very similar results in the CNT growths using the nanoclusters created from both the cavitated and non-cavitated thin films, so for the remainder of this chapter, the discussions will apply to either synthesis route.

To verify that the catalytic activity of the iron oxide nanoclusters is required to enable CNT growth in our experiments, we attempted to grow CNTs on our control substrate, which was identical to all others except for the omission of the iron loading step. By characterizing the sample using both TEM and SEM (images not shown), we found a total absence of CNT growth, demonstrating the need for iron-containing nanoclusters in our CNT synthesis protocol.

The SEM images show that the average length of the CNTs increase as the growth time is increased. From images of the substrates subjected to a 10 min CNT growth, the average CNT length was estimated to be ~ 100 nm. By examining a substrate after a 60 min CNT growth, shown in Figure 2-6b, it is clear that the CNTs have an average length that is considerably greater than that achieved in 10 minutes of growth. In each of the growth times employed, the CNTs exhibit a broad distribution of lengths, which is common for thermal CVD growth processes¹².

The density of CNTs on the substrate surface also increases with increased CNT growth time. This was qualitatively determined by translating over the substrate surface using SEM. Figure 2-5a (image of low CNT density from the 30 min growth) is representative of about 40% of the substrate surface. The low density areas of the 30 min growth samples correspond to approximately 1 CNT per 100 nanoclusters on the substrate surface, while the higher density areas correspond to approximately 1 CNT per

10 nanoclusters. In contrast to the 30 min growth, Figure 2-6a (image of low CNT density from the 60 min growth), represents less than about 25% of the substrate surface. In the 60 min growth, the particles lose their hexagonal arrangement (as demonstrated in the TEM image of Figure 2-7), and therefore it is exceedingly difficult to estimate the ratio of CNTs to nanoclusters.

Based on a variety of SEM images similar to Figures 2-5 and 2-6, the average CNT diameter is 11.9 ± 1.5 nm, which is larger than the nanocluster diameter of 7.5 ± 0.8 nm determined from TEM. This is an unexpected result, because previous research¹⁰ has shown that CNTs have diameters slightly smaller than the diameters of the nanoclusters from which they are catalyzed.

Although the SEM images allow for determining trends in the CNT growths, the TEM images of the substrates give a clearer view of the CNT growth and allow for a better quantification of the size of the CNTs relative to the catalytic iron oxide nanoclusters. From the TEM images in Figure 2-7, the average CNT diameter is 11.8 ± 0.7 nm, which agrees closely with the data from the SEM images. The TEM image also reveals polydispersity in the post-CVD iron-containing nanocluster diameters that was not seen in the originally-templated nanocluster precursors. As illustrated in Figure 2-7b, there is a population of noticeably larger nanoclusters (some are labeled with circles in Figure 2-7b) with diameters of $\sim 12 - 14$ nm, scattered among the smaller nanoclusters (some are labeled with squares in Figure 2-7b) with diameters between $\sim 7 - 9$ nm. Examining numerous TEM images like Figure 2-7 leads to the conclusion that very few of the smaller nanoclusters have successfully catalyzed CNT growth, and most of the CNTs have diameters closely matched to the larger nanocluster diameters. The process

by which these larger nanoclusters form is currently unclear, but a possible mechanism might involve the precursor (7.5 nm diameter) nanoclusters initially increasing in size by absorbing carbon atoms to create larger nanoclusters (12 - 14 nm diameter), followed by carbon precipitation and CNT growth. We do not believe that the smaller nanoclusters fuse to form larger nanoclusters during the high temperature CNT growth process because the absence of any change in the number of nanoparticles per unit area does not support this latter idea.

From the TEM images in Figure 2-7, it is clear that the catalytic iron-containing nanoclusters lose their quasi-hexagonal array over time while exposed to the growth conditions. For the 10 min CNT growth, the TEM image in Figure 2-9 clearly shows that the iron-containing nanoclusters remain in their quasi-hexagonal arrays. After the growth time is increased to 60 min, the nanocluster quasi-hexagonal arrays appear to be disrupted, as seen in Figure 2-7. It is unclear at this time whether the disruption of the nanocluster arrays is caused explicitly by the CNT growth process, or if the exposure to high temperature (750°C) in the CVD growth process plays a central role.

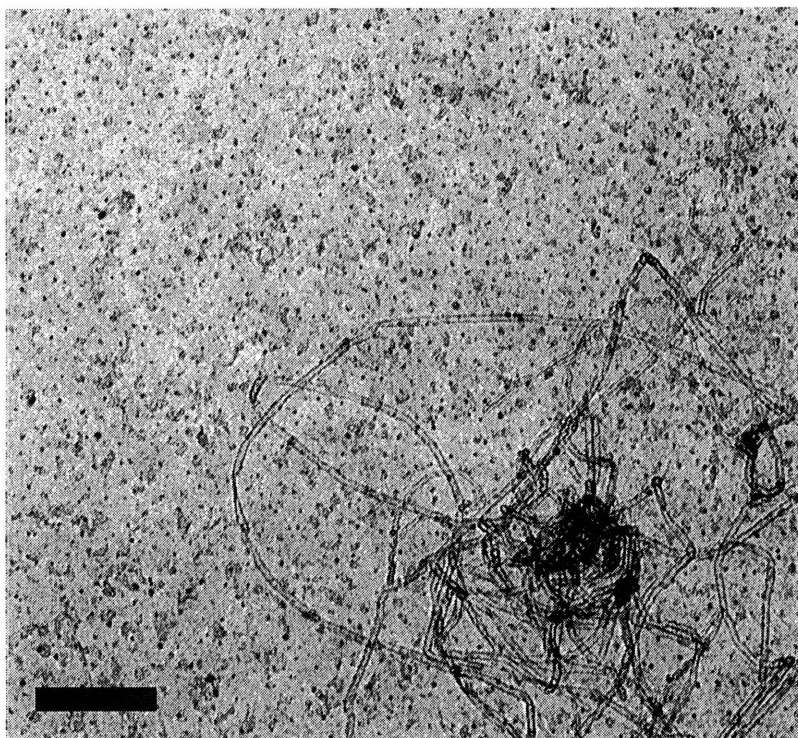


Figure 2-9. TEM image of a 10 min CNT growth using iron oxide nanoclusters synthesized from a cavitated template on a silicon nitride substrate, Scale bar = 100 nm.

From examining both the SEM and TEM images, we are unable to determine conclusively whether the growth mechanism is tip-growth or base-growth. For a base-growth mechanism to dominate, the iron nanoclusters must interact strongly with the substrate and the nanoclusters must remain on the substrate throughout the growth process. We believe that this growth is catalyzed from the tip of the CNT because the nanoclusters do not appear to be strongly bound to the surface, as demonstrated in Figure 2-7, where the iron-containing nanoclusters lose their quasi-hexagonal array during the 60 minute growth process.

In future work, we plan to examine more closely the possible distinctions between the CNTs produced using nanoclusters created from either cavitated or non-cavitated thin films. We also plan on using scanning transmission electron microscopy and energy dispersive X-ray analysis to determine the elements present within the iron-containing nanoclusters after growth, which will help us to better understand the mechanism for the increase in nanocluster diameter. A distinct advantage of this synthesis procedure is the ability to synthesize arrays of different metal-containing nanoclusters from a single block copolymer precursor template. As mentioned above, we plan to utilize this capability to create arrays of other metals known to be catalytically active in CNT growth, such as Ni and Co. We also plan to use these templates to create gold nanocluster arrays for possible applications in the synthesis of zinc oxide nanowires.

2.5 Conclusion

In this chapter, we have demonstrated the ability to create iron-containing nanoclusters with near monodisperse diameters in partially-ordered lateral arrays using block copolymer micellar thin films. By varying the spin-casting variables and the concentration of the block copolymer solution, we succeeded in producing a micellar thin film, and subsequently an iron-containing nanocluster array covering more than 90% of the substrate surface. After synthesizing these iron-containing nanoclusters on both silicon nitride and silicon substrates, we used a thermal CVD process to demonstrate their catalytic activity in MWCNT synthesis. By using silicon nitride membrane window grids as substrates, we were able to characterize the as-grown carbon nanotubes and the catalytic metal nanoclusters while still attached to the substrate surface using TEM. The

block copolymer template offers the possibility of tuning the size and spacing of the metal nanoclusters by altering the block copolymer chain length and composition. It is also straightforward to create nanocluster arrays of different metal species.

2.6 References

1. Iijima, S. *Nature* **1991**, 354, 56-58.
2. DeHeer, W. A.; Chatelain, A.; Ugarte, D. *Science* **1995**, 270, 1179-1180.
3. Dillon, A. C.; Jones, K. M.; Bekkedahl, T. A.; Kiang, C. H.; Bethune, D. S.; Heben, M. J. *Nature* **1997**, 386, 377-379.
4. Tans, S. J.; Verschueren, A. R. M.; Dekker, C. *Nature* **1998**, 393, 49-52.
5. Ren, Z. F.; Huang, Z. P.; Xu, J. W.; Wang, J. H.; Bush, P.; Siegal, M. P.; Provencio, P. N. *Science*, **1998**, 282, 1105-1107.
6. Huang, Z. P.; Wang, D. Z.; Wen, J. G.; Sennett, M.; Gibson, H.; Ren, Z. F. *App. Phys. A* **2002**, 74, 387-391.
7. Hofmann, S.; Ducati, C.; Robertson, J.; Kleinsorge, B. *App. Phys. Lett.* **2003**, 83, 135-137.
8. Huang, Z. P.; Carnahan, D. L.; Rybczynski, J.; Giersig, M.; Sennett, M.; Wang, D. Z.; Wen, J. G.; Kempa, K.; Ren, Z. F. *App. Phys. Lett.* **2003**, 82, 460-462.
9. Tu, Y.; Huang, Z. P.; Wang, D. Z.; Wen, J. G.; Ren, Z. F. *Appl. Phys. Lett.* **2002**, 80, 4018-4020.
10. Cheung, C. L.; Kurtz, A.; Park, H.; Lieber, C. M. *J. Phys. Chem. B*, **2002**, 106, 2429-2433.
11. Choi, H. C.; Kundaria, S.; Wang, D. W.; Javey, A.; Wang, Q.; Rolandi, M.; Dai, H. J. *Nano Lett.* **2003**, 3, 157-161.
12. Li, Y. M.; Kim, W.; Zhang, Y. G.; Rolandi, M.; Wang, D. W.; Dai, H. J. *J. Phys. Chem. B* **2001**, 105, 11424-11431.
13. Hinderling, C.; Keles, Y.; Stockli, T.; Knapp, H. F.; de los Arcos, T.; Oelhafen, P.; Korczagin, I.; Hempenius, M. A.; Vancso, G. J.; Pugin, R.; Heinzelmann, H. *Adv. Mater.* **2004**, 16, 876-879.

14. Boontongkong, Y.; Cohen, R. E. *Macromolecules* **2002**, *35*, 3647-3652.
15. Clay, R. T.; Cohen, R. E. *Supramol. Sci.* **1998**, *5*, 41-48.
16. Khougaz, K.; Zhong, X. F.; Eisenberg, A. *Macromolecules* **1996**, *29*, 3937-3949.
17. Wiese, H.; Rupaner, R. *Colloid Polym. Sci.* **1999**, *277*, 372-375.

Chapter 3 Strategies for Controlling the Planar Arrangement of Block Copolymer Micelles and Inorganic Nanoclusters*

3.1 Introduction

In the past decade, the use of self-assembling systems for the fabrication of materials on the nanometer scale has been an active area of research¹, with possible applications in areas such as data storage, electronics, and molecular separation². Block copolymer thin films are nano-scale self-assembling systems³⁻⁸ that have been exploited due to their intrinsic nanometer feature size, their ease of synthesis, and their rich phase behavior^{9,10}. Block copolymer lithography³ is an example that uses the heterogeneous morphology of block copolymer thin films to transfer periodic arrays of features onto a substrate on a nanometer length scale. Generally, solvent cast block copolymer films are annealed on the substrate to generate an equilibrium morphology and to reduce the occurrence of unwanted grain boundaries and other defects.

A related but different route for patterning on the nano-scale utilizes amphiphilic block copolymer micellar solutions to produce ultra-thin nanostructured films. These micellar systems, which have frequently been based on poly(styrene-*block*-2-vinylpyridine), have been utilized for various applications, including nanolithography based on gold-loaded micelles¹¹, deposition of gold nanocluster arrays for ZnO nanowire

growth¹² and protein binding¹³, and deposition of iron oxide nanocluster arrays for carbon nanotube growth¹⁴. Previous work in our research group used block copolymer micellar thin films based on poly(styrene-*block*-acrylic acid) to create arrays of PAA domains that could be cavitated to expose free carboxylic acid groups¹⁵. These systems have been used to generate planar arrays of various inorganic nanoclusters¹⁵ including iron oxides suitable for catalyzing carbon nanotube growth¹⁶. One advantage of the micellar route to generate such planar nano-arrays arises from the fact that these systems are often trapped in a non-equilibrium state, facilitating the opportunity to vary structural parameters such as the characteristic shape, size, and spacing of the array features.

In this chapter, we focus on strategies to vary the size and spacing of spherical block copolymer micellar domains on planar surfaces, as well as routes that allow for nanocluster synthesis within the spherical domains. Our specific approach capitalizes on the ability of the amphiphilic block copolymer, poly(styrene-*block*-acrylic acid) (PS-*b*-PAA) to form quasi-hexagonal planar arrays of PAA spheres in a matrix of PS. As shown previously^{15,16}, it is possible to exploit the metal-binding properties of the carboxylic acid groups in chemical synthesis schemes that are confined to nanometer-scale reaction zones. Application of these nanoreactor synthesis protocols ideally requires a measure of control over the size, spacing, and packing arrangement of these reaction zones on the planar substrate. The present chapter addresses some of these issues using a variety of strategies, including: varying the block copolymer molecular weight, adding homopolymer of PS into the micellar solution, and also by the combination of different micellar solutions.

This chapter also presents a novel route for creating metal nanocluster arrays containing more than one inorganic species, with each nanocluster containing either one or all of the inorganic species, depending on the conditions of the synthesis. This route focuses on the time-dependent inter-diffusion of inorganic species following mixing of micelle solutions that have been previously loaded with different inorganic species. These arrays are characterized using energy dispersive x-ray (EDX) analysis on a scanning transmission electron microscope (STEM).

3.2 Experimental Section

3.2.1 Materials

Three PS-*b*-PAA copolymers were used in this work, with molecular weights and nomenclatures as follows: PS-*b*-PAA (16.4/4.5) [M_n (PS) = 16 400 g/mol, M_n (PAA) = 4 500 g/mol, PDI = 1.05]; PS-*b*-PAA (66.5/4.5) [M_n (PS) = 66 500 g/mol, M_n (PAA) = 4 500 g/mol, PDI = 1.07]; and PS-*b*-PAA (11.0/1.2) [M_n (PS) = 11 000 g/mol, M_n (PAA) = 1 200 g/mol, PDI = 1.11]. The copolymers were used as received from Polymer Source, Inc. A homopolymer of polystyrene (PS) (M_n = 8 500 g/mol, PDI = 1.06) was used as received from Polymer Source, Inc. The following chemicals were also used as received: anhydrous iron(III) chloride (FeCl_3) obtained from Sigma-Aldrich Co., lead(II) acetate trihydrate (PbAc_2) obtained from Sigma-Aldrich Co., sodium hydroxide (98.9%) obtained from Mallinckrodt, and toluene (HPLC grade, 99.8%) obtained from Sigma-Aldrich Co.

The silicon nitride membrane window substrates were purchased from Structure Probe, Inc. Each substrate (surface area $\sim 4.5 \text{ mm}^2$) consisted of a 100-nm-thick

amorphous, low-stress Si_3N_4 membrane supported on a 0.2-mm-thick silicon wafer that had been back-etched in the center to create the electron transparent Si_3N_4 window (surface area $\sim 0.2 \text{ mm}^2$). The use of the electron-transparent silicon nitride substrates allows for direct TEM characterization without disturbing the spin-cast films. Each substrate was rinsed with toluene prior to film casting. All aqueous solutions were made using deionized water ($> 18 \text{ M}\Omega \text{ cm}$, Millipore Milli-Q).

3.2.2 Sample Preparation

To produce the metal-loaded micellar arrays we employed a variety of synthesis procedures that capitalize on the micellar organization of PS-*b*-PAA in toluene solution. A summary of the processing routes is shown in Figure 3-1 and outlined below.

In route i), three different molecular weights of PS-*b*-PAA (listed in the Materials section) were mixed with toluene at a concentration of 12.5 – 15 mg/mL, all of which resulted in a slightly cloudy solution. After heating these solutions to $\sim 145^\circ\text{C}$ for 20 min, the solutions became optically clear, and they remained clear after cooling to room temperature. Previous work¹⁵ has shown that this transition in solution optical properties is the result of a change from (equilibrium) cylindrical to (kinetically trapped) spherical block copolymer micelles. The PAA micelle cores were then selectively loaded with the chosen metal by adding the metal species to the micellar solution at a ratio of 5.4 metal ion equivalents per carboxylic acid group (metal loading ratio). Thin films were then created by spin-casting the metal-loaded micellar solutions onto the planar substrates at between 6000 – 8000 rpm for one minute at room temperature.

In route ii), PS-*b*-PAA (16.4/4.5) was mixed with toluene at a concentration of 12.5 – 15 mg/mL. The chosen metal was then added at three different metal loading

ratios (0.3, 5.4, and 15). Thin films of each solution were then produced by spin-casting the solution onto the substrates.

In route iii), PS homopolymer ($M_n = 8\,500$ g/mol) was added to the micellar solutions (metal loading ratio 5.4) based on the PS-*b*-PAA (16.4/4.5) system. Homopolymer was added in quantities leading to solutions in which the molar ratio of molecules of PS homopolymer to PS-*b*-PAA block copolymer [PS : PS-*b*-PAA] was equal to 4 and 10, respectively. To reduce the viscosities of these solutions to acceptable levels for spin-casting, the solutions were diluted with toluene from 13 mg PS-*b*-PAA /mL toluene to 5 mg PS-*b*-PAA /mL toluene. Thin films were then produced by spin casting these solutions onto substrates.

In route iv), metal-loaded micellar solutions were combined with either an unloaded micellar solution (micelle solution that bypassed the metal loading step) or a micelle solution that had been loaded with a different metal species. In the first example, a micelle solution of PS-*b*-PAA (16.4/4.5) with a metal loading ratio of 5.4 was mixed in a 1:1 volume ratio with an unloaded micelle solution of the same PS-*b*-PAA copolymer. After the combined solutions had been mixed for 1 min, a thin film was spin-cast onto a substrate. In the second example, a micelle solution of PS-*b*-PAA (16.4/4.5) with an FeCl₃ loading ratio of 0.3 was mixed in a 1:1 volume ratio with a micelle solution of PS-*b*-PAA (16.4/4.5) with a PbAc₂ loading ratio of 0.9. Thin films were then created by spin casting this mixed micellar solution onto a substrate after mixing the solutions for a short time (2 min) and an extended time (120 hr).

In each of the routes above, there exists the possibility of bypassing the metal loading step (step ii in Figure 3-1) to create arrays of PAA domains within a PS matrix.

From previous research it is known that treating these films in a basic solution containing a monovalent cation results in significant swelling of the PAA domains¹⁵, which eventually leads to localized cavitation that exposes the interior of the PAA domains to the surface.

In each of the routes listed above, the polymer thin film was removed by oxygen plasma etching (RF plasma, 8 – 12 MHz) for 15 min, leaving only the inorganic species remaining on the substrate. The inorganic nanocluster arrays were then characterized using TEM, atomic force microscopy (AFM), and STEM.

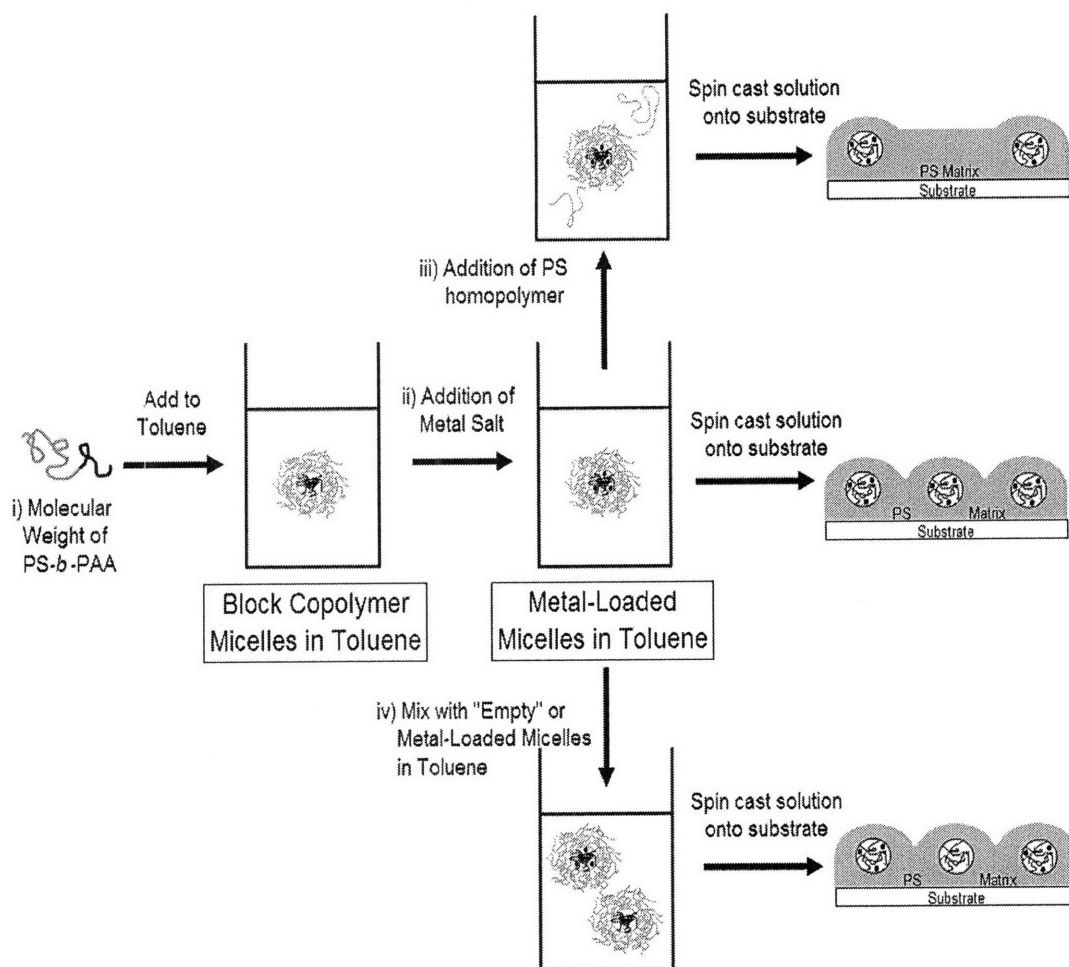


Figure 3-1. Diagram of synthesis procedures for modification of block copolymer micellar thin films.

3.2.3 *Microscopy and Spectroscopy*

TEM was performed on a JEOL 200CX operating at 200 kV and a JEOL 2000FX operating at 200 kV. STEM was performed on a VG HB603 operating at 250 kV. AFM was performed on a Digital Instruments Dimension 3000 Nanoscope IIIA scanning probe microscope operating in tapping mode using a silicon cantilever. Dynamic Light Scattering (DLS) was performed on a BI-9000AT Digital Autocorrelator (Brookhaven Instruments Corporation) using a 514 nm laser, at $\theta = 90^\circ$ and a temperature of 25°C. X-ray photoelectron spectroscopy (XPS) was performed with a Kratos AXIS Ultra Imaging Spectrometer.

3.3 Results and Discussion

The TEM images in Figure 3-2a through 3-2c show nanocluster arrays that have been created by spin-casting a micellar solution with different metal loading ratios onto a planar substrate followed by oxygen plasma etching to remove the polymer thin film. These images illustrate the effect of the metal loading ratio on the size and spacing of the metal nanocluster arrays. In each of these images, PS-*b*-PAA (16.4/4.5) was the block copolymer and FeCl₃ was the selected metal salt. In Figure 3-2a, FeCl₃ was added to the block copolymer micellar solution at a loading ratio of approximately 0.3, leaving an excess of carboxylic acid groups relative to the amount of iron cation. In Figure 3-2a, the iron oxide nanoclusters have diameters of 8 ± 0.7 nm, a center-to-center spacing of

approximately 40 ± 4 nm, and an areal density of 8×10^{10} nanoclusters per cm^2 . In Figure 3-2b, the FeCl_3 loading ratio is increased to approximately 5.4, i.e. there is a significant excess of iron compared to the available carboxylic acid groups. In this image, the iron oxide nanoclusters have diameters of 16.0 ± 1.6 nm, a center-to-center spacing of approximately 45 ± 4 nm, and an areal density of approximately 6×10^{10} nanoclusters per cm^2 . The diameter of the iron oxide nanoclusters approximately doubles as a result of the increased FeCl_3 loading ratio. The center-to-center spacing increases only slightly due to the increased metal loading ratio, and the variation roughly corresponds to the increase in the diameter of the nanoclusters. In Figure 3-2c, the FeCl_3 loading ratio is increased to approximately 15, and the iron oxide nanoclusters have diameters of 16.2 ± 1.1 nm, a center-to-center spacing of approximately 45 ± 4 nm, and an areal density of roughly 6×10^{10} nanoclusters per cm^2 . By comparing the nanocluster arrays formed from an FeCl_3 loading ratio of 5.4 vs. an FeCl_3 loading ratio of 15, it is clear that very little change occurs in the size or spacing of the metal nanocluster arrays, owing to the saturation of the loading capacity of the micelles. This result is supported by our observation of undissolved FeCl_3 precipitate remaining in the solutions with a metal loading ratio of 15, while no FeCl_3 precipitate remains in the solutions with a metal loading ratio of 0.3. A summary of the data for Figures 3-2a through 3-2c is shown in Table 3-1. By varying the metal loading ratio in solution, we have demonstrated the ability to exhibit a degree of control over the diameter of the metal nanoclusters that are formed at essentially constant spacing.

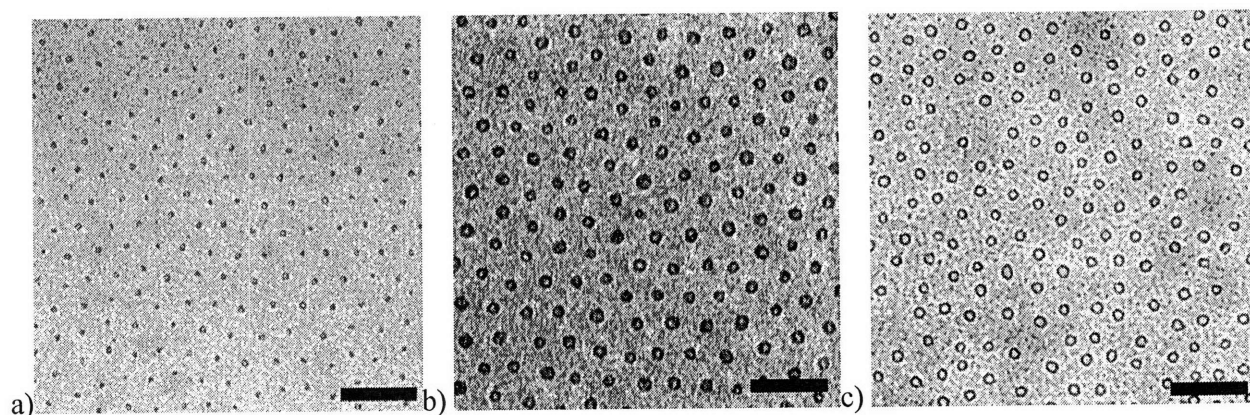


Figure 3-2. TEM images of iron oxide nanocluster arrays synthesized from micellar thin films using PS-*b*-PAA (16.4/4.5) with a FeCl₃ loading ratio of: (a) 0.3; (b) 5.4; (c) 15.

Scale bar = 100 nm.

<u>PS</u>	<u>PAA</u>	<u>Metal Loading</u>		<u>C-to-C spacing</u>		<u>Areal</u> <u>Density</u>
		<u>Ratio</u>	<u>Diameter</u>	(Measured) ^a	(FFT) ^b	
(g/mol)	(g/mol)		(nm)	(nm)	(nm)	(part/cm ²)
16 400	4 500	0.3	8 ± 0.7	39.6 ± 4.1	35.8	8.2E+10
16 400	4 500	5.4	16.0 ± 1.6	44.9 ± 4.0	39.5	6.0E+10
16 400	4 500	15	16.2 ± 1.1	44.8 ± 4.2	38.1	6.3E+10

Table 3-1. Effects of varying metal loading ratio on diameter, center-to-center spacing, and areal density of iron oxide nanocluster arrays.

^aFrom TEM images. ^bDetermined from Fast Fourier Transform (FFT) of TEM image.

From the TEM images in Figure 3-2, it is apparent that the nanoclusters have a higher contrast around the exterior and considerably less contrast within the center of the

nanocluster. We feel confident that this effect is caused by phase contrast in TEM imaging and is not representative of the actual structure of our nanoclusters. Because these nanoclusters offer very little amplitude contrast, we are forced to take steps to increase the contrast in order to produce useful images. We accomplish this by under-focusing our sample in order to image the nanoclusters using phase contrast. When the nanoclusters are over-focused, the center of the nanoclusters appear dark and the exterior appears bright, which is a common indicator of phase contrast effects. When the nanoclusters are in focus, this effect is eliminated, but the images are extremely difficult to view due to the lack of contrast. This explanation is also confirmed by the annular dark field (ADF) image of the nanoclusters, which is shown subsequently in Figure 3-6b. If the nanoclusters were hollow, we would observe a bright ring with a dark center for each nanocluster in the ADF image; however, it is clear from Figure 3-6b that each nanocluster appears as a uniform bright circle. We also imaged these nanoclusters using AFM (image not shown), which confirmed that the nanoclusters were approximately spherical in shape, and did not contain a cavity as the TEM images in Figure 3-2 might suggest.

We also characterized the substrates using x-ray photoelectron spectroscopy (XPS) to determine the chemical composition of the nanoclusters. As shown in Figures 3-3 and 3-4, the nanoclusters exhibited a Fe ($2p^{3/2}$) peak at approximately 711.7 eV and an O (1s) peak at approximately 530.7 eV. Comparing these values to literature values for various iron oxides, we are able to conclude that the nanoclusters are either Fe₂O₃ [Fe ($2p^{3/2}$) ~ 710.9 – 711.6 eV and O (1s) ~ 529.6 – 530.3 eV] or FeOOH [Fe ($2p^{3/2}$) ~ 711.0 – 711.8 eV and O (1s) ~ 530.1 – 530.5 for the oxide oxygen, O (1s) ~ 531.4 –

531.8 eV for the hydroxide oxygen]¹⁷, or a combination of the two species. Because our nanoclusters are on silicon oxide, the O (1s) peak caused by the Si-O bond makes it extremely difficult to examine more closely the O (1s) peak associated with the nanoclusters to determine if there are two different oxygen peaks.

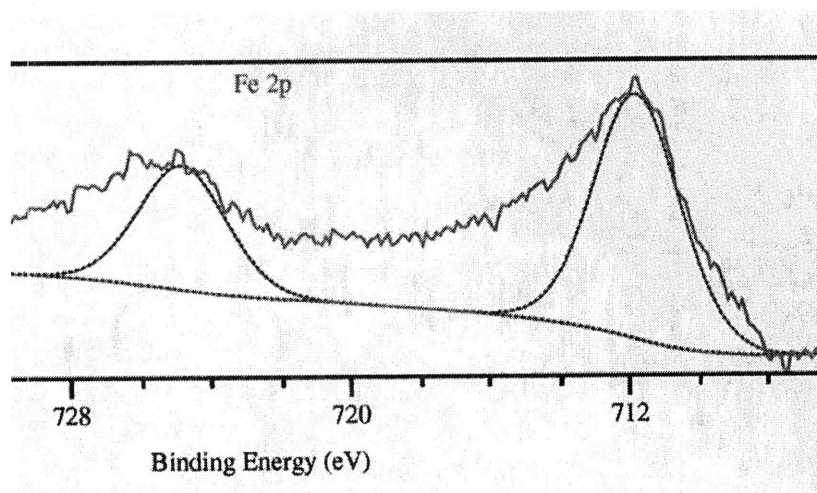


Figure 3-3. Fe 2p XPS spectra for iron oxide nanocluster arrays synthesized from micellar thin films using PS-*b*-PAA (16.4/4.5) with a FeCl₃ loading ratio of 5.4.

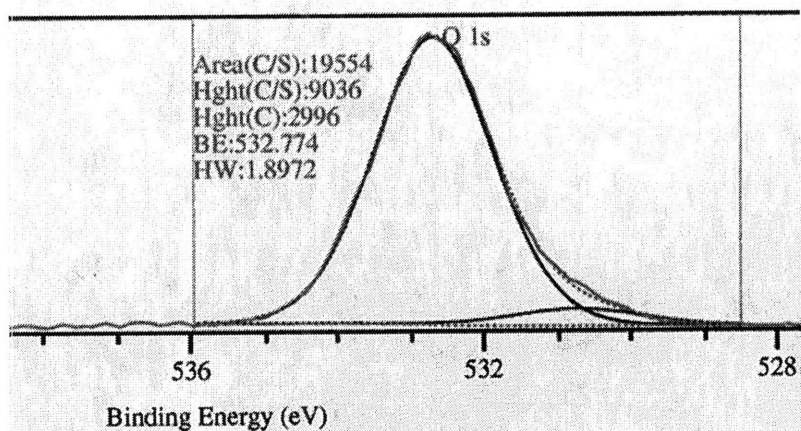


Figure 3-4. O 1s XPS spectra for iron oxide nanocluster arrays synthesized from micellar thin films using PS-*b*-PAA (16.4/4.5) with a FeCl₃ loading ratio of 5.4.

The TEM images in Figure 3-5a through 3-5c demonstrate the effect of the molecular weight of PS-*b*-PAA on the size and spacing of the PAA domains, and consequently on the size and spacing of the resulting nanoclusters. In Figure 3-5a, micelles formed from PS-*b*-PAA (11.0/1.2) with a FeCl₃ loading ratio of 5.4 led to iron oxide nanoclusters with diameters of 4.7 ± 0.6 nm, a center-to-center spacing of 13 ± 1.7 nm, and an areal density of approximately 3×10^{11} nanoclusters per cm². Figure 3-5b shows iron oxide nanoclusters with diameters of 16 ± 1.6 nm, a center-to-center spacing of approximately 45 ± 4 nm, and an areal density of approximately 6×10^{10} nanoclusters per cm² that resulted from similar processing conditions for the case of the PS-*b*-PAA (16.4/4.5) copolymer. At constant loading ratio, decreasing the molecular weight of the PAA block leads to smaller nanoclusters, while decreasing the length of the PS block leads to smaller center-to-center spacing. Micelles of PS-*b*-PAA (66.5/4.5), again using a loading ratio of 5.4, were used to create iron oxide nanoclusters with diameters of 11.2 ± 1.1 nm, a center-to-center spacing of 57.6 ± 8.2 nm, and an areal density of approximately 4×10^{10} nanoclusters per cm². Increasing the PS segment of the block copolymer four-fold enlarged the center-to-center spacing of the PAA domains by approximately 30% (Figures 3-5b and 3-5c), and even though the PAA block length remained constant ($M = 4500$ g/mol), the cluster size also decreased (from 16 nm to 11 nm). These trends result from a decrease in aggregation number of the micelles caused by the increase in the molecular weight of the PS segment, a result that has been previously shown by Khougaz *et al*¹⁸. The three TEM images in Figure 3-5 demonstrate a method for controlling the size and spacing of the PAA micellar domains, which leads to control over the size and spacing of metal nanocluster arrays, as summarized in Table 3-2.

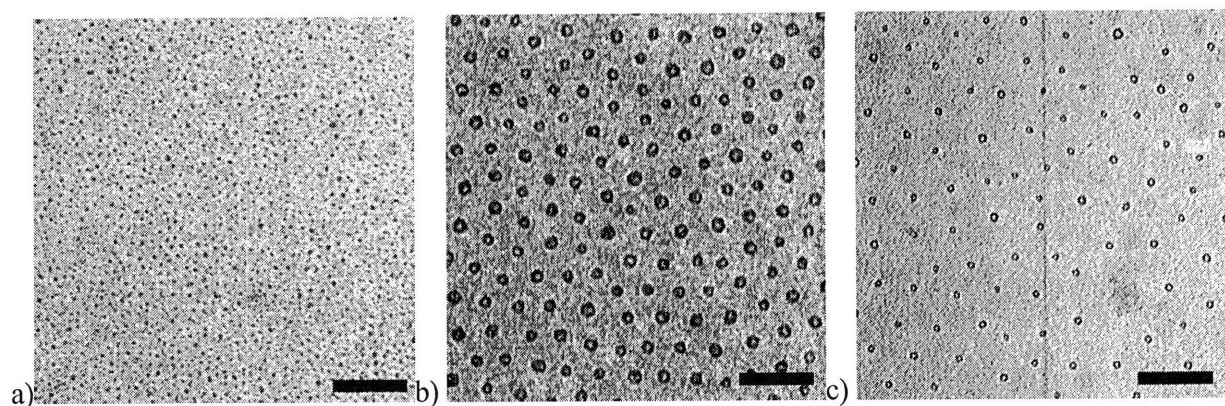


Figure 3-5. TEM images of iron oxide nanocluster arrays synthesized from micellar thin films with a FeCl_3 loading ratio of 5.4 and PS-*b*-PAA with a molecular weight of: (a) 11/1.2; (b) 16.4/4.5; (c) 66.5/4.5. Scale bar = 100 nm.

<u>PS</u> (g/mol)	<u>PAA</u> (g/mol)	<u>Hydrodynamic</u>		<u>C-to-C spacing</u>		<u>Areal</u> <u>Density</u> (part/cm ²)
		<u>Radius (R_h)</u>	<u>Diameter</u> (nm)	<u>(Measured)^a</u> (nm)	<u>(FFT)^b</u> (nm)	
11 000	1 200	27 nm	4.7 ± 0.6	13 ± 1.7	12	$3.0\text{E}+11$
16 400	4 500	44 nm	16.0 ± 1.6	44.9 ± 4.0	39.5	$6.0\text{E}+10$
66 500	4 500	96 nm	11.2 ± 1.1	57.6 ± 8.2	56	$4.3\text{E}+10$

Table 3-2. Effects of varying the molecular weight of PS-*b*-PAA on diameter, center-to-center spacing, and areal density of iron oxide nanocluster arrays.

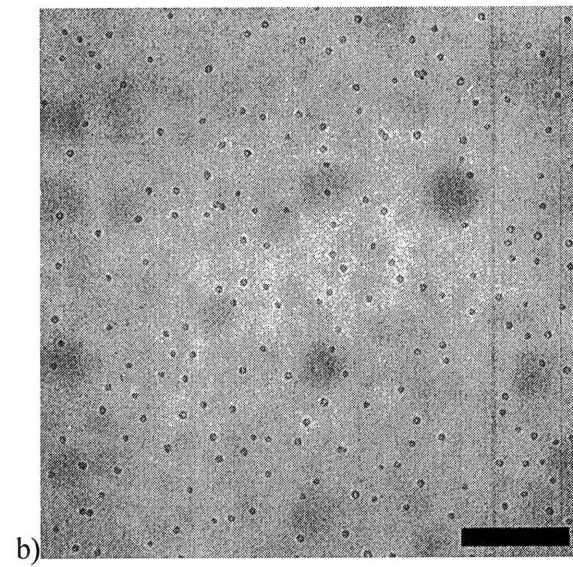
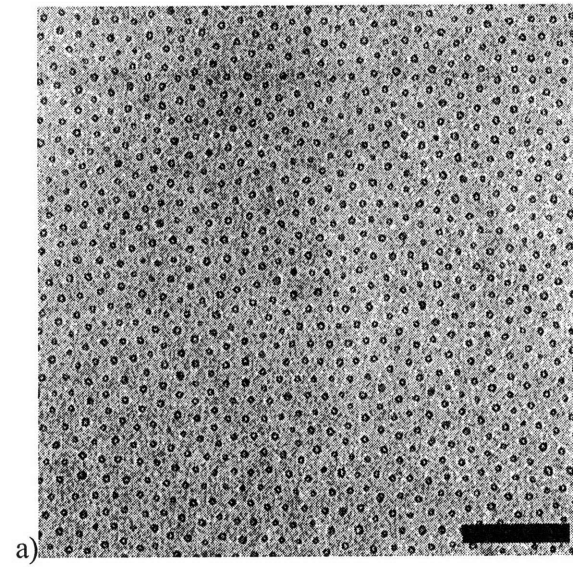
^aFrom TEM images. ^bDetermined from Fast Fourier Transform (FFT) of TEM image.

The variation of center-to-center spacing between the metal nanoclusters caused by the alteration of the block copolymer molecular weight also correlated with changes in the size of the micelles in solution, as verified by DLS. An average hydrodynamic radius

was determined for each micellar solution and results are shown in Table 3-2. The average hydrodynamic radii were 27 nm, 44 nm, and 96 nm, for the PS-*b*-PAA (11/1.2), PS-*b*-PAA (16.4/4.5), and the PS-*b*-PAA (66.5/4.5) systems, respectively. A scaling relationship for the total micellar radius, specific to the regime where micelles have corona segments much longer than core segments, was previously developed by Halperin¹⁹. This scaling relationship shows that the total micellar radius (*R*) scales as $(N_{\text{PAA}})^{4/25} (N_{\text{PS}})^{3/5}$, where N_{PAA} denotes the number of repeat units of the PAA segment, and N_{PS} denotes the number of repeat units of the PS segment. Our hydrodynamic radius data from DLS agree very closely with this scaling law. However, this theory also predicts that the aggregation number and the core radius of the micelles should be independent of the PS segment length in this regime, whereas we observed a decrease in the size of the core radius with increasing the PS segment length at constant PAA segment length.

Although the areal density of the PAA domains can be tailored by variation of the molecular weight (as shown in Figure 3-5), there is an unavoidable coupling of areal density with the size of the nanoclusters. Therefore, a more general approach allowing independent control of these two parameters was sought. By adding PS homopolymer ($M_n(\text{PS}) = 8\,500\text{ g/mol}$) to our micellar solution, as illustrated in route iii) of Figure 3-1, we were able to vary the areal density over an order of magnitude, as demonstrated in the TEM images in Figure 3-6. In all three TEM images in Figure 3-6, the PS-*b*-PAA (16.4/4.5) copolymer was used and the FeCl₃ loading ratio was constant at 5.4. In Figure 3-6a, no PS homopolymer was added to the solution, and a density of 6×10^{10} particles per cm² was achieved. In Figure 3-6b, PS homopolymer was added to the micellar

solution at a ratio of 4 molecules of PS homopolymer per molecule of PS-*b*-PAA block copolymer ([PS : PS-*b*-PAA] = 4). This addition of PS homopolymer decreased the areal density by 83% to 1.1×10^{10} particles per cm^2 . By further increasing the PS homopolymer to block copolymer ratio ([PS : PS-*b*-PAA] = 10), as shown in Figure 3-6c, the density decreased to 6.5×10^9 particles per cm^2 . These results, which are summarized in Table 3-3, indicate that the addition of PS homopolymer was a successful methodology for varying the areal density over nearly an order of magnitude. At the same time, there is a clear loss of packing regularity in the resulting nanocluster arrays.



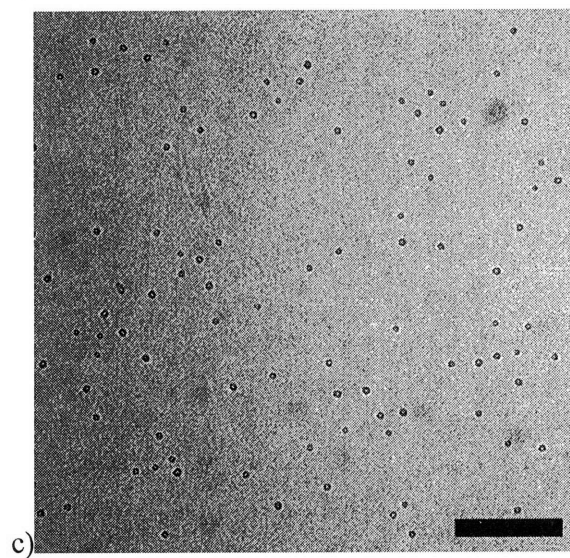


Figure 3-6. TEM images of iron oxide nanocluster arrays synthesized from micellar thin films using PS-*b*-PAA (16.4/4.5) with a FeCl₃ loading ratio of 5.4 and a [PS : PS-*b*-PAA] equal to: (a) 0 (no PS homopolymer); (b) 4; (c) 10. Scale bar = 250 nm.

<u>PS</u>	<u>PAA</u>	<u>Concentration</u> <u>of PS/PAA</u>	<u>Ratio [PS : PS/PAA]</u>	<u>Areal</u> <u>Density</u>
(g/mol)	(g/mol)	(mg/mL toluene)		(part/cm ²)
16 400	4 500	13	No PS homopolymer	6.0E+10
16 400	4 500	5	4	1.1E+10
16 400	4 500	5	10	6.5E+09

Table 3-3. Effects of varying the ratio of PS homopolymer molecules per PS-*b*-PAA molecule ([PS : PS-*b*-PAA]) on the areal density of iron oxide nanocluster arrays synthesized from micellar thin films using PS-*b*-PAA (16.4/4.5) with a FeCl₃ loading ratio of 5.4.

As mentioned in the Experimental section, the addition of PS homopolymer into the micellar solution increased the viscosity of the resulting solutions significantly, and toluene dilutions were employed to facilitate processing. As a control experiment to determine whether or not the dilution itself somehow affected the resulting micellar array spacing, a 5 mg/mL toluene solution of PS-*b*-PAA (16.4/4.5) without PS homopolymer was spin-cast onto a substrate to create a micellar thin film to compare with the 13 mg/mL results shown above in Figure 3-6a. The resulting TEM images (not shown) revealed nanocluster arrays that had diameters and a center-to-center spacing that were identical to the arrays in Figure 3-6a.

Another useful strategy is to combine different micellar solutions, as shown in route iv) from Figure 3-1. This novel procedure can allow for controlling the spatial density of loaded nanoreactors on the substrate or for the synthesis of multiple species metal nanocluster arrays, as described below.

Variations in the areal density of metal-loaded micelles on a substrate were achieved by combining a PbAc₂-loaded micelle solution (loading ratio ~ 5.4) with an unloaded micelle solution in a 1:1 volume ratio for 1 min and then spin casting the solution onto a substrate. The resulting TEM image is shown in Figure 3-7. It is apparent from the TEM image that the areal density of the metal nanoclusters has decreased due to the inclusion of unloaded PAA domains within the micellar thin film. By analyzing the image, we estimated the ratio of metal-loaded micelles to unloaded micelles in the thin film to be roughly 1:1, which is equal to the ratio in our initial mixture. It is interesting to note that when the PbAc₂-loaded micellar solution was combined with the unloaded micellar solution for an extended period of time (1 – 2 days), the thin films lacked

unloaded micelles and contained only Pb-loaded micelles (image not shown). This demonstrates that there is significant diffusion and exchange of the metal species within the micellar solution, and that the holding time following the combination of these micellar solutions is an important factor.

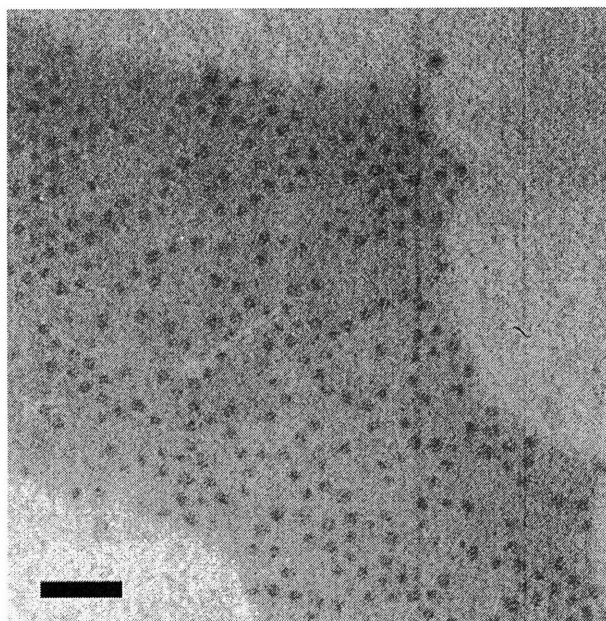
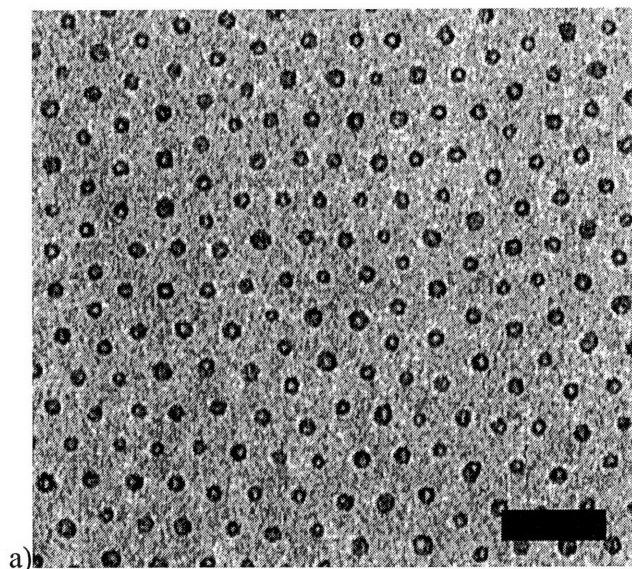


Figure 3-7. TEM image of Pb-containing nanocluster array formed from combining a PbAc₂-loaded micelle solution with an unloaded micelle solution in a 1:1 volume ratio for 1 min and then spin casting onto a substrate. Scale bar = 100 nm.

The procedure for combining different micellar solutions can also be used to create nanoclusters arrays consisting of more than one inorganic species. To characterize the nanocluster arrays with multiple metal species, we used STEM equipped with EDX analysis, which identifies elements through the detection of the characteristic energies of x-rays that are emitted from a specific atomic species when bombarded by the electron beam. The results from a typical analysis of a nanocluster array are shown below in

Figure 3-8. Using these techniques, we are able to capture an annular dark field image of the nanoclusters (shown in Figure 3-8b), and then create corresponding elemental maps for specific elements, shown for the case of Fe in Figure 3-8c. Comparing Figures 3-8b and 3-8c, it is clear for this sample that each nanocluster contains Fe molecules. We also acquire EDX spectra for single nanoclusters by focusing the beam on each nanocluster individually, as shown in Figure 3-8d. This allows us to determine the composition of individual nanoclusters in a more quantitative manner. It should be noted that the large Si and N peaks seen in Figure 3-8d are expected and due to our use of Si_3N_4 as the substrate; an O peak is not observed because it is located within the large N peak. For each of the nanocluster arrays discussed below, an analysis similar to the example shown in Figure 3-8 was performed.



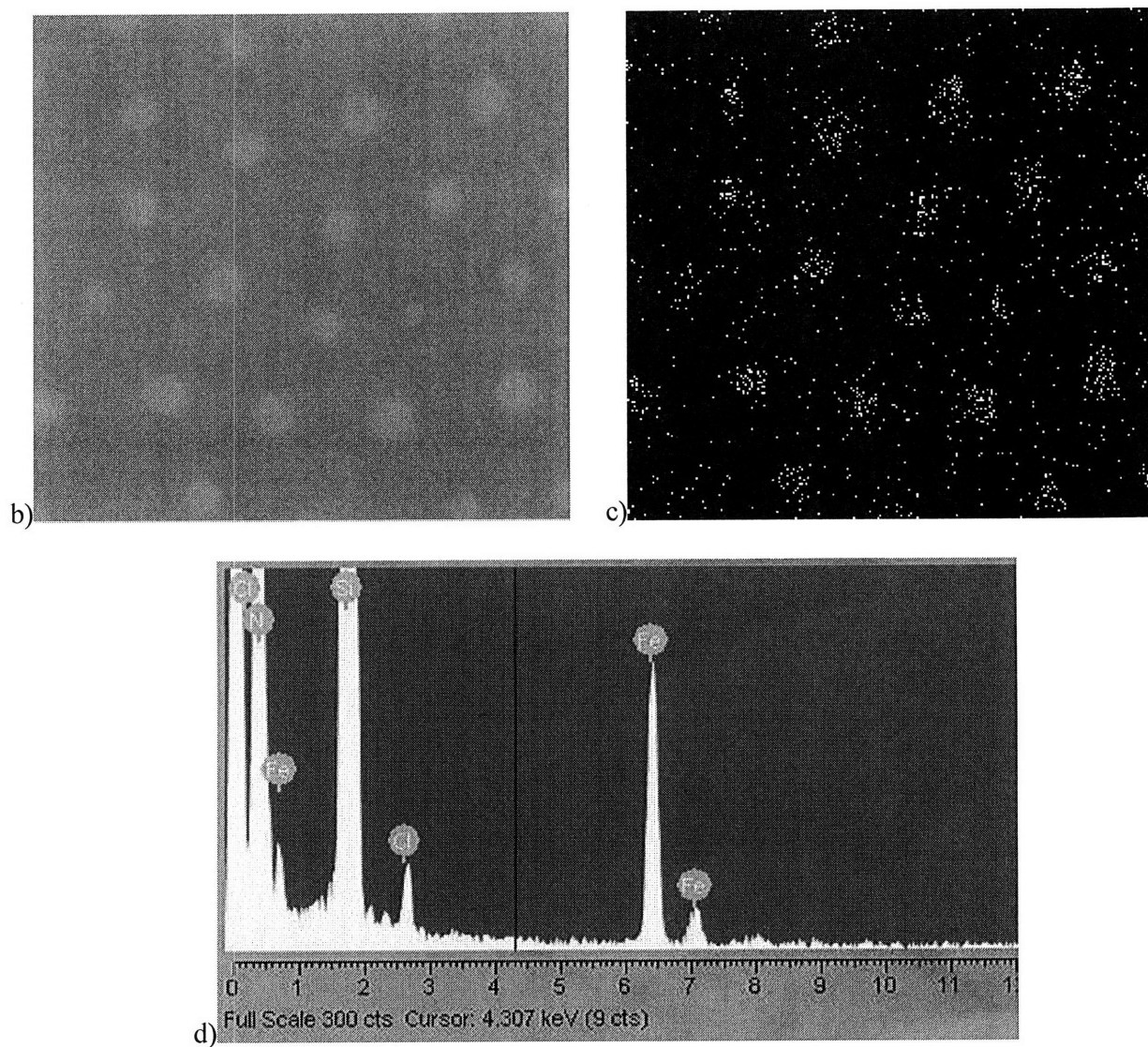
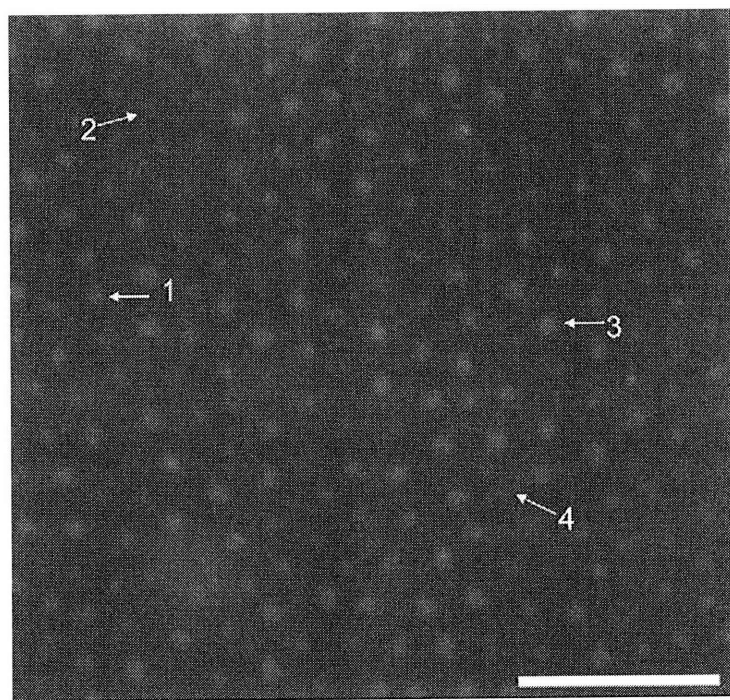


Figure 3-8. Characterization of a nanocluster array formed from PS-*b*-PAA (16.4/4.5) copolymer with a FeCl₃ loading ratio of 5.4: a) Bright field TEM image (scale bar ~ 100 nm); b) Annular dark field image obtained using STEM; c) Elemental Fe map obtained using EDX analysis with STEM; d) EDX spectra from nanocluster obtained using STEM.

As mentioned above in the context of combining PbAc₂-loaded micellar solutions and unloaded micellar solutions, the contact time before spin-casting is a critical factor.

To study this effect in more detail, we created a mixed micellar solution from a FeCl_3 -loaded micellar solution (loading ratio ~ 0.3) and a PbAc_2 -loaded micellar solution (loading ratio ~ 0.9) in a 1:1 volume ratio. Two nanocluster arrays were then created from this combined solution; one was spin-cast 2 min after the solutions were combined and the other 120 hr after combination. The annular dark field image obtained from the 2 min sample is shown in Figure 3-9. By analyzing the elemental maps and the EDX spectra for each nanocluster (shown in Figure 3-9), it is evident that the nanoclusters with the higher contrast are Pb-containing nanoclusters, and that the nanoclusters with lower contrast are Fe-containing nanoclusters. By examining the EDX spectra, it is also clear that each of the nanoclusters contain only one metal species; there has been no noticeable inter-diffusion of metal species between micelles. In this image, 45% of the nanoclusters are iron-containing, corresponding closely to the expected value of 50% for a 1:1 volume ratio.



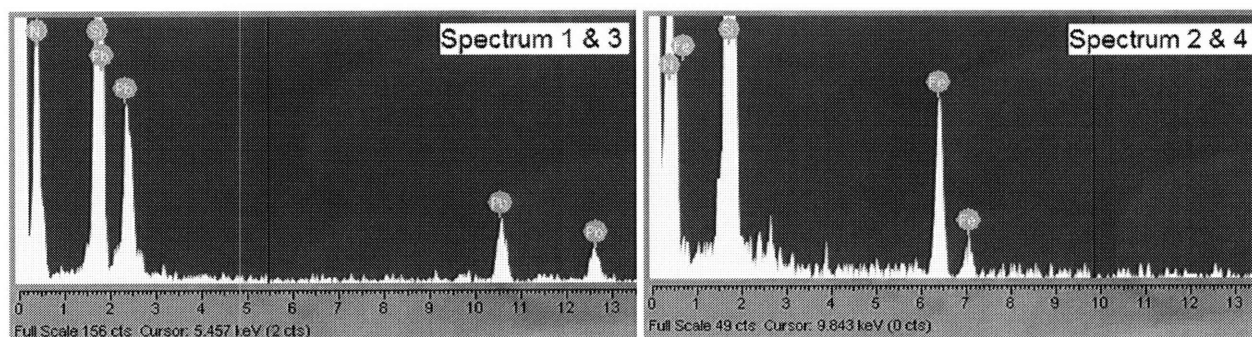


Figure 3-9. Annular dark field image of multi-species nanocluster array formed by combining an FeCl_3 -loaded micellar solution (loading ratio ~ 0.3) with a PbAc_2 -loaded micellar solution (loading ratio ~ 0.9) for 2 min, along with spectrums from EDX analysis. The spectrum on the left was acquired while focusing the electron beam on the nanoclusters labeled 1 & 3 in the dark field image. The spectrum on the right was acquired while focusing the electron beam on the nanoclusters labeled 2 & 4 in the dark field image. Scale bar = 100 nm.

The resulting annular dark field image from the nanocluster array that was spin-cast 120 hr after the solutions were combined is shown in Figure 3-10. The elemental maps as well as the EDX spectra (shown in Figure 3-10), reveal some nanoclusters whose compositions are nearly all one species (Fe or Pb), in addition to nanoclusters that contain both iron and lead. Figure 3-11 compares the nanocluster populations obtained from the 2 min and 120 hr samples. Increasing the contact times for the combined micelle solutions facilitates considerable inter-diffusion of Fe^{3+} and Pb^{2+} ions, resulting in nanoclusters containing multiple metal species.

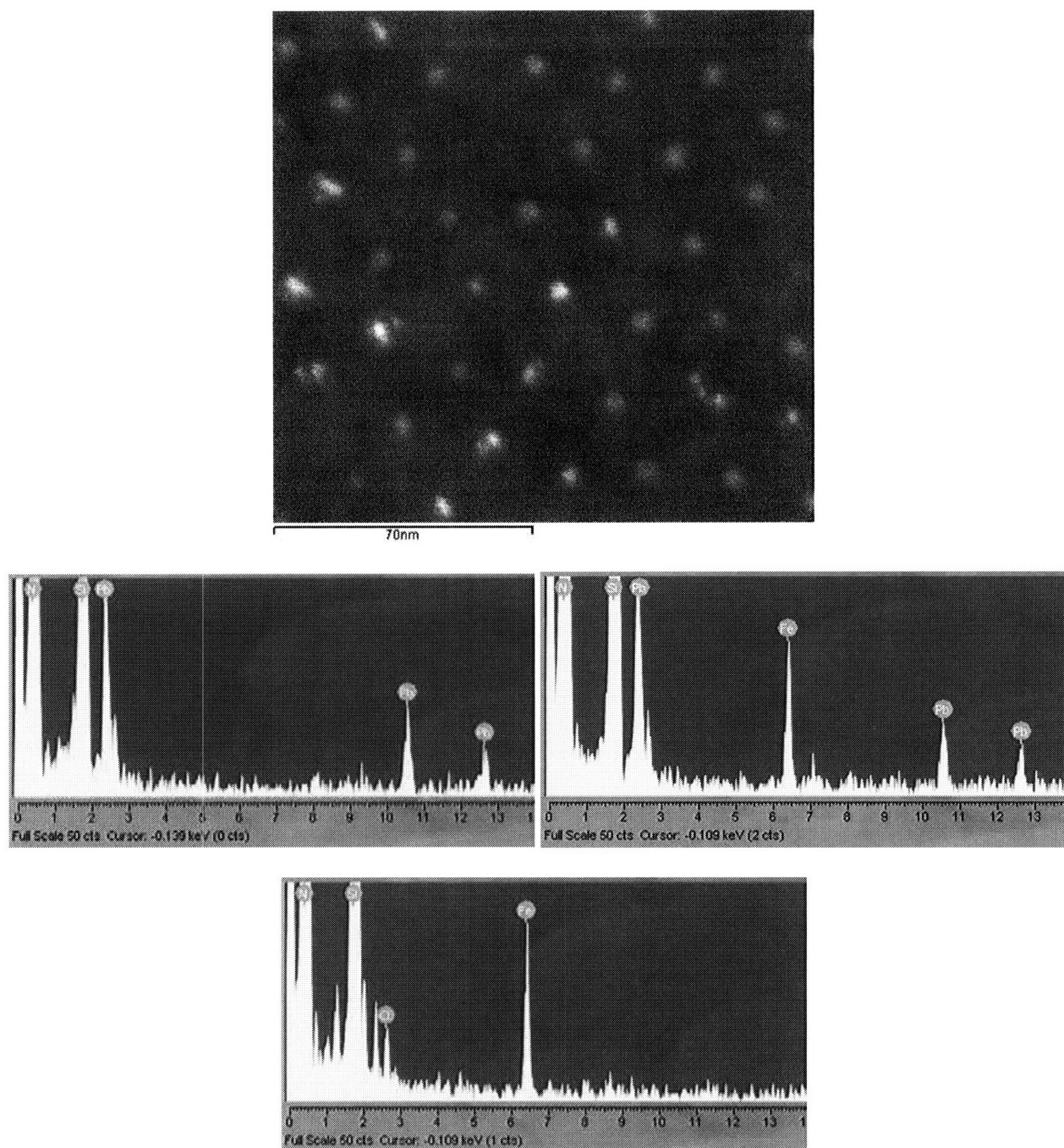


Figure 3-10. Annular dark field image of multi-species nanocluster array formed by combining an FeCl_3 -loaded micellar solution (loading ratio ~ 0.3) with a PbAc_2 -loaded

micellar solution (loading ratio ~ 0.9) for 120 hr, along with EDX spectrums from individual nanoclusters.

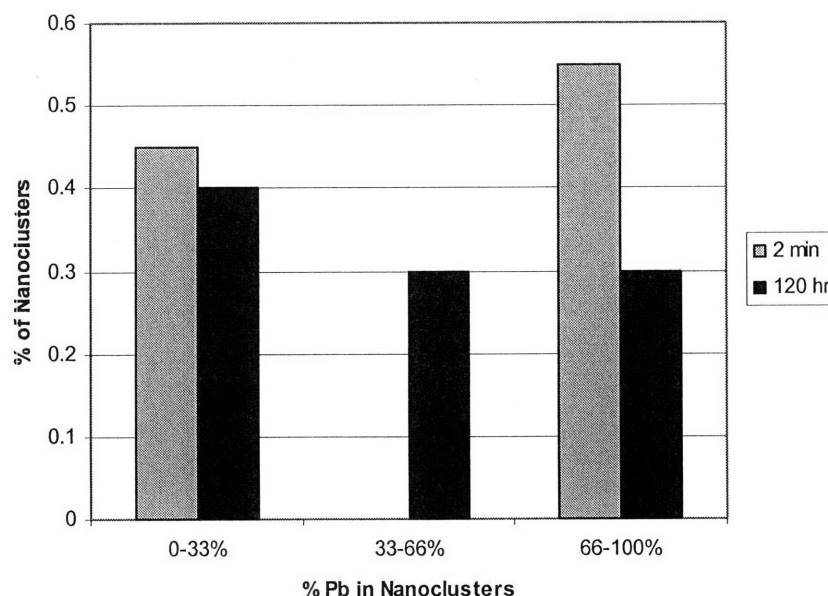


Figure 3-11. Comparison of the composition of multi-species nanocluster arrays formed by combining an FeCl_3 -loaded micellar solution (loading ratio ~ 0.3) with a PbAc_2 -loaded micellar solution (loading ratio ~ 0.9) for 2 min vs. 120 hr before spin-casting.

The compositions of these nanocluster arrays can also be controlled by varying the volume ratio of the combined micellar solutions. In this case, we created three separate mixed micellar solutions where an FeCl_3 -loaded micellar solution (loading ratio ~ 0.3) was combined with a PbAc_2 -loaded micellar solution (loading ratio ~ 0.9) in volume ratios of 1:9, 1:1, and 9:1, where the volume ratio is defined as the mL of FeCl_3 -loaded micelle solution per mL of PbAc_2 -loaded micelle solution. The solutions were then spin-cast onto a substrate 120 hr after they were created. After analyzing each substrate using EDX analysis, we can compare the composition of nanoclusters as a

function of the initial volume ratio of the combined micellar solution, as shown in Figure 3-12. Variation of the volume ratio of the combined micelle solutions has a significant effect on the nanocluster composition distribution. When the volume ratio was 1:1, we observed approximately an equal percentage of Fe-containing, Pb-containing nanoclusters, and Fe- and Pb-containing nanoclusters. When the volume ratio was changed to 9:1, we observed that nearly all of the nanoclusters were Fe-containing. When the volume ratio was 1:9, we observed approximately 5% of the nanoclusters were Fe-containing, 40% of the nanoclusters were Pb-containing, and 55% of the nanoclusters contained both Fe and Pb. We believe this observation is a result of the higher solubility of FeCl_3 in toluene compared to PbAc_2 , which allows for higher loadings of the FeCl_3 -loaded micelles compared to the PbAc_2 -loaded micelles. When the micelle solutions are combined, the increased loading of the Fe-containing micelles facilitates increased exchange of the Fe^{3+} ions into Pb-loaded micelles. This results in an increased percentage of nanoclusters containing both Fe and Pb and a decreased percentage of Pb-containing micelles, as seen in the data in Figure 3-12.

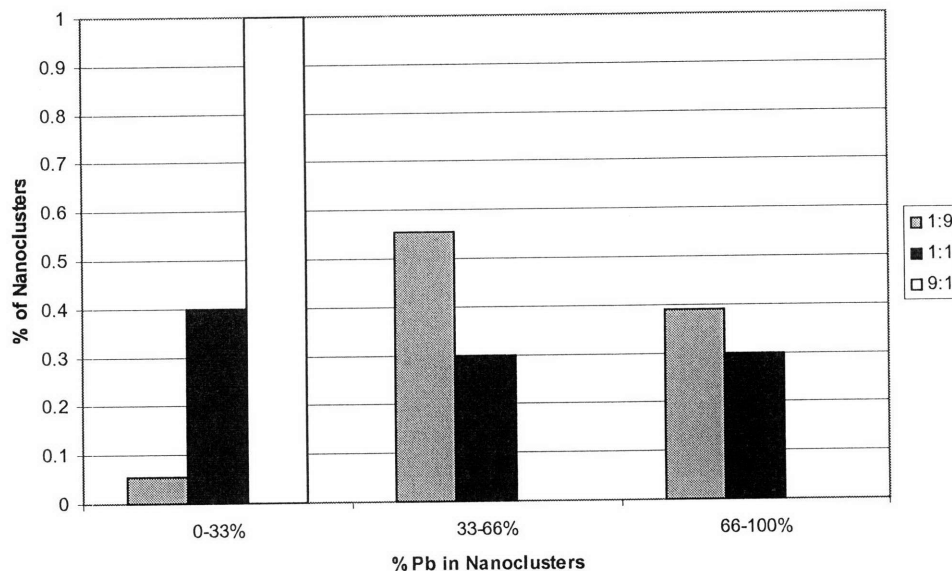


Figure 3-12. Comparison of the composition of multi-species nanocluster arrays formed by combining an FeCl_3 -loaded micellar solution (loading ratio ~ 0.3) with a PbAc_2 -loaded micellar solution (loading ratio ~ 0.9) in a volume ratio of 1:9, 1:1, and 9:1, where the ratio is mL of FeCl_3 -loaded micelle solution per mL of PbAc_2 -loaded micelle solution. The solutions were spin-cast onto a substrate 120 hr after they were created.

To help understand the inter-diffusion issues of these inorganic species, we used a two-step loading process to create inorganic nanocluster arrays. In this system, we created PbAc_2 -loaded micelles (loading ratio ~ 0.9) using the $\text{PS-}b\text{-PAA}$ (16.4/4.5) copolymer, and after allowing sufficient time for the Pb^{2+} ions to load, we added FeCl_3 (loading ratio ~ 2.1) directly into the micelle solution. After waiting 24 hr, the solution was spin-cast onto a substrate to create a nanocluster array, which was characterized using EDX analysis and is shown in Figure 3-13. The EDX analysis showed that all of the nanoclusters contained only Fe, indicating that Fe^{3+} ions have a higher affinity for the carboxylic acid groups than Pb^{2+} ions in this system.

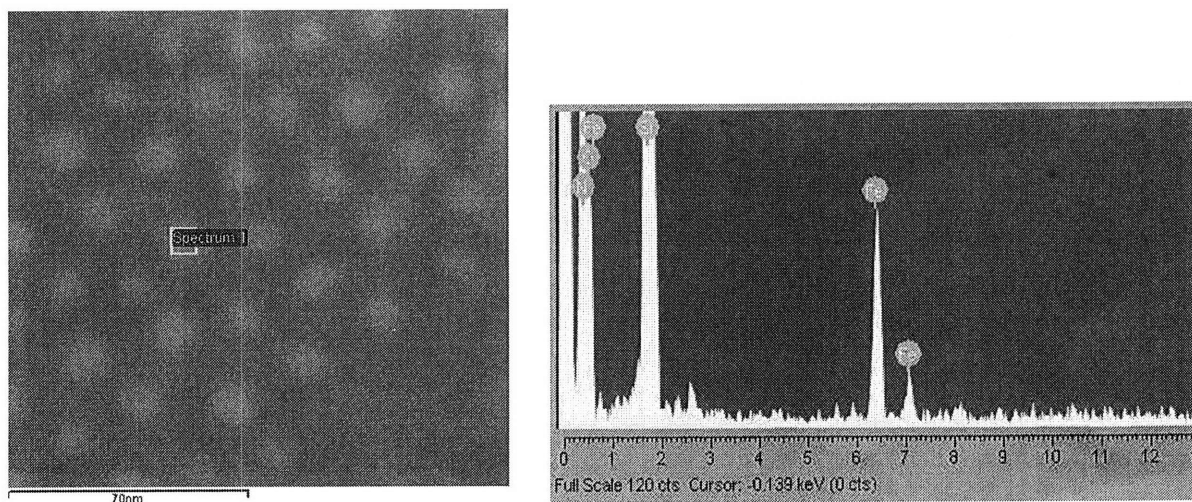


Figure 3-13. Annular dark field image (scale bar = 70 nm) of multi-species nanocluster array formed by adding FeCl_3 (loading ratio ~ 2.1) directly into a previously PbAc_2 -loaded micellar solution (loading ratio ~ 0.9), along with EDX spectrums from individual nanoclusters.

3.4 Conclusion

We have demonstrated the ability to vary the size, center-to-center spacing, and density of spin-cast 2-D arrays of spherical $\text{PS-}b\text{-PAA}$ micelles and the subsequent inorganic nanoclusters synthesized therein. The strategies used to vary the arrays include alteration of the block copolymer molecular weight, addition of PS homopolymer, variation of the metal loading ratio in solution, and the combination of different micellar solutions. We have also demonstrated routes for the creation of metal nanocluster arrays containing multiple metal species, in which each nanocluster contains one or more of the metal species, depending on the synthesis conditions. These routes are based on the inter-diffusion and exchange of different inorganic species within micellar solutions. The

strategies discussed in this work could have useful applications in the synthesis of carbon nanotube catalysts and in the construction of nanopatterned substrates for the investigation of cell attachment and function.

3.5 References

1. Whitesides, G. M.; Mathias, J. P.; Seto, C. T. *Science* **1991**, *254*, 1312-1319.
2. Hamley, I. W. *Nanotechnology* **2003**, *14*, R39-R54.
3. Park, M.; Harrison, C.; Chaikin, P. M.; Register, R. A.; Adamson, D. H. *Science* **1997**, *276*, 1401-1404.
4. Thurn-Albrecht, T.; Schotter, J.; Kastle, C. A.; Emley, N.; Shibauchi, T.; Krusin-Elbaum, L.; Guarini, K.; Black, C. T.; Tuominen, M. T.; Russell, T. P. *Science* **2000**, *290*, 2126-2129.
5. Li, R. R.; Dapkus, P. D.; Thompson, M. E.; Jeong, W. G.; Harrison, C.; Chaikin, P. M.; Register, R. A.; Adamson, D. H. *Applied Physics Letters* **2000**, *76*, 1689-1691.
6. Black, C. T.; Guarini, K. W.; Milkove, K. R.; Baker, S. M.; Russell, T. P.; Tuominen, M. T. *Applied Physics Letters* **2001**, *79*, 409-411.
7. Park, M.; Chaikin, P. M.; Register, R. A.; Adamson, D. H. *Applied Physics Letters* **2001**, *79*, 257-259.
8. Cheng, J. Y.; Ross, C. A.; Thomas, E. L.; Smith, H. I.; Vancso, G. J. *Applied Physics Letters* **2002**, *81*, 3657-3659.
9. Lazzari, M.; Lopez-Quintela, M. A. *Advanced Materials* **2003**, *15*, 1583-1594.
10. Bates, F. S.; Fredrickson, G. H. *Annual Review of Physical Chemistry* **1990**, *41*, 525-557.
11. Spatz, J. P.; Herzog, T.; Mossmer, S.; Ziemann, P.; Moller, M. *Advanced Materials* **1999**, *11*, 149-153.
12. Haupt, M.; Ladenburger, A.; Sauer, R.; Thonke, K.; Glass, R.; Roos, W.; Spatz, J. P.; Rauscher, H.; Riethmuller, S.; Moller, M. *Journal of Applied Physics* **2003**, *93*, 6252-6257.

13. Spatz, J. P.; Mossmer, S.; Hartmann, C.; Moller, M.; Herzog, T.; Krieger, M.; Boyen, H. G.; Ziemann, P.; Kabius, B. *Langmuir* **2000**, *16*, 407-415.
14. Fu, Q.; Huang, S. M.; Liu, J. *Journal of Physical Chemistry B* **2004**, *108*, 6124-6129.
15. Boontongkong, Y.; Cohen, R. E. *Macromolecules* **2002**, *35*, 3647-3652.
16. Bennett, R. D.; Xiong, G. Y.; Ren, Z. F.; Cohen, R. E. *Chemistry of Materials* **2004**, *16*, 5589-5595.
17. Data retrieved from NIST X-ray Photoelectron Spectroscopy Database: Version 2.0, located at <<http://nist.gov/srd/nist20.htm>>.
18. Khougaz, K.; Zhong, X. F.; Eisenberg, A. *Macromolecules* **1996**, *29*, 3937-3949.
19. Halperin, A. *Macromolecules* **1987**, *20*, 2943-2946.

Chapter 4 Controlling the Morphology of Carbon Nanotube Films by Varying the Areal Density of Catalyst Nanoclusters Using Block Copolymer Micellar Thin Films*

4.1 Introduction

In spite of much research progress in the science and synthesis of carbon nanotubes (CNTs)¹, control over the location and orientation of CNTs on substrates remains a major challenge. A key breakthrough was the synthesis of vertically-aligned CNT (VA-CNT) arrays using thermal chemical vapor deposition (CVD)²⁻⁷ and plasma-enhanced CVD⁸, where the CNTs self-orient perpendicular to the substrate surface due to initial crowding and continue to grow upward in this direction. These CNT arrays have wide-ranging applications including membranes, heat dissipation, electrical interconnects, and nanoelectronics⁹⁻¹³. The catalysts for synthesis of vertically-aligned CNTs are commonly prepared by sputtering or evaporating a thin metal film onto a substrate^{14,15}, which dewets to form catalyst nanoparticles at an elevated temperature prior to growth¹⁶⁻¹⁸. While these catalysts are easily prepared and patterned by shadow masking or lithography^{7,14}, these approaches are not easily able to create nanocluster catalysts having monodisperse diameters and quantifiable areal densities. In thin metal films, both the nanocluster size and areal density are coupled to the film thickness, and the annealing procedure affects the size, density, and the chemical state of the

nanoclusters. Recently Huh *et al*¹⁹ demonstrated a route for controlling the density of CNT growth using varying densities of colloidal cobalt nanoparticles; however, due to nanoparticle coalescence their route does not enable precise quantification of nanocluster areal density and leads to a broad distribution of CNT diameters. Zhang *et al*²⁰ also recently demonstrated the control of CNT growth by varying the density of Co-Mo nanoparticles, although their route is unable to independently vary the diameter and the areal density of nanoparticles.

We employ a methodology for synthesizing iron oxide nanoclusters that utilizes micelles formed by the amphiphilic block copolymer, poly(styrene-*b*-acrylic acid) (PS-*b*-PAA)^{21,22}. This catalyst system has significant value because it enables the creation of nanocluster arrays of a chosen metal species, with independent control of the nanocluster diameter and areal density²². In previous chapters, nanocluster diameters were varied between 5 nm and 16 nm and the areal density was varied from $6.0 \times 10^{10} \text{ cm}^{-2}$ to $1 \times 10^9 \text{ cm}^{-2}$, although variation outside of these ranges is easily accessible. At higher areal densities, the nanoclusters are hexagonally ordered. Further, as we will present in the subsequent chapter, the nanoclusters arrays can be patterned on the micron length scale using microcontact printing²³.

In this chapter we utilize this system to create arrays of uniform-diameter iron oxide nanoclusters, having quantifiable areal densities that can be varied over more than an order of magnitude. We achieve vertical CNT growth from our catalyst system through appropriate selection of the substrate, catalyst preparation procedure, and reaction conditions. To the best of our knowledge, our work is the first example of vertical growth of CNTs from a block copolymer based catalyst. Because this catalyst

system allows for precise quantification of the nanocluster areal density, we can estimate the percentage of nanoclusters that nucleate the growth of a CNT. By uniformly varying the areal density of iron oxide nanoclusters on the substrate surface, we manipulate the morphology of the CNT film from a tangled and sparse arrangement of individual CNTs, through a transition region with locally bunched and self-aligned CNTs, to rapid growth of thick vertical CNT films.

4.2 Experimental Section

4.2.1 Materials

Poly(styrene-*block*-acrylic acid) (PS-*b*-PAA) [M_n (PS) = 16 400 g/mol, M_n (PAA) = 4 500 g/mol, PDI = 1.05] and polystyrene (PS) homopolymer (M_n = 8500 g/mol, PDI = 1.06) were used as received from Polymer Source, Inc. The following chemicals were also used as received: anhydrous iron(III) chloride (FeCl_3) obtained from Sigma-Aldrich Co., and toluene (HPLC grade, 99.8%) obtained from Sigma-Aldrich Co. The substrates were clean silicon wafers (p-type, Silicon Quest International) coated with a 1 μm layer of thermally-grown SiO_2 , or a 15 nm layer of Al_2O_3 deposited by electron beam evaporation in Temescal VES-2550 with a FDC-8000 Film Deposition Controller. The silicon nitride membrane window substrates were purchased from Structure Probe, Inc. Each substrate (surface area $\sim 4.5 \text{ mm}^2$) consisted of a 100-nm-thick amorphous, low-stress Si_3N_4 membrane supported on a 0.2-mm-thick silicon wafer that had been back-etched in the center to create the electron transparent Si_3N_4 window (surface area $\sim 0.2 \text{ mm}^2$). The use of the electron-transparent silicon nitride substrates allows for direct TEM characterization without disturbing the spin-cast films.

4.2.2 Preparation of Carbon Nanotube Growth Catalysts

Details about synthesizing iron oxide nanocluster arrays have been discussed in previous chapters^{21,22,24}. In brief, PS-*b*-PAA was mixed with toluene at a concentration of 10 mg/mL and heated to 145 °C for 20 min in a sealed vial to create a spherical block copolymer micellar solution. The PAA micelle cores were selectively loaded with iron by adding FeCl₃ to the micellar solution at a ratio of 5.4 metal ion equivalents per carboxylic acid group. Thin films were then created by spin casting the metal-loaded micellar solutions onto the planar substrates at 2000 – 8000 rpm for 1 min at room temperature. The micellar thin film was removed by oxygen plasma etching (rf plasma, 8 – 12 MHz) for 20 min, leaving only the inorganic iron oxide nanocluster arrays remaining on the substrate. To create iron oxide nanocluster arrays with lower areal densities, PS homopolymer ($M_n = 8500$ g/mol) was added to the micellar solutions with a PS-*b*-PAA to PS homopolymer ratio of 3:1, 4:1, and 50:1 prior to spin casting. To reduce the viscosities of these solutions to acceptable levels for spin casting monolayers, the solutions with a 3:1 and 4:1 ratio were diluted with toluene from 10 mg PS-*b*-PAA / mL of toluene to 5 mg PS-*b*-PAA / mL of toluene, while the solution with a 50:1 ratio was diluted to 1 mg PS-*b*-PAA / mL of toluene.

4.2.3 Carbon Nanotube Growth Procedure

CNT growth is performed in a single-zone atmospheric pressure quartz tube furnace (Lindberg), having an inside diameter of 22 mm and a 30 cm long heating zone, using flows of Ar (99.999%, Airgas), C₂H₄ (99.5%, Airgas), and H₂ (99.999%, BOC). The substrate sample is rested in the furnace tube, at a location starting 40 mm

downstream of the control thermocouple. The furnace temperature is ramped to the set point temperature in 30 minutes and held for an additional 15 minutes under 400 sccm Ar. The flows of Ar and H₂ used during growth are established 1 minute prior to introducing C₂H₄, and then the C₂H₄/H₂/Ar mixture is maintained for the growth period of 15 – 60 minutes. Finally, the H₂ and C₂H₄ flows are discontinued, and 400 sccm Ar is maintained for 10 more minutes to displace the reactant gases from the tube, before being reduced to a trickle while the furnace cools to below 100 °C.

4.2.4 Characterization

Transmission electron microscopy (TEM) was performed on a JEOL 2000FX operating at 200 kV. Scanning electron microscopy (SEM) was performed on a JEOL 6320FV field-emission high-resolution microscope operating at 5 kV. High-resolution TEM (HRTEM) was performed on a JEOL 2010 operating at 200 kV. Thermogravimetric analysis (TGA) was performed on a Perkin Elmer TGA7 Thermogravimetric Analyzer. Spectroscopic ellipsometry was performed using an ellipsometer (model M-2000D) manufactured by J. A. Woollam Co. Atomic force microscopy (AFM) was performed on a Digital Instruments Dimension 3000 NanoScope IIIA scanning probe microscope operating in tapping mode using a silicon cantilever. The images were analyzed using NanoScope III software (version 5.12r3, Digital Instruments).

4.3 Results and Discussion

The procedure for synthesizing the iron oxide nanocluster arrays utilized spherical micelles formed by PS-*b*-PAA in toluene, which were loaded with FeCl₃, and then spin-cast onto a substrate^{21,22,24}. The polymer thin film was then treated in oxygen plasma to remove the organic components, leaving an iron oxide nanocluster array as shown in Figure 4-1. Previous studies have demonstrated that the iron oxide nanocluster structure is Fe₂O₃^{22,25}. The molecular weight and metal loading ratios of Figure 4-1 led to iron oxide nanocluster arrays with diameters of 16 ± 1.6 nm, that were arranged in a quasi-hexagonal array with an areal density of $6.0 \times 10^{10} \text{ cm}^{-2}$ ²². The root-mean-square (rms) roughness of the nanocluster arrays was 2.2 nm, as determined from atomic force microscopy (AFM).

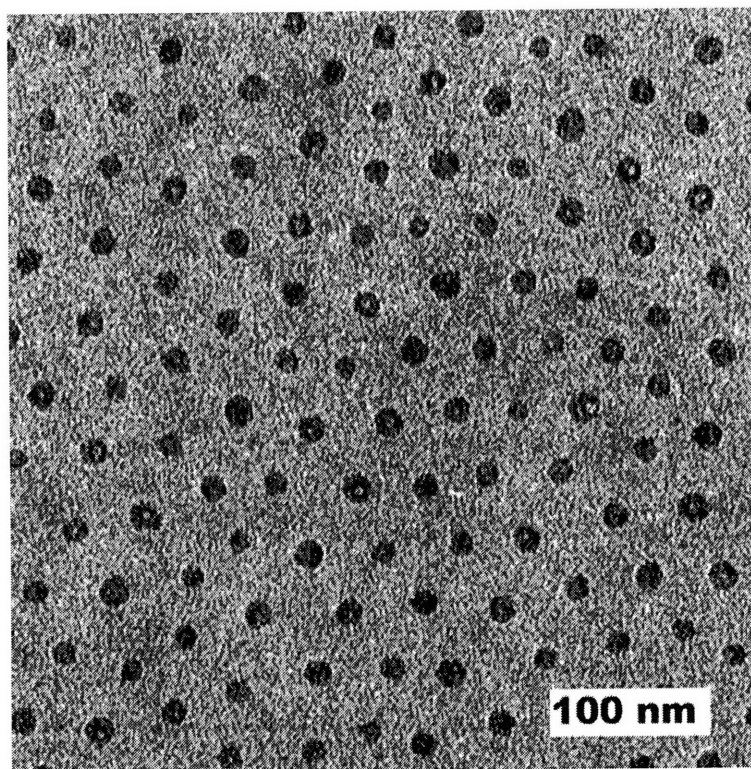


Figure 4-1. TEM image of iron oxide nanoclusters on a Si₃N₄ window grid prior to CNT growth.

We first synthesized CNTs using our iron oxide nanocluster catalyst on a SiO₂ substrate, via a CVD process with 100/500/200 sccm of C₂H₄/H₂/Ar at 750 °C⁷. The resulting CNTs were short (generally 1 μm in length), tangled and sparsely-distributed on the substrate. To improve the CNT yield, we synthesized iron oxide nanoclusters on a Si substrate coated with Al₂O₃ deposited by electron beam evaporation. Figure 4-2 shows the growth results for the nanoclusters on an Al₂O₃-coated Si wafer using identical growth conditions as used for the SiO₂-supported nanoclusters. The Al₂O₃ support improved the activity of our iron-based catalyst and increased the CNT growth density, in agreement with previous reports studying the effect of Al₂O₃-coated substrates on CNT growth^{15,26}. The inset of Figure 4-2 clearly demonstrates that the iron oxide nanoclusters on Al₂O₃-coated Si do not migrate and coalesce at the high growth temperature. To further improve the CNT yield, the gas flow rates for the CNT growth were systematically varied. Figure 4-3 shows the effect of doubling the C₂H₄ flow rate while keeping the Ar and H₂ flow rates constant (C₂H₄/H₂/Ar flow rates of 200/500/200 sccm at 750°C). The increased carbon supply significantly increased the CNT yield, causing sporadic regions of CNTs to grow vertically from the substrate surface. Results similar to Figure 4-3 were also observed using 200/500/0 sccm C₂H₄/H₂/Ar at 750°C.

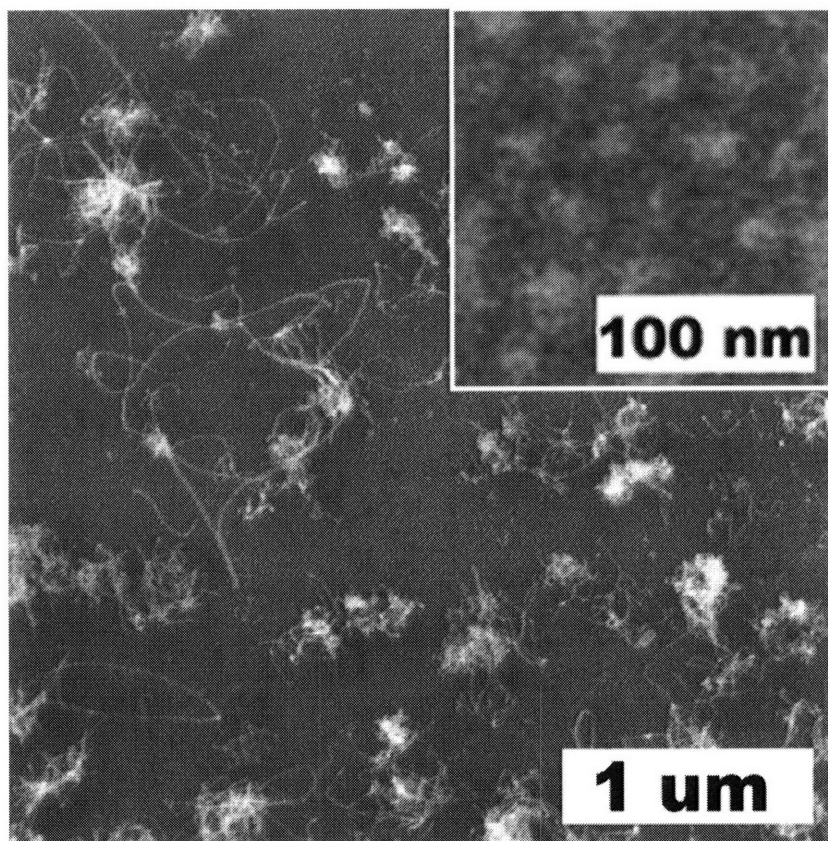


Figure 4-2. SEM image of a CNT growth using 16 nm diameter iron oxide nanoclusters on Al_2O_3 -coated Si with a flow rate of 100/500/200 sccm of $\text{C}_2\text{H}_4/\text{H}_2/\text{Ar}$ at 750°C , where the inset shows a higher resolution SEM image demonstrating that the iron oxide nanoclusters do not coalesce during the growth process.

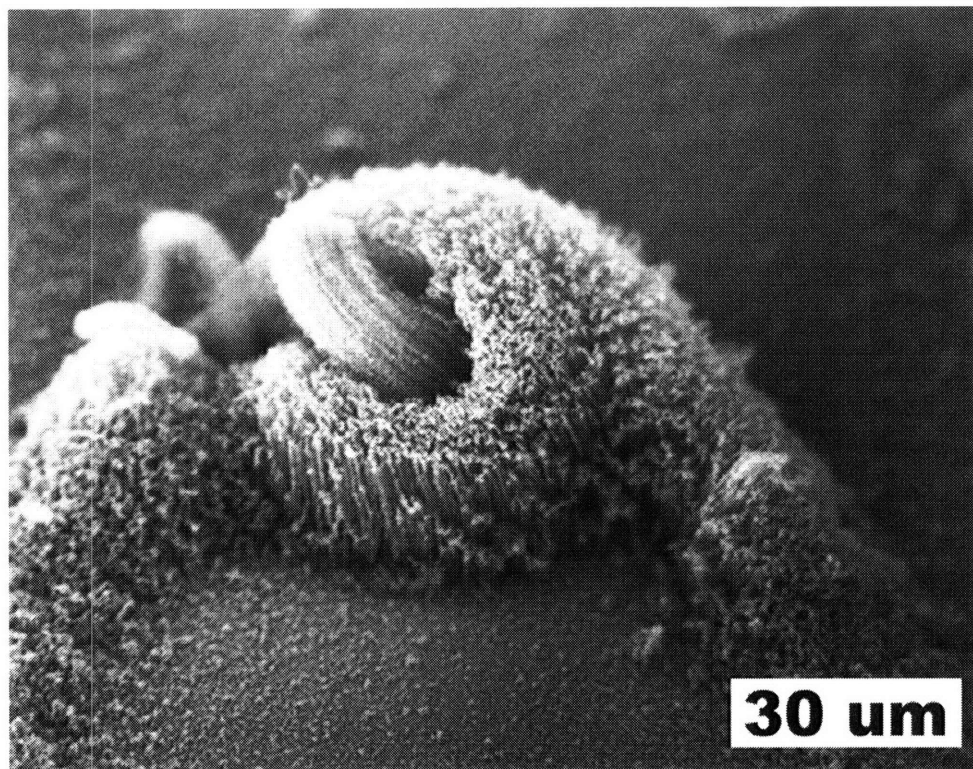


Figure 4-3. SEM image of a CNT growth using 16 nm diameter iron oxide nanoclusters on Al₂O₃-coated Si with a flow rate of 200/500/200 sccm of C₂H₄/H₂/Ar at 750°C (45° tilt).

Because of the flexibility of this catalyst system, we were also able to synthesize iron oxide nanocluster arrays with diameters of 8.0 ± 0.7 nm and an areal density of $8.2 \times 10^{10} \text{ cm}^{-2}$. We observed that the 8 nm diameter iron oxide nanocluster arrays catalyzed significantly fewer CNTs than the 16 nm diameter iron oxide nanoclusters at each of the growth conditions shown in Figures 4-2 and 4-3, and vertical CNT growth from the 8 nm diameter nanoclusters was not observed. Thus, for a given CVD growth condition, nanocluster diameter has a direct effect on the density and the uniformity of the resulting CNT growth. The increased activity of the 16 nm diameter nanoclusters (producing

CNTs with 12 ± 2 nm o.d., discussed later) versus the 8 nm diameter nanoclusters reinforces the notion of a catalyst particle “size window” for growth at a certain CVD condition²⁷. Our previous study of CNT growth from a thin film catalyst at identical CVD conditions demonstrated growth of 8 nm o.d. CNTs with a much broader diameter distribution. Further characterization would enable assessment of surface and support effects that may govern the precise relationship between nanocluster size and CNT diameter, and determine the suitability of a particle for growth. Because this catalyst system enables the synthesis of iron oxide nanoclusters with diameters smaller than 5 nm, we believe that this approach will also be applicable for growing smaller diameter CNTs such as single-walled CNTs (SWCNTs) and double-walled CNTs (DWCNTs). Future research will involve optimizing CVD growth conditions to facilitate the growth of CNTs having tailored diameters and a specific number of walls, along with controlling the film morphology and packing density as suggested by our results here. For the remainder of this chapter, we focus on MWCNT growth from the 16 nm diameter micellar-templated nanoclusters.

During the spin casting of polymer thin films, non-uniformities at the edge of the substrate lead to polymer films that are thicker at the substrate edge than in the center of the substrate²⁸. Depending on the shape of the substrate and other experimental variables, these non-uniformities can extend substantially from the substrate edge. The substrates from Figures 4-2 and 4-3 were created by spin-casting the micellar solution onto a 1 x 1 cm Al₂O₃-coated Si substrate, followed by oxygen plasma etching prior to CNT growth. While these substrates had a monolayer of iron oxide nanoclusters in the center of the substrate, the edge regions had a substantially higher areal density of nanoclusters as a

result of the spin-casting non-uniformities. For the 1 x 1 cm Al_2O_3 -coated Si substrates, denser CNT growth was always observed along the substrate edges, which was consistent with the higher areal density of nanoclusters at the edges. We have previously observed that the yield is affected by the local areal density of catalyst on the substrate, and that under limiting CVD conditions the reactant supply can be depleted at the edges of the substrate surface⁷; therefore it was important for the micellar-based catalyst system to have a uniform micellar film thickness over the entire substrate surface.

To eliminate the non-uniformities in the thickness of the micellar thin film, the micellar solution was spin cast onto 2.5 x 2.5 cm Al_2O_3 -coated Si substrates. The edges of the substrates were then removed to leave a 1 x 1 cm substrate. This process led to substrates with uniform micellar film thicknesses and to uniform areal densities of iron oxide nanoclusters over the entire substrate. Figure 4-4 shows CNTs grown from a uniform density nanocluster array on Al_2O_3 -coated Si using CVD with 200/500/0 sccm $\text{C}_2\text{H}_4/\text{H}_2/\text{Ar}$ at 750 °C. The activity of the catalyst and the density of the CNT growth substantially increased compared to the CNT growth shown in Figure 4-3. The dense uniform vertical CNT growth, which is caused by the high density of CNTs simultaneously growing from the nanoclusters, was observed over the entire substrate surface.

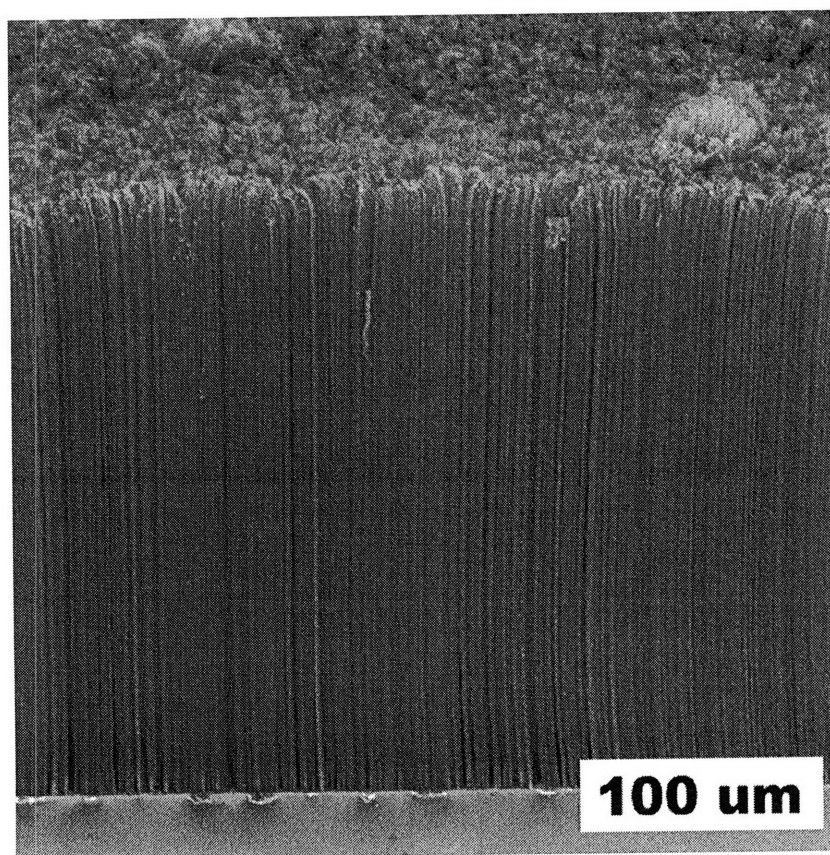
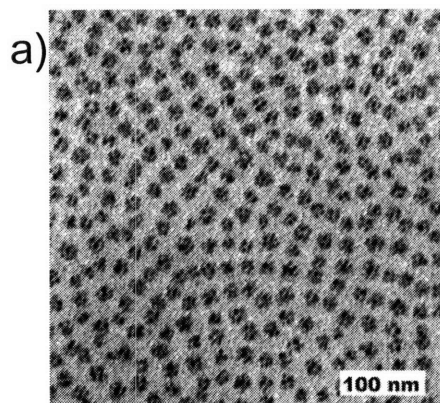


Figure 4-4. SEM image (85° tilt) of vertical CNT growth from 16 nm iron oxide nanocluster arrays created from a micellar monolayer of uniform thickness on Al₂O₃-coated Si after C₂H₄/H₂/Ar flow rates of 200/500/0 sccm at 750°C.

The capability to systematically vary the areal density of iron oxide nanoclusters on the substrate is one of the key advantages of this catalyst system. By adding varying amounts of polystyrene (PS) homopolymer into the PS-*b*-PAA micelle solution prior to spin casting, the areal density of iron oxide nanoclusters can be systematically decreased over more than an order of magnitude²². Because the areal density of the iron oxide nanoclusters can easily be varied and quantified, the morphology of CNT films can be controlled and studied using this catalyst system. The results from our catalyst system are shown in Figure 4-5, which demonstrates the effects of uniformly varying the areal

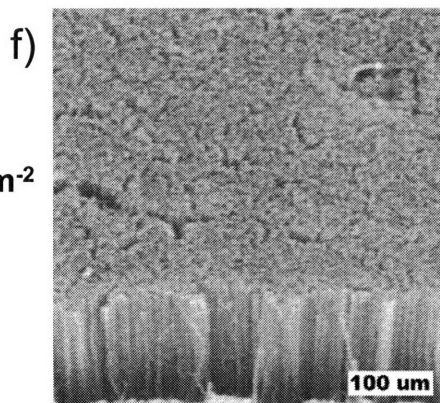
density of the iron oxide nanoclusters on CNT growth. All of the substrates in Figure 4-5 were cut from a larger initial substrate to remove the non-uniform edge regions. In each level of the figure a TEM image of the catalytic nanoclusters is shown on the left, with the corresponding SEM image of the resulting CNT growth on the right. As discussed previously, an iron oxide nanocluster areal density of $6 \times 10^{10} \text{ cm}^{-2}$ results in a dense vertical growth of CNTs (Figures 4-5b and 4-5g). By decreasing the spin-casting speed to 2000 rpm, thicker micellar thin films with multilayers of iron oxide nanoclusters were created. These films had a thickness of 50 nm, as measured by ellipsometry, and resulted in an iron oxide areal density of $1.5 \times 10^{11} \text{ cm}^{-2}$ (Figure 4-5a). The CNT growth using this catalyst (Figure 4-5f) resulted in a uniform and dense film of vertically grown MWCNTs that was similar to the CNT growth from the catalyst with an areal density of $6 \times 10^{10} \text{ cm}^{-2}$ (Figure 4-5g). By decreasing the areal density of nanoclusters to $2.5 \times 10^{10} \text{ cm}^{-2}$ (Figures 4-5c and 4-5h), the uniform vertical growth of CNTs was replaced with a more irregular vertical growth, where the average thickness of the CNT thin film was significantly reduced compared to the thickness in Figure 4-5g. These results suggest that the minimum areal density of iron oxide nanoclusters required to grow uniform and thick CNT films is in the range between $2.5 \times 10^{10} \text{ cm}^{-2}$ and $6.0 \times 10^{10} \text{ cm}^{-2}$ for this system.

TEM Image of Catalyst

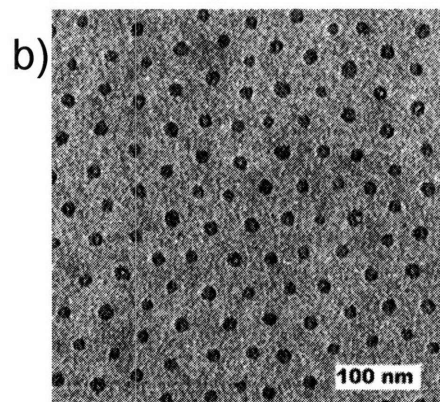


$1.5 \times 10^{11} \text{ cm}^{-2}$

SEM Image of CNTs

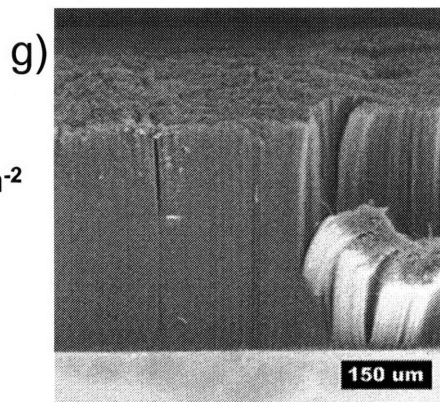


TEM Image of Catalyst

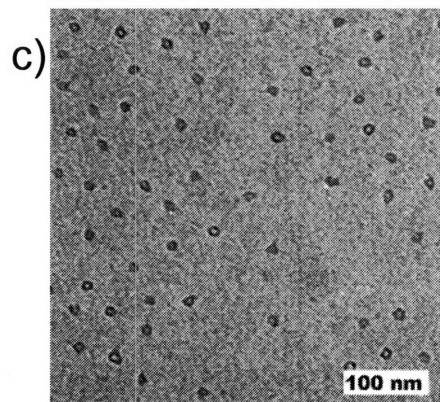


$6 \times 10^{10} \text{ cm}^{-2}$

SEM Image of CNTs

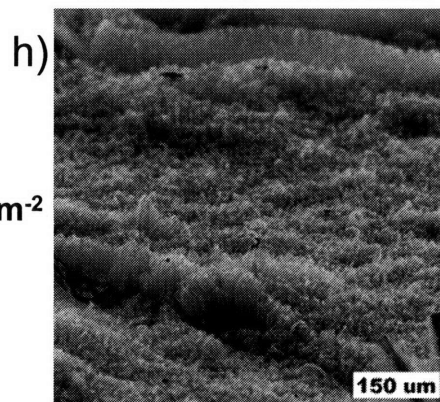


TEM Image of Catalyst



$2.5 \times 10^{10} \text{ cm}^{-2}$

SEM Image of CNTs



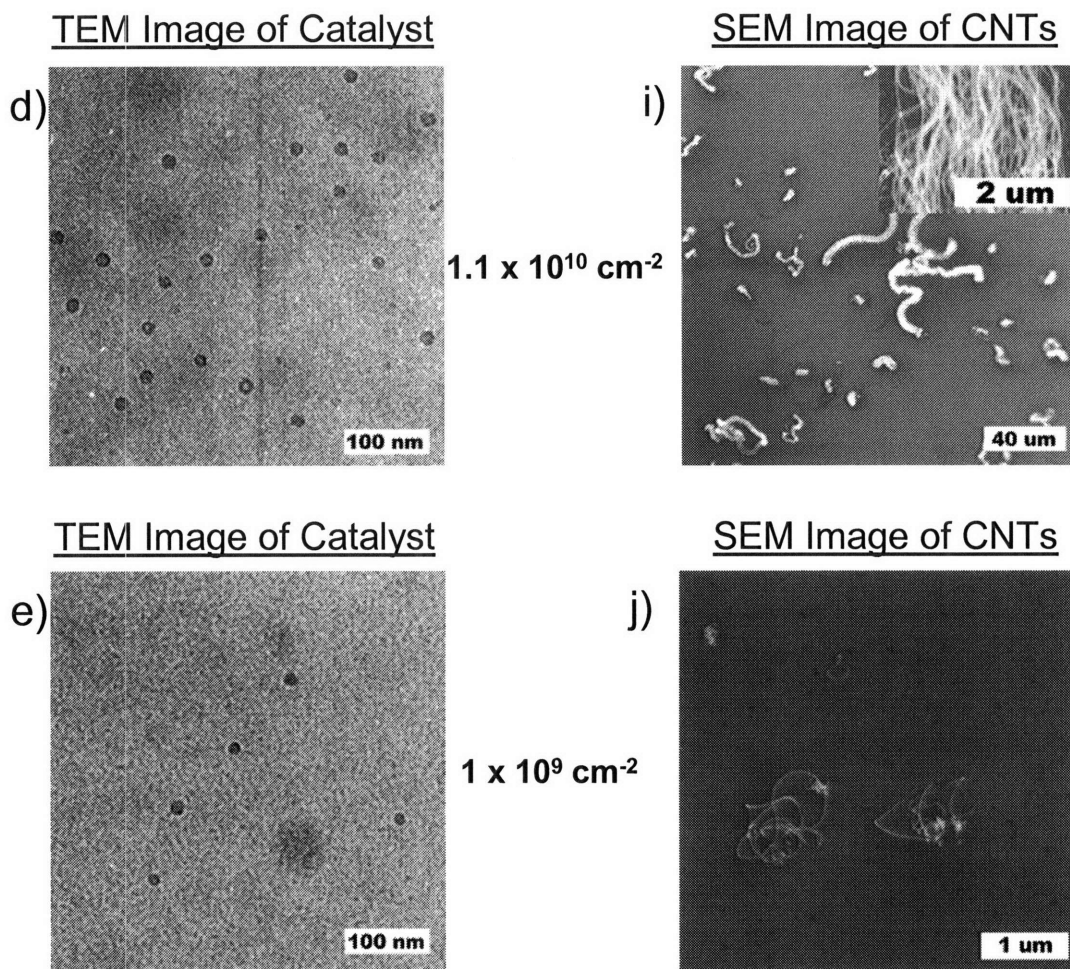


Figure 4-5. Effects of varying iron oxide nanocluster areal density on morphology of CNT films. The left column (a, b, c, d, e) shows TEM images of the iron oxide nanocluster arrays with varying areal density prior to CNT growth. The right column (f - 45° tilt, g - 85° tilt, h - 70° tilt, i - 0° tilt, j - 0° tilt) shows SEM images of CNT growths using iron oxide nanocluster arrays with a specified areal density on Al₂O₃-coated Si with C₂H₄/H₂/Ar flow rates of 200/500/0 sccm at 750°C. The figures correspond to the following iron oxide nanocluster densities: Figures a) and f) - $1.5 \times 10^{11} \text{ cm}^{-2}$; Figures b) and g) - $6 \times 10^{10} \text{ cm}^{-2}$; Figures c) and h) - $2.5 \times 10^{10} \text{ cm}^{-2}$; Figures d) and i) - $1.1 \times 10^{10} \text{ cm}^{-2}$.

cm⁻² (Inset shows a higher magnification image of one vertically-grown CNT column); and Figures e) and j) approximately 1×10^9 cm⁻².

When the areal density was further decreased to 1×10^{10} cm⁻² (Figures 4-5d and 4-5i), the overall density of the CNT growth decreased significantly. This sample showed sporadic columns of vertical CNT growth (inset of Figure 4-5i) surrounded by large areas with considerably less growth. The columns of vertically grown CNTs can be explained by a local variation in the iron oxide nanocluster areal density that results from the loss of hexagonal order of the nanoclusters as the PS homopolymer is added. These results suggest that when the critical local areal density of nanoclusters is exceeded, free volume constraints cause the MWCNTs to grow vertically from the substrate, leading to columns of vertically-grown MWCNTs held together by van der Waals forces. Alternatively, when the local areal density of nanoclusters is below the critical value, the growing MWCNTs do not grow vertically due to an increase in the free volume available, leading to tangled MWCNT growth. When the areal density was decreased to 1×10^9 cm⁻² (Figures 4-5e and 4-5j), no vertical growth of CNTs was observed. Comparing Figures 4-5i and 4-5j shows that the density of the CNT growth was significantly reduced and the average distance between CNTs increased noticeably. For the sample in Figure 4-5j, the areal density was low enough that the local variations in the areal density did not exceed the critical local areal density; therefore the vertical growth of MWCNTs was prevented altogether. The distributions of CNT diameters were nearly identical for each of the nanocluster areal densities tested, with CNT diameters of 12 ± 2 nm o.d. This result was expected because the diameters of the iron oxide nanoclusters remained constant as the areal density was varied.

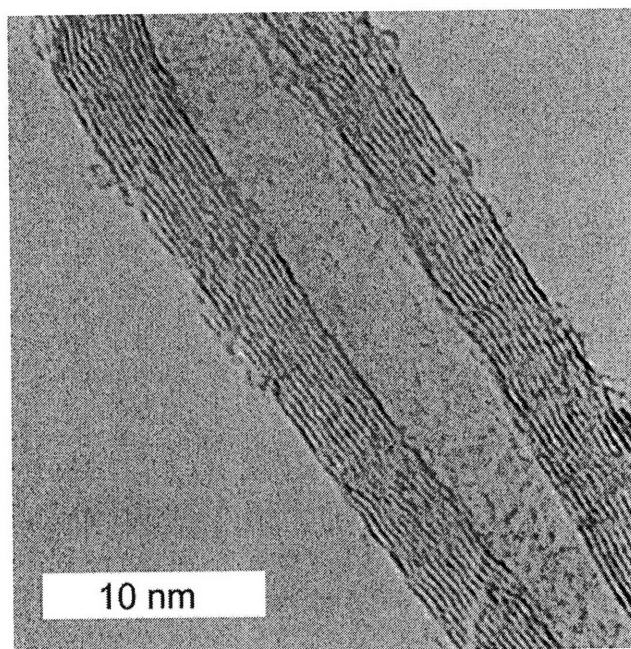


Figure 4-6. HRTEM image of a typical MWCNT grown from the micellar thin film catalysts.

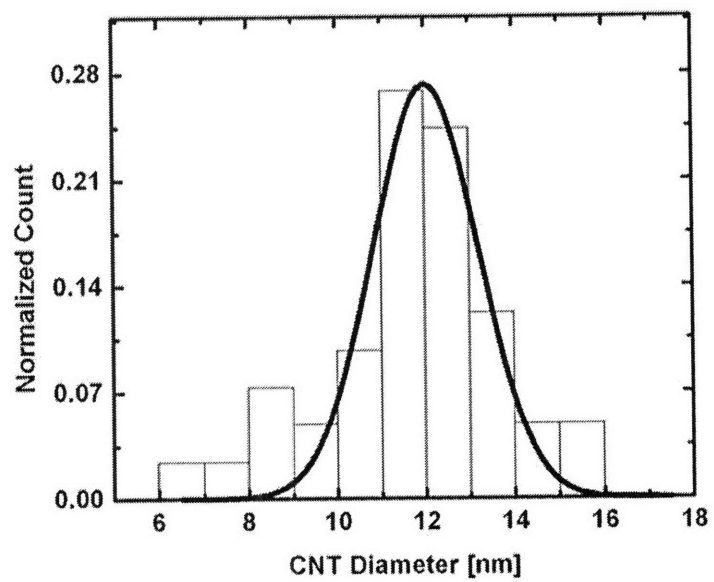


Figure 4-7. Diameter distribution of CNTs grown from 16 nm iron oxide nanoclusters with an areal density of $6 \times 10^{10} \text{ cm}^{-2}$ on Al_2O_3 -coated Si in 200/500/0 sccm $\text{C}_2\text{H}_4/\text{H}_2/\text{Ar}$ at 750°C .

Because the areal density of iron oxide nanoclusters created using our micellar route is readily available, the catalyst activity can be estimated for these vertically-grown CNT thin films. The catalyst activity is defined as the ratio of the CNT areal density to the areal density of the iron oxide nanoclusters. Because the iron oxide nanoclusters do not coalesce during the CNT growth process (demonstrated in the inset of Figure 4-2), the only unknown quantity is the CNT areal density. To calculate the CNT areal density, we determined the mass of the CNT film using thermogravimetric analysis (TGA). The average CNT diameter was $12 (\pm 2) \text{ nm}$, as determined from high-resolution TEM (HRTEM), which is shown in Figure 4-6. A histogram illustrating the distribution of CNT diameters is shown in Figure 4-7. The length of each CNT was estimated by observing the height of the bulk CNT film (Figure 4-4) and the side view of the vertically-grown MWCNT thin film (Figure 4-8) using SEM imaging. Figure 4-8 clearly demonstrates that the MWCNTs are not highly aligned, and are therefore longer than the height of the bulk MWCNT thin film. From the curvature of the CNTs in Figure 4-8, we estimate the length of the MWCNTs to be approximately 50% longer than the bulk thickness of the MWCNT thin film. By combining the length of the CNTs with the diameter and the number of concentric walls of the CNTs, the mass of an individual CNT can be estimated. The ratio of the mass of the CNT film to the mass of an individual CNT gives the number of CNTs, which can be converted to the CNT areal density by dividing by the substrate area. By using this analysis for the CNT growth substrate containing a

monolayer of iron oxide nanoclusters with uniform density (as shown in Figures 4-5b and 4-5g), we obtained a CNT areal density of $2.2 \times 10^9 \text{ cm}^{-2}$ (0.363 mg cm^{-2}). By comparing with the known iron oxide nanocluster density of $6.0 \times 10^{10} \text{ cm}^{-2}$, we obtained a catalyst activity of approximately 4%. This catalytic activity is very reasonable compared to the few percent catalyst activity observed in normal CVD growth, while considerably less than the 84% activity calculated for highly efficient water-assisted CNT growth¹⁸, as expected. Using this analysis for a CNT thin film grown from a nanocluster array created from a multilayer micellar thin film (as shown in Figures 4-5a and 4-5f), we obtained a CNT areal density of $5.2 \times 10^9 \text{ cm}^{-2}$ (0.879 mg cm^{-2}). By comparing the CNT areal density with the nanocluster areal density of $1.5 \times 10^{11} \text{ cm}^{-2}$, the catalytic activity for the multilayer nanocluster catalyst was determined to be approximately 4%. This suggests that while the areal density of the CNTs grown on the substrate varies as a function of the areal density of iron oxide nanoclusters, the percentage of nanoclusters catalyzing the growth of a CNT remains approximately constant.

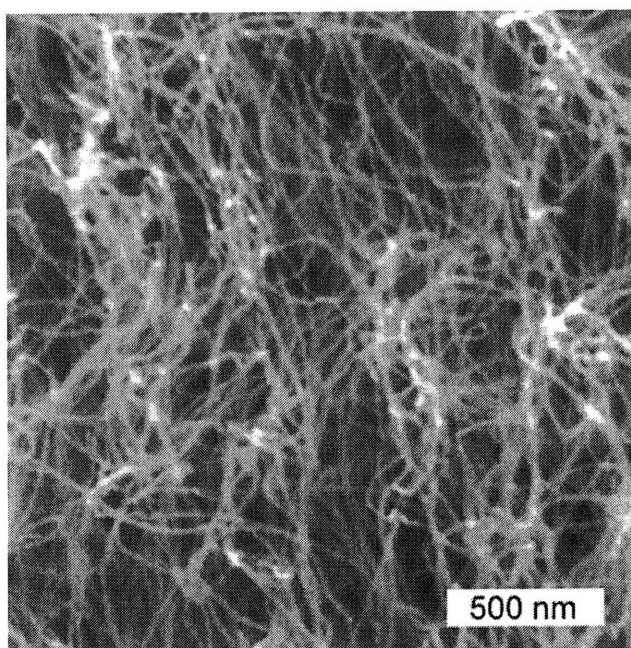


Figure 4-8. SEM image (85° tilt) of the side view of a vertical CNT film grown from 16 nm iron oxide nanoclusters with an areal density of $6 \times 10^{10} \text{ cm}^{-2}$ on Al_2O_3 -coated Si in 200/500/0 sccm $\text{C}_2\text{H}_4/\text{H}_2/\text{Ar}$ at 750°C.

The yield of the catalyst can also be quantified as the ratio of the mass of MWCNTs produced to the mass of iron in the catalyst nanoclusters. We can estimate the mass of iron in the nanoclusters by using a micelle aggregation number of 150 and assuming that the ratio of carboxylic acids groups to iron ions within the micelles was 3:1. For the iron oxide nanocluster array with an areal density of $6.0 \times 10^{10} \text{ cm}^{-2}$, there was $1.7 \times 10^{-5} \text{ mg cm}^{-2}$ of Fe. By comparing this to the mass of MWCNT per area, the yield of the nanocluster array was $2.1 \times 10^4 \text{ mg MWCNT / mg Fe}$. This yield can also be determined for an evaporated iron thin film catalyst subjected to identical CNT growth conditions⁷. The thickness (1.2 nm, as measured by Rutherford Backscattering Spectrometry) of the iron thin film was used to determine that the catalyst contains approximately $9.4 \times 10^{-4} \text{ mg cm}^{-2}$ of Fe after deposition. From the measured mass of MWCNT and the substrate area, the yield of the iron thin film was determined to be $1.2 \times 10^3 \text{ mg MWCNT / mg Fe}$. Comparing the yield of the nanocluster array versus the evaporated thin film suggests that the micelle-based nanocluster array more efficiently utilizes the iron molecules present on the substrate surface to convert the feed gases into MWCNTs.

4.4 Conclusion

In conclusion, our novel carbon nanotube catalyst system derived from spin-coated, iron-loaded PS-*b*-PAA micelles has significant advantages over other catalyst

systems. This block copolymer micellar catalyst system combines a unique ability to control the diameter, the areal density, and the composition of the nanoclusters, along with the ability to pattern the catalyst on a micron scale using microcontact printing techniques (presented in Chapter 5). Through the variation of substrates and growth conditions, as well as the removal of spin casting non-uniformities, we demonstrated the ability to catalyze vertical CNT growth from these iron oxide nanocluster arrays. Because these iron oxide nanocluster arrays have an easily quantifiable areal density, we were able to estimate that the catalyst activity for the vertical CNT growths was approximately 4%. The catalytic activity was approximately constant over the range of iron oxide nanocluster areal densities from $6 \times 10^{10} \text{ cm}^{-2}$ to $1.5 \times 10^{11} \text{ cm}^{-2}$. Furthermore, by varying the areal density of the iron oxide nanocluster arrays while maintaining a constant nanocluster diameter, we were able to control the morphology of the resulting CNT growth from dense vertical CNT films to an arrangement of sparse individual CNTs on the substrate surface. In our system, the critical areal density for growing a uniform vertical CNT film was between $2.5 \times 10^{10} \text{ cm}^{-2}$ and $6.0 \times 10^{10} \text{ cm}^{-2}$.

The control afforded by this micellar catalyst system could be promising for both CNT applications as well as for improved understanding of the combination of chemical and mechanical conditions necessary for growth of uniform CNT films. Using this micellar catalyst system, we can create multi-component nanocluster arrays of interest in CNT growth, such as iron / molybdenum containing particles. Particularly, we expect that the critical density for vertical growth depends on the catalyst composition and the CVD reaction conditions. Our approach could also be used to synthesize various other nanotubes and nanowires which grow from catalytic nanoparticles, including carbon

nitride nanotubes²⁹ that are produced in alternative CVD atmospheres. Our micellar catalyst system is a step toward precisely engineering the position, orientation, and density of nanostructures on substrates.

4.5 References

1. Iijima, S. *Nature* **1991**, *354*, 56-58.
2. Hata, K.; Futaba, D. N.; Mizuno, K.; Namai, T.; Yumura, M.; Iijima, S. *Science* **2004**, *306*, 1362-1364.
3. Pan, Z. W.; Xie, S. S.; Chang, B. H.; Wang, C. Y.; Lu, L.; Liu, W.; Zhou, M. Y.; Li, W. Z. *Nature* **1998**, *394*, 631-632.
4. Dai, H. J. *Surface Science* **2002**, *500*, 218-241.
5. Fan, S. S.; Chapline, M. G.; Franklin, N. R.; Tomblor, T. W.; Cassell, A. M.; Dai, H. J. *Science* **1999**, *283*, 512-514.
6. Murakami, Y.; Chiashi, S.; Miyauchi, Y.; Hu, M. H.; Ogura, M.; Okubo, T.; Maruyama, S. *Chemical Physics Letters* **2004**, *385*, 298-303.
7. Hart, A. J.; Slocum, A. H. *Journal of Physical Chemistry B* **2006**, *110*, 8250 - 8257.
8. Ren, Z. F.; Huang, Z. P.; Xu, J. W.; Wang, J. H.; Bush, P.; Siegal, M. P.; Provencio, P. N. *Science* **1998**, *282*, 1105-1107.
9. Hinds, B. J.; Chopra, N.; Rantell, T.; Andrews, R.; Gavalas, V.; Bachas, L. G. *Science* **2004**, *303*, 62-65.
10. Dresselhaus, M. S.; Dresselhaus, G.; Avouris, P. *Carbon Nanotubes: Synthesis, Structure, Properties, and Applications*; Springer: New York, 2001.
11. Baughman, R. H.; Zakhidov, A. A.; de Heer, W. A. *Science* **2002**, *297*, 787-792.
12. Huang, H.; Liu, C. H.; Wu, Y.; Fan, S. S. *Advanced Materials* **2005**, *17*, 1652.
13. Horibe, M.; Nihei, M.; Kondo, D.; Kawabata, A.; Awano, Y. *Japanese Journal of Applied Physics Part I* **2005**, *44*, 5309-5312.
14. Delzeit, L.; Nguyen, C. V.; Chen, B.; Stevens, R.; Cassell, A.; Han, J.; Meyyappan, M. *Journal of Physical Chemistry B* **2002**, *106*, 5629-5635.

15. Hart, A. J.; Slocum, A. H.; Royer, L. *Carbon* **2006**, *44*, 348-359.
16. Lacerda, R. G.; Teo, K. B. K.; Teh, A. S.; Yang, M. H.; Dalal, S. H.; Jefferson, D. A.; Durrell, J. H.; Rupesinghe, N. L.; Roy, D.; Amaratunga, G. A. J.; Milne, W. I.; Wyczisk, F.; Legagneux, P.; Chhowalla, M. *Journal of Applied Physics* **2004**, *96*, 4456-4462.
17. Hofmann, S.; Cantoro, M.; Kleinsorge, B.; Casiraghi, C.; Parvez, A.; Robertson, J.; Ducati, C. *Journal of Applied Physics* **2005**, *98*, 34308-34301.
18. Futaba, D.; Hata, K.; Namai, T.; Yamada, T.; Mizuno, K.; Hayamizu, Y.; Yumura, M.; Iijima, S. *Journal of Physical Chemistry B* **2006**, *110*, 8035.
19. Huh, Y.; Green, M. L. H.; Kim, Y. H.; Lee, J. Y.; Lee, C. J. *Applied Surface Science* **2005**, *249*, 145-150.
20. Zhang, L.; Tan, Y.; Resasco, D. *Chemical Physics Letters* **2006**, *422*, 198-203.
21. Boontongkong, Y.; Cohen, R. E. *Macromolecules* **2002**, *35*, 3647-3652.
22. Bennett, R. D.; Miller, A. C.; Kohen, N. T.; Hammond, P. T.; Irvine, D. J.; Cohen, R. E. *Macromolecules* **2005**, *38*, 10728-10735.
23. Bennett, R. D.; Hart, A. J.; Miller, A. C.; Hammond, P. T.; Irvine, D. J.; Cohen, R. E. *Langmuir* **2006**, *22*, 8273.
24. Bennett, R. D.; Xiong, G. Y.; Ren, Z. F.; Cohen, R. E. *Chemistry of Materials* **2004**, *16*, 5589-5595.
25. Yun, S. H.; Sohn, B. H.; Jung, J. C.; Zin, W. C.; Lee, J. K.; Song, O. *Langmuir* **2005**, *21*, 6548-6552.
26. de los Arcos, T.; Garnier, M. G.; Seo, J. W.; Oelhafen, P.; Thommen, V.; Mathys, D. *Journal of Physical Chemistry B* **2004**, *108*, 7728-7734.
27. Cheung, C. L.; Kurtz, A.; Park, H.; Lieber, C. M. *Journal of Physical Chemistry B* **2002**, *106*, 2429-2433.
28. Extrand, C. W. *Polymer Engineering and Science* **1994**, *34*, 390-394.
29. Zhong, D.; Liu, S.; Zhang, G.; Wang, E. G. *Journal of Applied Physics* **2001**, *11*, 5939.

Chapter 5 Patterning of Block Copolymer Micellar Thin Films Using Microcontact Printing and Their Applications in Carbon Nanotube Synthesis*

5.1 Introduction

Reliable and facile patterning of substrates is an important technological challenge. Patterning using soft lithography¹⁻⁴, which relies on using an elastomeric polymer to replicate a hard master, has successfully emerged as a fast, inexpensive, and straightforward route for patterning substrates⁵.

Microcontact printing (μ CP) is a powerful soft lithographic patterning technique that has received much attention since its development roughly a decade ago⁶⁻⁸. While μ CP was originally utilized to pattern self-assembled monolayers of alkane thiols on gold⁷, this technique has also been shown to be effective in patterning polymeric thin films^{5,9-13}. In general, this approach consists of wetting or “inking” a poly(dimethylsiloxane) (PDMS) stamp with a polymer solution, followed by transferring the polymeric thin film to the substrate. Harnessing the competitive interplay of surface energies and wetting behavior of the components is central to successful printing using this technique.

* Portions of this chapter have been previously published in Bennett, R.D., Hart, A.J., Miller, A.C., Hammond, P.T., Irvine, D.J., Cohen, R.E. *Langmuir* **2006**, 22, 8273 – 8276.

Amphiphilic block copolymer micelles in organic solvents represent a novel type of polymer solution from which micelles are capable of self-assembling into nanoscale ordered structures when deposited onto a surface¹⁴⁻¹⁶. These block copolymer micellar systems have been utilized for various applications, including creating inorganic nanoclusters for: carbon nanotube^{14,17} and zinc oxide nanowire growth¹⁸, protein binding¹⁹, and magnetic applications²⁰. For many of the applications of these systems, it would be very useful to pattern these block copolymer micellar thin films on a micron length scale or smaller to complement the inherent nanostructure of the thin films. In previous work, block copolymer micellar thin films have been patterned using both electron beam lithography and photolithography²¹⁻²³. While these routes have been effective for patterning on length scales as small as 100 nm, these routes are time-consuming, expensive, and equipment intensive. Recently Yun *et al*²³ developed a soft-lithographic method for patterning polystyrene-*block*-poly(4-vinylpyridine) (PS-*b*-PVP) micelles onto a substrate utilizing μ CP. In this approach, a toluene-based solution of PS-*b*-PVP micelles loaded with FeCl₃ was spin-coated onto a PDMS stamp and then transferred to a silicon (Si) substrate through μ CP. This route achieved micron-scale patterning of PS-*b*-PVP micellar thin films, which were subsequently oxygen plasma etched to create a monolayer of iron oxide nanoclusters.

In this chapter we present a soft-lithographic route for fabricating patterned block copolymer micellar thin films that utilizes dip-coating to ink the PDMS stamp prior to μ CP. In our approach we utilize the amphiphilic block copolymer, poly(styrene-*block*-acrylic acid) (PS-*b*-PAA), which forms spherical micelles when added to a toluene solution and heated¹⁴⁻¹⁶. After inking a PDMS stamp with this micellar solution using dip

coating, we allow the toluene to evaporate before transferring the patterned block copolymer thin films onto a substrate through μ CP. We demonstrate the ability to control the size, periodicity, and characteristic shape of the patterned areas through variation of the PDMS stamp geometry. While confirming the results of Yun *et al*²³ by demonstrating the ability to transfer PS-based block copolymer micellar thin films from a PDMS stamp to a Si substrate, we also identify interesting wetting behavior that we believe is due to the inhomogeneous swelling of the PDMS stamp in toluene during dip-coating. This swelling causes the patterned micellar thin films to have feature dimensions that are smaller than the corresponding PDMS stamp dimensions, while the periodicity of the patterned micellar thin films corresponds to the PDMS stamp periodicity. This behavior allows us to pattern stripes and circles of micellar thin films on submicron length scales. We also demonstrate the effect of varying the removal velocity of the PDMS stamp from the micellar solution, which alters the deposition of the micellar thin film onto the PDMS stamp. By varying the removal velocity we are able to create both positive and negative replications of the PDMS stamp with micellar thin films. We characterize these patterned substrates using optical microscopy as well as atomic force microscopy (AFM). Using the latter technique we also confirm that the PS-*b*-PAA thin films maintain their micellar nanostructure upon printing.

We further utilize our μ CP approach to pattern PS-*b*-PAA micellar thin films as organized catalyst templates for carbon nanotube (CNT) growth. In previous work, CNT growth catalysts have primarily been patterned using lithographic methods following physical deposition of metal thin films^{24,25}, although some work has been done using block copolymers containing covalently-bound iron molecules to create catalysts^{26,27}.

Using our μ CP approach, we pattern a PS-*b*-PAA micellar thin film using a block copolymer micellar inking solution that had been previously loaded with FeCl₃ onto a Si wafer coated with aluminum oxide (Al₂O₃). Oxygen plasma etching is utilized to remove the organic components of the micellar thin film to leave a patterned iron oxide nanocluster array. We then utilize the catalytic function of these patterned iron oxide nanocluster arrays, along with our previous knowledge of growth conditions for these catalyst systems²⁸, to synthesize patterned arrays of vertically-grown multi-wall carbon nanotubes (CNT) that are characterized using scanning electron microscopy (SEM). We observe that the fidelity of the pattern is maintained as the CNTs grow vertically from the substrate to heights that are two orders of magnitude larger than the characteristic pattern width.

5.2 Experimental Section

5.2.1 Materials

Poly(styrene-*block*-acrylic acid) (PS-*b*-PAA) [M_n (PS) = 16 400 g/mol, M_n (PAA) = 4 500 g/mol, PDI = 1.05] was used as received from Polymer Source, Inc. PDMS stamps were synthesized by pouring a two-component curable siloxane (Sylgard 184, Dow Corning) over a silicon master with the desired pattern. The following chemicals were also used as received: anhydrous iron(III) chloride (FeCl₃) obtained from Sigma-Aldrich Co., and toluene (HPLC grade, 99.8%) obtained from Sigma-Aldrich Co. Polished, single crystal silicon (Si) wafers (p-type) were used as received from WaferNet, Inc. Carbon nanotubes were synthesized on clean silicon wafers (p-type, Silicon Quest

International), which were coated with a 15 nm film of Al_2O_3 by electron beam evaporation using a Temescal VES-2550, with a FDC-8000 Film Deposition Controller. CNT growth²⁸ was performed in a conventional single-zone atmospheric pressure quartz tube furnace having an inside diameter of 22 mm and a heating zone of 30 cm. Argon (Ar, 99.999%, Airgas), ethylene (C_2H_4 , 99.5%, Airgas), and hydrogen (H_2 , 99.999%, BOC) were used as received.

5.2.2 Sample Preparation

PS-*b*-PAA was mixed with toluene at a concentration of 5.5 mg/mL and heated to 145 °C for 20 min in a sealed vial to create a spherical block copolymer micellar solution. Details about the formation of spherical block copolymer micelles in solution have been presented in previous publications¹⁴⁻¹⁶. The μ CP procedure is illustrated schematically in Figure 5-1. Two stamp geometries were utilized: channeled PDMS stamps had a constant feature height of 400 nm (variable aspect ratio from 2.5 to 20), while the cylindrical post PDMS stamps had a constant aspect ratio of 1. The untreated PDMS stamps were inked by dipping the stamps into the micellar solution with the patterned surface oriented vertically. Maintaining this orientation, the PDMS stamps were submerged in the solution for 3 s, and then removed at a rate of .5 – 2 mm s⁻¹. The PDMS stamps were then allowed to dry for 4 min with the patterned surface oriented vertically, and then rotated to dry for 1 min with the patterned surface oriented horizontally. The PDMS stamps were then placed in contact with an untreated Si substrate for 3-5 min and a mechanical pressure was applied. For the channeled PDMS stamps, the applied pressure for a stamp with a feature width of 8 μm was approximately 40 kPa, while the applied pressure for the stamp with 1 μm diameter posts was approximately 180 kPa. An excessive stamping pressure

caused the entire stamp (both the raised and recessed features) to contact the substrate (which was easily observed visually during stamping), in which case the applied pressure was reduced for proper stamping. The stamps were slowly peeled from the substrate to leave a patterned block copolymer micellar film on the substrate.

For the preparation of iron oxide nanocluster arrays, FeCl_3 was added to a 5 mg/mL spherical PS-*b*-PAA micellar solution at a ratio of 5.4 metal ion equivalents per carboxylic acid group¹⁵. The μCP printing procedure was then used to pattern the iron-containing PS-*b*-PAA micellar thin film onto an Al_2O_3 -coated Si wafer. Al_2O_3 -coated substrates have been previously shown to be effective supporting layers for CNT growth using Fe-based catalysts²⁸⁻³⁰. The patterned substrate was then oxygen plasma etched (rf plasma, 8-12 MHz) for 15 – 20 min to remove the polymer thin film, leaving only iron oxide nanoclusters remaining on the substrate¹⁴. Details about our procedure for synthesizing vertically-grown CNTs have been discussed previously²⁸. In brief, the substrate was placed in a quartz tube reactor, covered by a silicon wafer shield, and ramped to 750 °C under a 400 sccm flow of Ar for 30 min. The substrate was held at 750 °C under Ar for 14 min; then Ar was reduced to 200 sccm and 500 sccm H_2 was introduced for 1 min. Ar was then reduced to 0 sccm and 200 sccm C_2H_4 was introduced with 500 sccm H_2 for 15 min. Following growth, the furnace was flushed with Ar and cooled to room temperature.

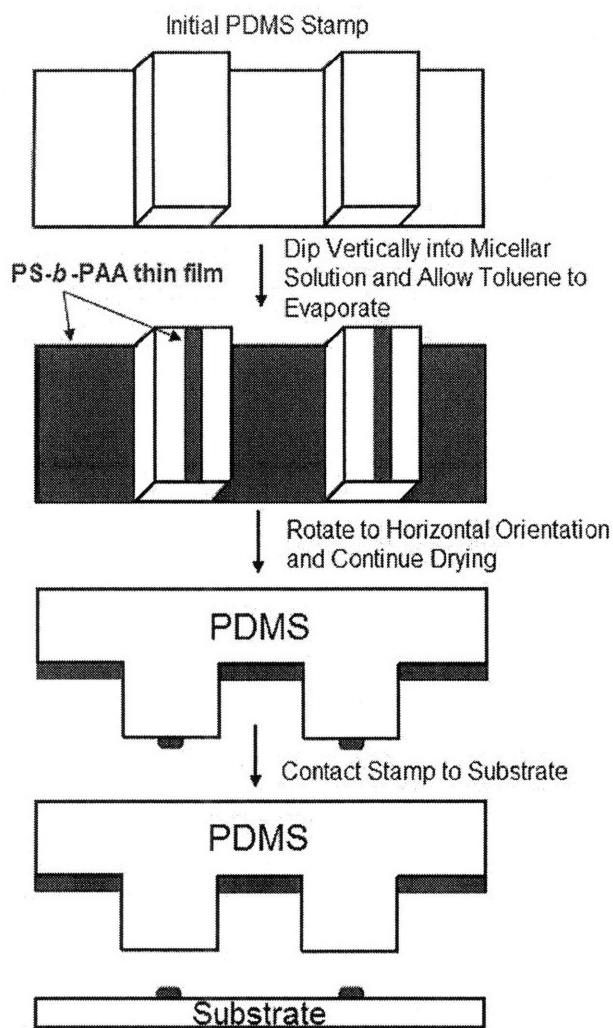


Figure 5-1. Schematic illustration of the μ CP of block copolymer micellar thin films using a PDMS stamp. The dimensions of the inked regions on the stamps are shown to be smaller than the characteristic size of the stamp feature dimensions, consistent with microscopic observations presented below. Unless excessive stamping pressure is used, only the micellar regions from the raised features are transferred to the substrate, as shown here.

5.2.3 Characterization

The patterned films were examined using a Leica optical microscope equipped with a Nikon digital camera (DXM 1200F) using Nikon imaging software (ACT-1, Version 2). Images were obtained in reflectance mode. Atomic force microscopy (AFM) images were obtained using a Digital Instruments Dimension 3000 Nanoscope IIIA scanning probe microscope operating in tapping mode using a silicon cantilever. Scanning electron microscopy (SEM) images were obtained using a JEOL 6320FV field-emission high-resolution microscope operating at 5 kV.

5.3 Results and Discussion

5.3.1 *Microcontact Printing of Block Copolymer Micellar Thin Films*

The optical microscope images in Figure 5-2 demonstrate the effectiveness of using μ CP to pattern PS-*b*-PAA micellar thin films. The results observed in Figure 5-2 are quantified in Table 5-1, which shows that by varying the width of the raised PDMS features from 1 μ m to 8 μ m, we can vary the width of the PS-*b*-PAA patterns from 0.5 to 1.5 μ m. The data in Table 5-1 also indicate that the patterned PS-*b*-PAA stripes had a width that was considerably smaller than the original width of the PDMS stamp. We believe that this effect was caused by the inhomogeneous swelling of the PDMS stamp. Because the edges of the PDMS channel have more surface area exposed to toluene, the edges achieved a higher degree of swelling than the inner region. This inhomogeneous swelling of the PDMS in toluene caused the micelle solution to collect towards the centerline of the PDMS features (See Figure 5-1). This effect has been documented previously in the μ CP of a poly(styrene-*alt*-maleic anhydride)/tetrahydrofuran system⁹. In

the present case, once the toluene evaporated, the PS-*b*-PAA micellar thin film was kinetically trapped on the surfaces of the stamp features because the continuous PS matrix has a glass transition temperature that is well above room temperature.

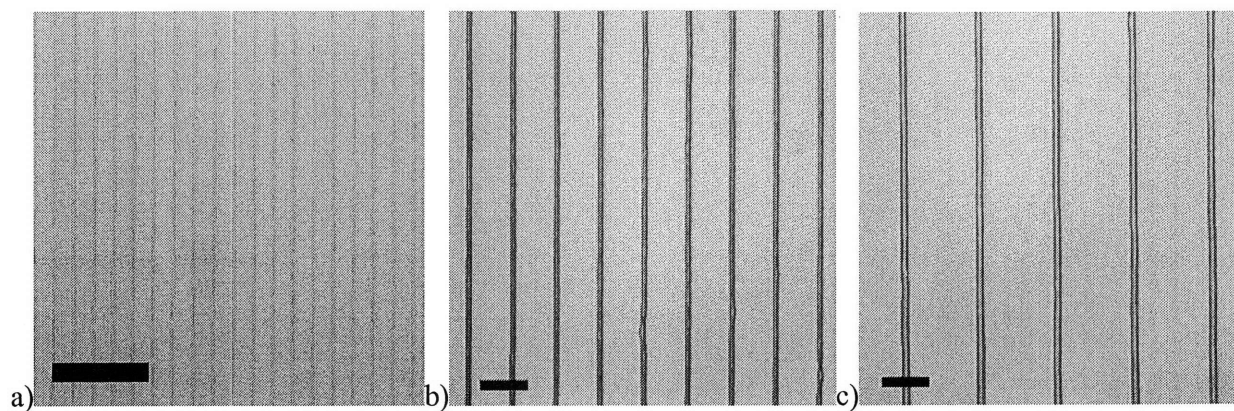


Figure 5-2. Optical microscope images of PS-*b*-PAA micellar thin films patterned using μ CP with a PDMS stamp with a feature width and periodicity of: (a) 1 μ m and 2 μ m, (b) 4.5 μ m and 9 μ m, and (c) 8 μ m and 16 μ m. Scale bar = 10 μ m.

Feature width of PDMS stamp (μ m)	Periodicity of PDMS stamp (μ m)	Width of patterned PS- <i>b</i> -PAA thin film (μ m)	Periodicity of patterned PS- <i>b</i> -PAA thin film (μ m)
1.0	2.0	0.5	2.0
4.5	9.0	0.9	8.9
8.0	16.0	1.5	15.8

Table 5-1. Effects of varying the feature width and periodicity of the PDMS stamp on the width and periodicity of the resulting PS-*b*-PAA micellar thin film features.

The optical microscope images in Figure 5-3 demonstrate the effect of using excessive stamping pressure. The patterns in this image were created using a PDMS stamp with 5 μ m wide features and a periodicity of 10 μ m using an applied pressure of 600 kPa. The regions of the patterned micellar thin films labeled “A” in Figure 5-3

correspond to material that was located on the top of the PDMS features prior to contacting the substrate, and these were the areas that transferred to the substrate with moderate applied pressures, as shown in Figure 5-2. The patterned areas labeled “B” in Figure 5-3 represent the micellar material that resided in the troughs between the raised features on the PDMS stamp. The light regions correspond to bare substrate. With lower applied pressures the troughs did not make contact with the substrate and were not printed, as demonstrated in Figure 5-2. When excessive pressure was applied, the micellar thin films located in the troughs contacted the surface and were transferred to the substrate. The inset in Figure 5-3 shows the region of the substrate that was patterned by the end of the raised features of the PDMS stamp. This image shows that the regions labeled “B” in Figure 5-3 continuously connect with the polymer thin film regions patterned where the raised features have ended, confirming that the regions labeled “B” were transferred from the troughs of the PDMS stamp. The width of the films labeled “B” in Figure 5-3 correspond exactly to the width of the troughs of the PDMS stamp, giving more evidence for the proposed mechanism. The regions labeled “A” were transferred from the raised features of the PDMS stamps, and these patterned areas end where the raised features of the PDMS stamp end. The inset in Figure 5-3 also corroborates the inhomogeneous swelling mechanism by showing that the patterned thin films from the top of the raised features do not extend to the end of the PDMS raised features, due to the higher swelling at the end of the raised features. The regions labeled “B” in Figure 5-3 exhibit a distinct three-fold structure along their edges; we are unsure of the mechanism for its formation.

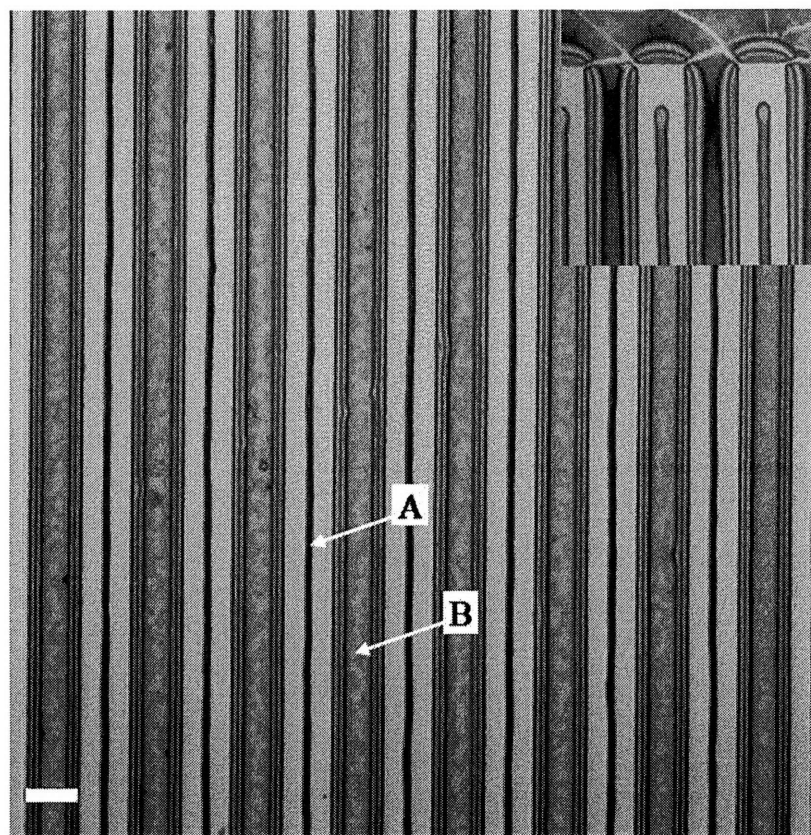


Figure 5-3. Optical microscope image of a PS-*b*-PAA micellar thin film patterned using μ CP with an applied pressure of 600 kPa and a PDMS stamp with a channel width of 5 μ m and a periodicity of 10 μ m. The narrow patterned films labeled “A” in the image correspond to the micellar thin films that originally were located on the raised PDMS features prior to stamping. The regions labeled “B” in the image correspond to micellar thin films that were originally located in the troughs of the PDMS prior to stamping. The inset shows the patterned substrate at the edge of the PDMS stamp. Scale bar = 5 μ m.

Figure 5-4 shows the AFM characterization of the PS-*b*-PAA micellar thin films patterned by using a PDMS stamp with a channel width of 7 μ m and a periodicity of 14 μ m and an applied pressure of 40 kPa. Figure 5-4a shows an AFM height image of the substrate after stamping. The thickness of the patterned micellar thin films is

demonstrated in Figure 5-4b, which shows an individual scan line between the two triangles shown in Figure 5-4a. This shows that the patterned stripes are approximately 100 nm thick and are uniform in shape. To confirm that the micellar substructure persisted in the patterned areas, we examined the areas indicated by the white squares in Figure 5-4a at higher resolution. Figure 5-4c shows the AFM phase image of the patterned micellar thin film that is located in the square labeled “c)” in Figure 5-4a. The observed structure is identical to previous AFM images of micellar thin films^{14,16} of this same block copolymer, and verifies the nanoscale sub-structure of the patterned thin films. Figure 5-4d shows the AFM phase image of the area indicated by the square labeled “d)” in Figure 5-4a and corresponds to the smooth structure of the bare Si substrate. From these AFM results we are able to conclude that our μ CP procedure enables the creation of substrates with well-defined patterns of PS-*b*-PAA micellar thin films. The thickness of the patterned stripes suggests there are 4 - 5 layers of micelles, as compared to the micellar monolayers that could be created using a spin casting approach^{15,16}. The cracks observed in Figure 5-4a are believed to arise from stresses that are imparted to the glassy polymer thin films during handling of the PDMS stamp during the stamping procedure. We have found that these cracks can be minimized by delicately handling the PDMS stamps during the stamping procedure.

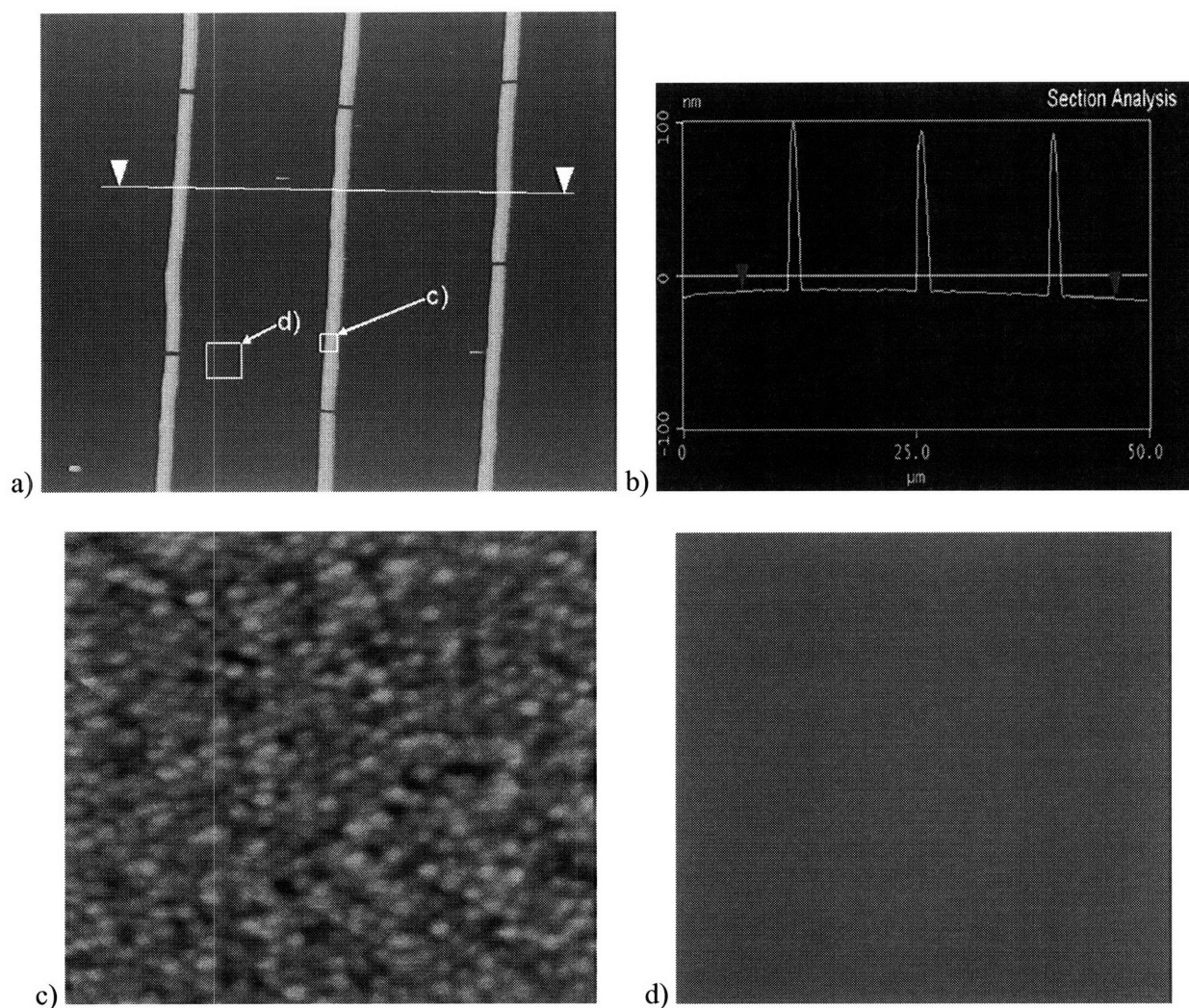


Figure 5-4. AFM characterization of a PS-*b*-PAA micellar thin film patterned using a PDMS stamp having a channel width of 7 μm and a periodicity of 14 μm . (a) AFM height image (50 μm by 50 μm scan) showing a patterned PS-*b*-PAA micellar thin film on a Si substrate; (b) Plot of individual scan line along the line connecting the two white triangles in (a); (c) AFM phase image (0.6 μm by 0.6 μm scan, 50° scale) from the square denoted “c)”; (d) AFM phase image (2.5 μm by 2.5 μm scan, 50° scale) from the square area denoted “d)”.

The optical microscope images in Figure 5-5 demonstrate the capability of using this μ CP procedure to pattern PS-*b*-PAA micellar thin films in other geometries. The micellar thin films observed in Figure 5-5 were obtained using a PDMS stamp with cylindrical post features and a removal velocity of 1 mm s^{-1} . The results are quantified in Table 5-2. Figures 5-5a – 5-5c demonstrate the ability to vary the periodicity of the resulting PS-*b*-PAA micellar thin film patterns from $6.1 \text{ }\mu\text{m}$ to $17.5 \text{ }\mu\text{m}$. In these images the diameters of the patterned micellar areas varied between $0.5 \text{ }\mu\text{m}$ and $0.6 \text{ }\mu\text{m}$, which is much smaller than the diameter of the cylindrical posts on the PDMS stamp and similar to the result that was observed for the PDMS stamp with linear features (see Figure 5-2 and Table 5-1).

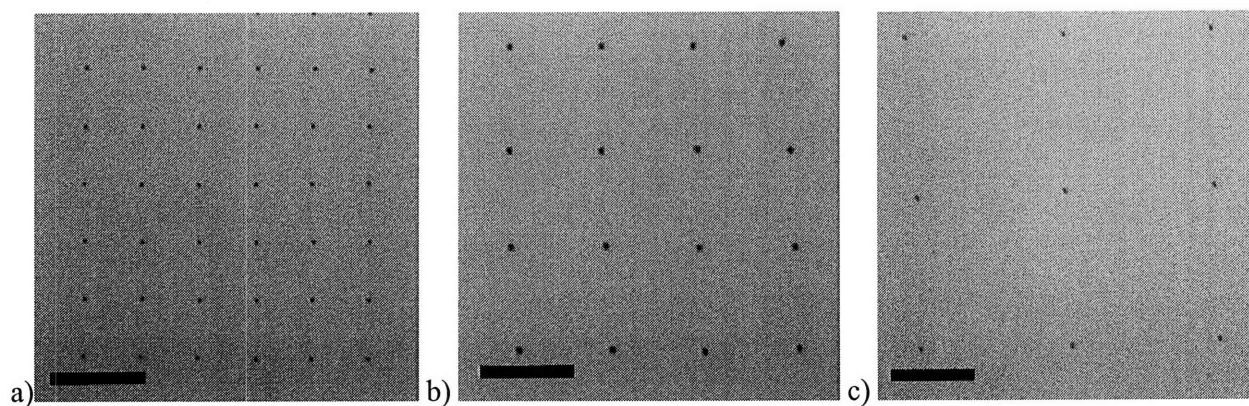


Figure 5-5. Optical microscope images of PS-*b*-PAA micellar thin films patterned using μ CP with a PDMS stamp of cylindrical posts with a removal velocity of 1 mm s^{-1} and with a diameter and periodicity of: (a) $4 \text{ }\mu\text{m}$ and $6 \text{ }\mu\text{m}$, (b) $4 \text{ }\mu\text{m}$ and $10 \text{ }\mu\text{m}$, and (c) $3 \text{ }\mu\text{m}$ and $18 \text{ }\mu\text{m}$. Scale bar = $10 \text{ }\mu\text{m}$.

Diameter of posts on PDMS stamp (um)	Periodicity of posts on PDMS stamp (um)	Diameter of patterned PS- <i>b</i> -PAA thin film (um)	Periodicity of patterned PS- <i>b</i> -PAA thin film (um)
4.0	6.0	0.6	6.1
4.0	10.0	0.6	9.6
3.0	18.0	0.5	17.5

Table 5-2. Effects of varying the diameter and periodicity of cylindrical posts on a PDMS stamp on the diameter and periodicity of the resulting patterned PS-*b*-PAA micellar thin film.

Although the μ CP of stripes of micellar thin films was relatively insensitive to the removal velocity of the PDMS stamp from the inking solution, μ CP using PDMS stamps with cylindrical posts was quite sensitive to the PDMS stamp removal velocity. For the results in Figure 5-5, a removal velocity of 1 mm s^{-1} caused micellar thin films to deposit onto the tops of the cylindrical posts and subsequently transfer to the Si substrate. When the removal velocity of the PDMS stamp with cylindrical posts was lowered to 0.2 mm s^{-1} , the micellar thin films did not deposit onto the tops of the cylindrical posts, as demonstrated in Figure 5-6a. Figure 5-6a shows an optical microscope image of a PS-*b*-PAA micellar thin film patterned using μ CP with an applied pressure of 600 kPa using a PDMS stamp of cylindrical posts with diameters of 4 μm and a periodicity of 8 μm . Because of the large applied pressure, inked material from both the top of the raised features and the troughs should transfer from the PDMS stamp to the substrate. In this image, however, the well-defined circles correspond to bare substrate indicating that the cylindrical posts did not have micellar thin films deposited on their top surfaces due to the slower removal velocity. In Figure 5-6b, an optical microscope image shows a PS-*b*-PAA micellar thin film patterned using an applied pressure of 600 kPa using a PDMS stamp of cylindrical posts with a diameter of 4 μm and a periodicity of 10 μm and a

removal velocity of 1 mm s^{-1} . In this image the PS-*b*-PAA micellar thin film did ink the tops of the cylindrical posts, and was subsequently transferred to the substrate along with the micellar thin film from the trough. Thus by varying the removal velocity of the PDMS stamp from the micellar solution and the applied pressure, we were able to create positive, negative, and mixed representations of the PDMS stamp using a PS-*b*-PAA micellar thin film.

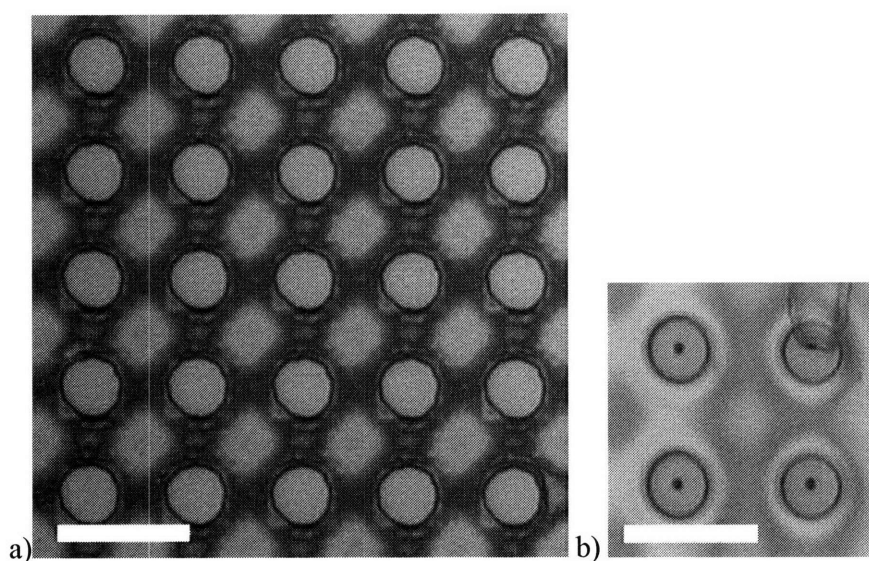
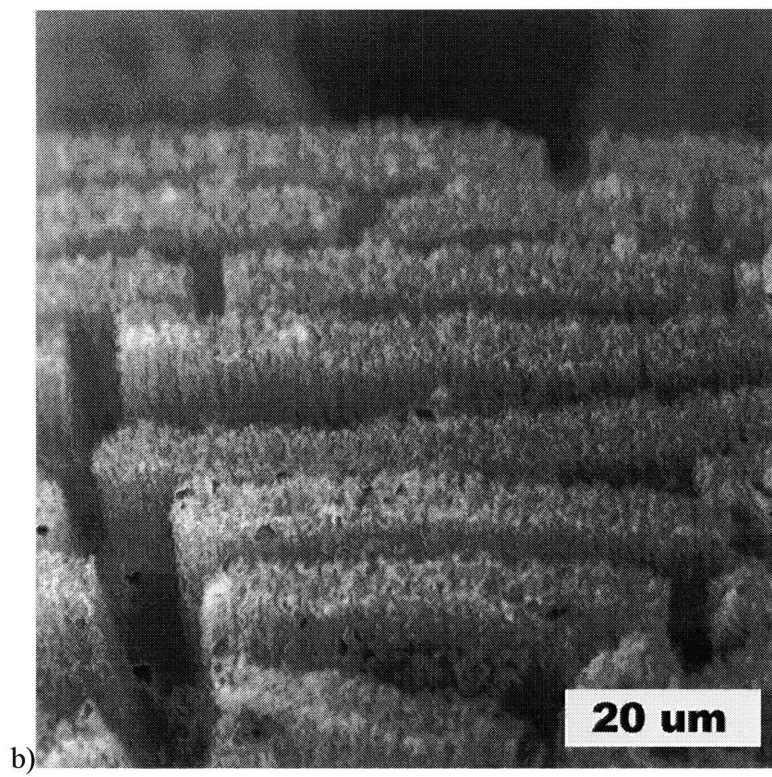
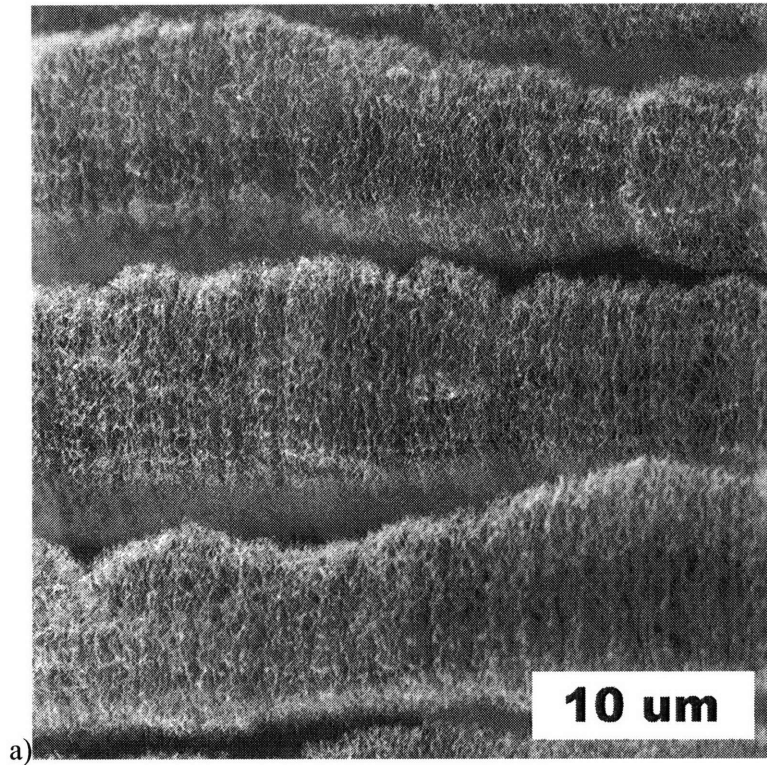


Figure 5-6. (a) Optical microscope image of a PS-*b*-PAA micellar thin film patterned using μ CP with an applied pressure of 600 kPa using a PDMS stamp of cylindrical posts with diameters of 4 μm and a periodicity of 8 μm and a removal velocity of 0.2 mm s^{-1} . The lighter areas correspond to bare substrate, while the darker areas correspond to PS-*b*-PAA micellar thin film. (b) Optical microscope image of a PS-*b*-PAA micellar thin film patterned using μ CP with an applied pressure of 600 kPa using a PDMS stamp of cylindrical posts with diameters of 4 μm and a periodicity of 10 μm and a removal velocity of 1 mm s^{-1} . Scale bars = 10 μm .

5.3.2 Carbon Nanotube Growth from Patterned Catalysts

In previous research we successfully exploited micellar thin films in a scheme that first led to a full-area-coverage of planar arrays of substrate-bound iron oxide nanoclusters, followed by their use as catalysts for the synthesis of multi-wall carbon nanotubes (MWCNTs)¹⁴. We also showed that iron ions added to a solution of spherical PS-*b*-PAA micelles will selectively load into the core of the micelles, thereby permitting the creation of iron oxide nanocluster arrays via spin casting¹⁵. Using this PS-*b*-PAA micellar system, we also demonstrated the ability to create iron oxide nanocluster catalysts for vertical growth of MWCNTs²⁸. This was accomplished by varying the CVD growth parameters, the substrate, and the uniformity of the micellar thin film, in order to discover a set of conditions that yielded dense growth of MWCNTs. In this chapter we patterned iron-loaded PS-*b*-PAA micellar thin films onto Al₂O₃-coated Si substrates using our μ CP procedure. Oxygen plasma etching was used to remove the organic component of the micellar thin film, leaving patterned iron oxide nanocluster arrays. These patterned inorganic nanocluster arrays were examined in the context of nanotube catalysis and growth using our knowledge of conditions for CNT synthesis using this catalyst system.



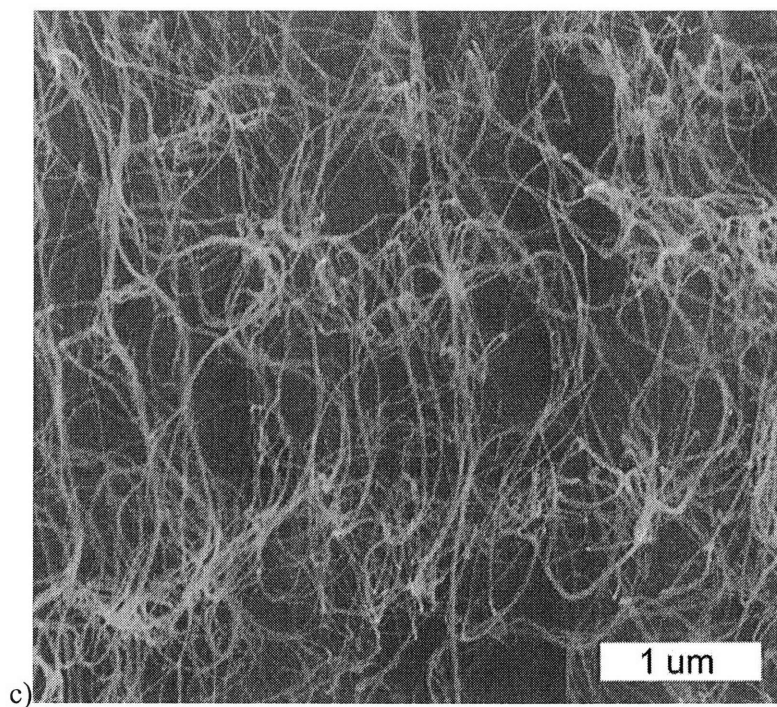


Figure 5-7. SEM micrographs of vertically-grown MWCNT structures grown from an FeCl_3 -loaded PS-*b*-PAA micellar thin film patterned onto an Al_2O_3 -coated Si substrate using a μCP approach with a channeled PDMS stamp with a width of 5 μm and a periodicity of 10 μm . The CNT synthesis used 200/500 sccm of $\text{C}_2\text{H}_4/\text{H}_2$ at 750 $^\circ\text{C}$ for 15 min. a) Overhead view (0° tilt); b) Side view (70° tilt); c) Higher magnification image of side of vertically-grown MWCNT structures (45° tilt).

The SEM micrographs in Figure 5-7 show the result for a CNT growth using an iron oxide nanocluster array patterned using a channeled PDMS stamp with a width of 5 μm and a periodicity of 10 μm . The images show dense “walls” of MWCNTs that have grown vertically from the substrate. It is clear that these CNTs, which were grown from a patterned strip of catalyst nanoclusters, retain the individual shape of the underlying pattern even though the height of these structures is roughly two orders of magnitude larger than the width of the patterns. Similar results have been observed for vertical

growth of CNTs using thin metal films patterned by electron beam evaporation^{24,25}. It is believed that strong van der Waals forces between the CNTs cause the CNT structures to retain the shape of the patterned nanocluster catalysts as the structures grow vertically from the substrate.

The SEM micrographs in Figure 5-8 show the result of a CNT growth using an iron oxide nanocluster array patterned using a PDMS stamp of cylindrical posts with diameters of 4 μm and a periodicity of 8 μm using a removal velocity of 0.2 mm s^{-1} and an applied pressure of 600 kPa. These conditions resulted in a transferred micellar thin film that was the negative of the original PDMS stamp, as shown in Figure 5-6a. The left image in Figure 5-8 shows a representative result from the growth, while the right image in Figure 5-8 shows the edge of the patterned area to demonstrate the vertical aspect of the growth. As in the CNT growth from channeled catalysts, it is clear from Figure 5-8 that the CNTs were catalyzed only from the patterned areas of the substrate. The CNTs also clearly maintain the patterned structure as they grow vertically from the substrate, even though the aspect ratio of the cylindrical columns is approximately 100. The MWCNT structures grown from the continuous circular pattern in Figure 5-8 appear to more accurately maintain the dimensions of the patterned catalyst as compared to the MWCNT structures grown from strips of patterned catalyst in Figure 5-7. We are currently unsure of the explanation for this observation and we plan to continue to investigate this topic in the future.

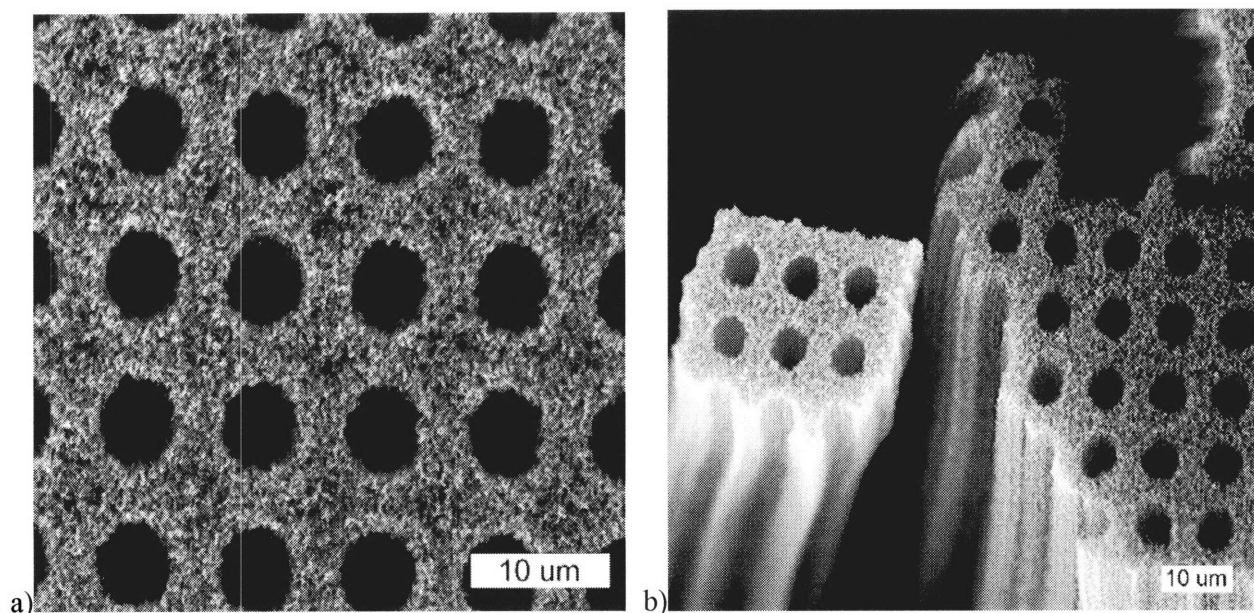


Figure 5-8. SEM micrographs of vertically-oriented MWCNT structures grown from an FeCl_3 -loaded PS-*b*-PAA micellar thin film patterned onto an Al_2O_3 -coated Si substrate using a μCP approach with a PDMS stamp with cylindrical posts having diameters of 4 μm and a periodicity of 8 μm . The PDMS stamp was removed from the micellar solution at 0.2 mm s^{-1} and stamped using 600 kPa of pressure to create the inverse pattern on the substrate. The CNT synthesis consisted of 200/500 sccm of $\text{C}_2\text{H}_4/\text{H}_2$ at 750°C for 15 min. a) Overhead view (0° tilt); b) Side view (45° tilt).

5.4 Conclusion

We have demonstrated a simple, effective, and easily accessible route for patterning PS-*b*-PAA micellar thin films using a μCP approach. We demonstrate the ability to create patterned features, while also varying their characteristic length, periodicity, and their characteristic shape. We also used AFM to characterize the

structure of our patterned substrates as well as to verify that the patterned thin films maintain their micellar structure. Because these micellar thin films are capable of acting as both templates to create inorganic nanoclusters and as nanoreactors, we believe that the ability to pattern these block copolymer micellar thin films will have many useful applications. We demonstrated one possible application by creating patterned iron oxide nanocluster arrays that were able to catalyze vertical growth of carbon nanotubes selectively on the patterned regions of the substrate. We are continuing our investigation of μ CP-patterned PS-*b*-PAA micellar thin films; studies of carbon nanotube and zinc oxide nanowire synthesis, as well as the templating of biologically-active molecules for modifying cell attachment and function will be pursued.

5.5 References

1. Whitesides, G. M.; Ostuni, E.; Takayama, S.; Jiang, X. Y.; Ingber, D. E. *Ann. Rev. of Biomedical Eng.* **2001**, *3*, 335-373.
2. Xia, Y. N.; Whitesides, G. M. *Ann. Rev. Mat. Sci.* **1998**, *28*, 153-184.
3. Kane, R. S.; Takayama, S.; Ostuni, E.; Ingber, D. E.; Whitesides, G. M. *Biomaterials* **1999**, *20*, 2363-2376.
4. Zhao, X. M.; Xia, Y. N.; Whitesides, G. M. *J. Mat. Chem.* **1997**, *7*, 1069-1074.
5. Jiang, X. P.; Zheng, H. P.; Gourdin, S.; Hammond, P. T. *Langmuir* **2002**, *18*, 2607-2615.
6. Kumar, A.; Whitesides, G. M. *App. Phys. Lett.* **1993**, *63*, 2002-2004.
7. Kumar, A.; Biebuyck, H. A.; Whitesides, G. M. *Langmuir* **1994**, *10*, 1498-1511.
8. Kumar, A.; Whitesides, G. M. *Science* **1994**, *263*, 60-62.
9. Wang, M. T.; Braun, H. G.; Kratzmuller, T.; Meyer, E. *Adv. Mater.* **2001**, *13*, 1312-1317.
10. Yan, L.; Huck, W. T. S.; Zhao, X. M.; Whitesides, G. M. *Langmuir* **1999**, *15*, 1208-1214.

11. Granlund, T.; Nyberg, T.; Roman, L. S.; Svensson, M.; Inganas, O. *Adv. Mater.* **2000**, *12*, 269-273.
12. Berg, M. C.; Choi, J.; Hammond, P. T.; Rubner, M. F. *Langmuir* **2003**, *19*, 2231-2237.
13. Tokuhisa, H.; Hammond, P. T. *Langmuir* **2004**, *20*, 1436-1441.
14. Bennett, R. D.; Xiong, G. Y.; Ren, Z. F.; Cohen, R. E. *Chem. Mater.* **2004**, *16*, 5589-5595.
15. Bennett, R. D.; Miller, A. C.; Kohen, N. T.; Hammond, P. T.; Irvine, D. J.; Cohen, R. E. *Macromolecules* **2005**, *38*, 10728-10735.
16. Boontongkong, Y.; Cohen, R. E. *Macromolecules* **2002**, *35*, 3647-3652.
17. Fu, Q.; Huang, S. M.; Liu, J. J. *Phys. Chem. B* **2004**, *108*, 6124-6129.
18. Haupt, M.; Ladenburger, A.; Sauer, R.; Thonke, K.; Glass, R.; Roos, W.; Spatz, J. P.; Rauscher, H.; Riethmuller, S.; Moller, M. *J. App. Phys.* **2003**, *93*, 6252-6257.
19. Spatz, J. P.; Mossmer, S.; Hartmann, C.; Moller, M.; Herzog, T.; Krieger, M.; Boyen, H. G.; Ziemann, P.; Kabius, B. *Langmuir* **2000**, *16*, 407-415.
20. Yun, S. H.; Sohn, B. H.; Jung, J. C.; Zin, W. C.; Lee, J. K.; Song, O. *Langmuir* **2005**, *21*, 6548-6552.
21. Glass, R.; Moller, M.; Spatz, J. P. *Nanotechnology* **2003**, *14*, 1153-1160.
22. Glass, R.; Arnold, M.; Blummel, J.; Kuller, A.; Moller, M.; Spatz, J. P. *Adv. Func. Mater.* **2003**, *13*, 569-575.
23. Yun, S. H.; Sohn, B. H.; Jung, J. C.; Zin, W. C.; Ree, M.; Park, J. W. *Nanotechnology* **2006**, *17*, 450-454.
24. Hata, K.; Futaba, D. N.; Mizuno, K.; Namai, T.; Yumura, M.; Iijima, S. *Science* **2004**, *306*, 1362-1364.
25. Zhang, G. Y.; Mann, D.; Zhang, L.; Javey, A.; Li, Y. M.; Yenilmez, E.; Wang, Q.; McVittie, J. P.; Nishi, Y.; Gibbons, J.; Dai, H. J. *Proceedings of the National Academy of Sciences* **2005**, *102*, 16141-16145.
26. Lastella, S.; Jung, Y. J.; Yang, H. C.; Vajtai, R.; Ajayan, P. M.; Ryu, C. Y.; Rider, D. A.; Manners, I. *J. Mater. Chem.* **2004**, *14*, 1791-1794.

27. Lu, J. Q.; Kopley, T. E.; Moll, N.; Roitman, D.; Chamberlin, D.; Fu, Q.; Liu, J.; Russell, T. P.; Rider, D. A.; Manners, I.; Winnik, M. A. *Chem. Mater.* **2005**, *17*, 2227-2231.
28. Bennett, R. D.; Hart, A. J.; Cohen, R. E. *Advanced Materials* **2006**, *18*, 2274 - 2279.
29. de los Arcos, T.; Garnier, M. G.; Seo, J. W.; Oelhafen, P.; Thommen, V.; Mathys, D. *J. Phys. Chem. B* **2004**, *108*, 7728-7734.
30. Hart, A. J.; Slocum, A. H.; Royer, L. *Carbon* **2006**, *44*, 348-359.

Chapter 6 DNA Printing Using Au Nanocluster

Arrays Synthesized via Block Copolymer

Micellar Thin Films

6.1 Introduction

DNA microarrays are an increasingly important biological tool that have been used for a host of applications including examining gene expression¹, fundamentally studying cancer and genetic diseases^{2,3}, and for the screening of drugs based on their interactions with DNA⁴. The two commercial routes for creating DNA microarrays involve either *in situ* synthesis or *ex situ* spotting^{5,6}. *In situ* synthesis involves the addition of a nucleotide to a growing oligonucleotide that has been spatially arranged on a substrate via a photolithographic mask⁵. This process has the advantage of design flexibility, but the synthesis cycle consists of multiple steps and the length of the oligonucleotide is limited to approximately 60 basepairs^{6,7}. The other alternative is to spot pre-synthesized oligonucleotides to a substrate using either contact printing or by projection via nozzles⁸. The *ex situ* method doesn't limit the size of the oligonucleotides, but the cost of creating the DNA microarrays scales with the size of the substrate. Both of these routes are subject to an accumulation of errors due to their sequential processing and are not suited for creating more complex microarrays⁶.

Recently two independently developed techniques for replicating DNA microarrays have been discovered. In the first, Stellacci and coworkers^{9,10} presented a

novel printing technique, named Supramolecular Nano-Stamping (SuNS), that replicated single-stranded DNA (ssDNA) arrays through a hybridization – contact – dehybridization cycle. Their method generally relied on modified DNA to form bonds with the target substrate. In their case, a thiol – gold interaction was used to bind hexylthiol-modified DNA to a gold substrate⁹. A second route, developed by Crooks and coworkers^{11,12}, uses a similar approach but relies on the binding of streptavidin – biotin to fabricate the DNA microarrays.

In this chapter, the capabilities of synthesizing tunable gold nanocluster arrays via poly(styrene-*block*-2-vinylpyridine) (PS-*b*-P2VP) will be combined with the SuNS printing route to create DNA nanoarrays. PS-*b*-P2VP micellar systems have previously been utilized for various applications, including nanolithography based on gold-loaded micelles¹³, the deposition of gold nanocluster arrays for ZnO nanowire growth¹⁴ and protein binding¹⁵, and the synthesis of micellar nanoreactors for nanoparticles synthesis¹⁶. This chapter will demonstrate the feasibility of using gold nanocluster arrays synthesized via PS-*b*-P2VP micellar thin films as templates for printing DNA nanoarrays via SuNS. This chapter will also demonstrate the tunability of the gold nanocluster arrays synthesized via PS-*b*-P2VP micellar thin films and discuss possible routes for creating more complex DNA nanoarrays utilizing this tunability.

6.2 Experimental Section

6.2.1 Materials

Three PS-*b*-P2VP copolymers were used in this work, with molecular weights and nomenclatures as follows: PS-*b*-P2VP (81/21) [M_n (PS) = 81 000 g/mol, M_n (P2VP) =

21 000 g/mol, PDI = 1.16]; PS-*b*-P2VP (16/3.5) [M_n (PS) = 16 000 g/mol, M_n (P2VP) = 3 500 g/mol, PDI = 1.05]; and PS-*b*-P2VP (325/92) [M_n (PS) = 325 000 g/mol, M_n (P2VP) = 92 000 g/mol, PDI = 1.07]. The copolymers were used as received from Polymer Source, Inc. A homopolymer of polystyrene (PS) (M_n = 115 000 g/mol, PDI = 1.04) was used as received from Polymer Source, Inc. The following chemicals were also used as received: hydrogen tetrachloroaurate(III) trihydrate (HAuCl₄) obtained from Sigma-Aldrich Co. and toluene (HPLC grade, 99.8%) obtained from Sigma-Aldrich Co. All modified DNA strands were purchased from Integrated DNA Technologies. Hexyl thiol modified DNA strands (purchased as disulfides) were reduced before use.

The silicon nitride membrane window substrates were purchased from Structure Probe, Inc. Each substrate (surface area $\sim 4.5 \text{ mm}^2$) consisted of a 100-nm-thick amorphous, low-stress Si₃N₄ membrane supported on a 0.2-mm-thick silicon wafer that had been back-etched in the center to create the electron transparent Si₃N₄ window (surface area $\sim 0.2 \text{ mm}^2$). The use of the electron-transparent silicon nitride substrates allows for direct TEM characterization without disturbing the spin-cast films. Each substrate was rinsed with toluene prior to film casting. The substrates were clean silicon wafers (p-type, Silicon Quest International) coated with a 5 nm layer of Chromium deposited by electron beam evaporation in Temescal VES-2550 with a FDC-8000 Film Deposition Controller.

6.2.2 Sample Preparation

PS-*b*-P2VP was mixed with toluene at a concentration of 4 mg/mL and stirred until the polymer had dissolved within the solution. The P2VP micelle cores were then loaded with Au by adding HAuCl₄ to the micelle solution at a predetermined loading

ratio¹⁶. The loading ratio was defined as the number of AuCl_4^- ions relative to the number of pyridine rings within the toluene solution. In this work, loading ratios of 0.1, 0.35, and 1.0 were used. After the addition of HAuCl_4 , the solutions were mixed for 16 – 24 hours. Thin films were then created by spin casting the metal-loaded micellar solutions onto planar substrates at 6000 – 8000 rpm for 1 min at room temperature. The micellar thin film was then removed by oxygen plasma etching (rf plasma, 8 – 12 MHz) for 12 min, leaving only the gold nanocluster arrays remaining on the substrate. To increase the center-to-center spacing of the gold nanoclusters, PS homopolymer ($M_n = 115\,000$ g/mol) was added to the gold-loaded micellar solution to achieve a molar ratio of PS homopolymer to PS-*b*-P2VP equal to 20. To reduce the viscosities of these solutions to acceptable levels for spin casting, the solutions were diluted with toluene from 4 mg/mL toluene to 1 mg/mL toluene.

6.2.3 DNA Printing Procedure

Details about printing DNA via Supramolecular Nano-Stamping (SuNS) were described elsewhere^{9,10}. In brief, the gold nanocluster arrays were immersed into a solution of 5'-hexylthiol-modified DNA (4 μM in 1.0 M Potassium Phosphate buffer) for at least 72 hours. The substrates were then cleaned with water to minimize nonspecific adsorption of DNA. The substrates were then immersed in a solution of 5'-hexylthiol-modified complementary DNA (cDNA) (1 μM in 1.0 M NaCl in TE buffer) for 3 hours followed by rinsing in deionized water. A gold substrate was then quickly placed on the master substrate so that a meniscus would form between the two substrates. If necessary, a small mechanical force was applied to maximize contact between the substrates. The substrates were often observed to be bonded together after 5 – 10 hours. The bonded

substrates were then placed in an oven between 80 – 100 °C for 20 min. A 0.1 M NaCl/TE buffer solution kept at the oven temperature was added dropwise on the substrates within the oven until the substrates separated. The samples were then rinsed with water. A schematic of the SuNS process on gold nanoclusters is shown in Figure 6-1.

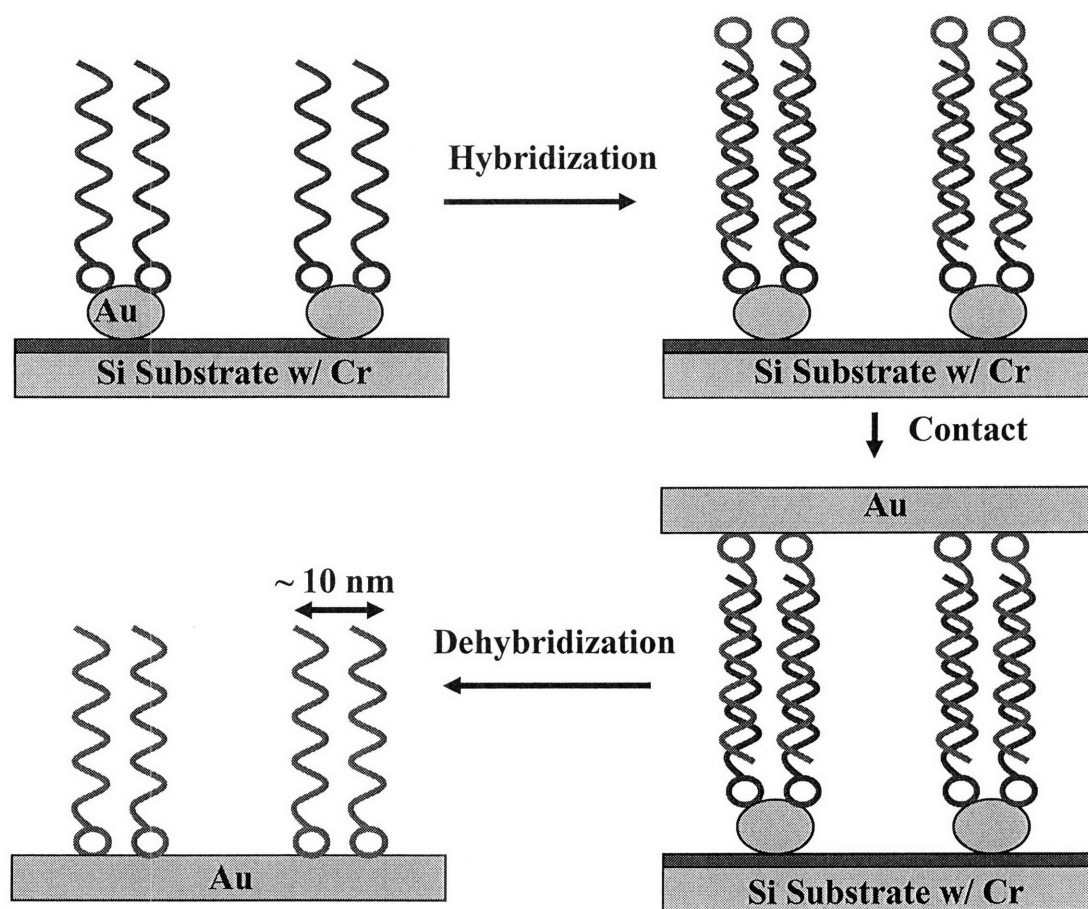


Figure 6-1. Diagram of DNA printing using block copolymer templated Au nanoclusters via SuNS.

6.3 Results and Discussion

Figure 6-2 shows a TEM image of a gold nanocluster array created from PS-*b*-P2VP (81/21) with a HAuCl₄ loading ratio of 0.35 after plasma etching on a Si₃N₄ substrate. As shown in previous chapters, the Si₃N₄ substrate offers a convenient route for analyzing the resulting inorganic nanocluster arrays using TEM. In this case, the gold nanoclusters had diameters of 8.6 ± 1.9 nm and center-to-center spacings of 95 ± 14 nm.

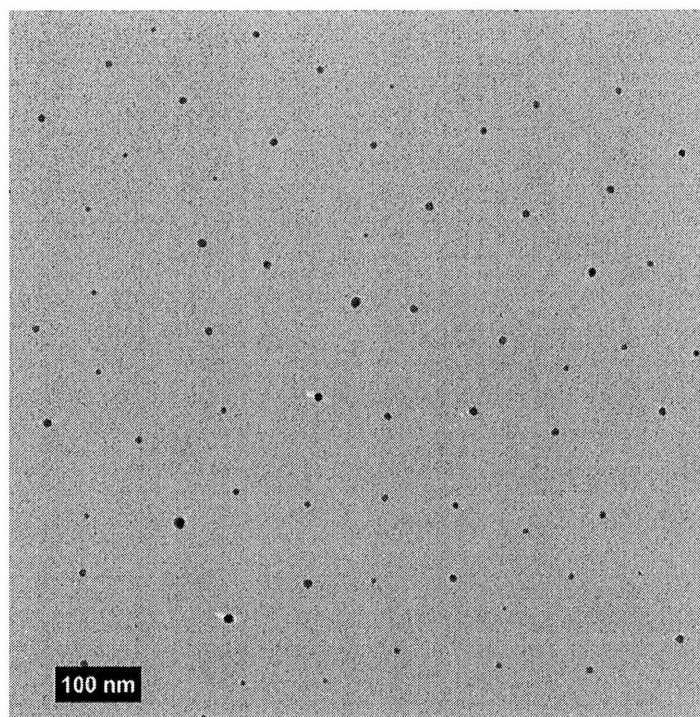


Figure 6-2. TEM image of a gold nanocluster array created from PS-*b*-P2VP (81/21) with a gold loading ratio of 0.35.

While Si₃N₄ substrates were useful for nanocluster characterization, Si was the initial substrate chosen for creating DNA nanoarrays. After synthesizing the gold nanoclusters on Si using the standard procedure, the Si substrates were immersed into a solution of 5'-hexylthiol-modified DNA for at least 72 hours. AFM characterization of

the Si substrates after this step demonstrated that very few of the gold nanoclusters remained on the Si substrates. It is believed that the gold nanoclusters dissociated from the substrate during this step due to the lack of strong interactions between the gold and Si. To increase the interactions between the gold nanoclusters and the surface, a 5 nm Chromium layer was deposited onto a Si substrate¹⁷. The standard synthesis procedure was then utilized to create a gold nanocluster array. In the next step, the Cr-coated substrate containing gold nanoclusters was immersed in the 5'-hexylthiol-modified DNA solution, and subsequently immersed in the 5'-hexylthiol-modified cDNA solution. The resulting AFM image is shown in Figure 6-3a. The results demonstrate that the Cr layer prevented a significant portion of the previously observed dissociation of gold nanoclusters from the Si substrate surface.

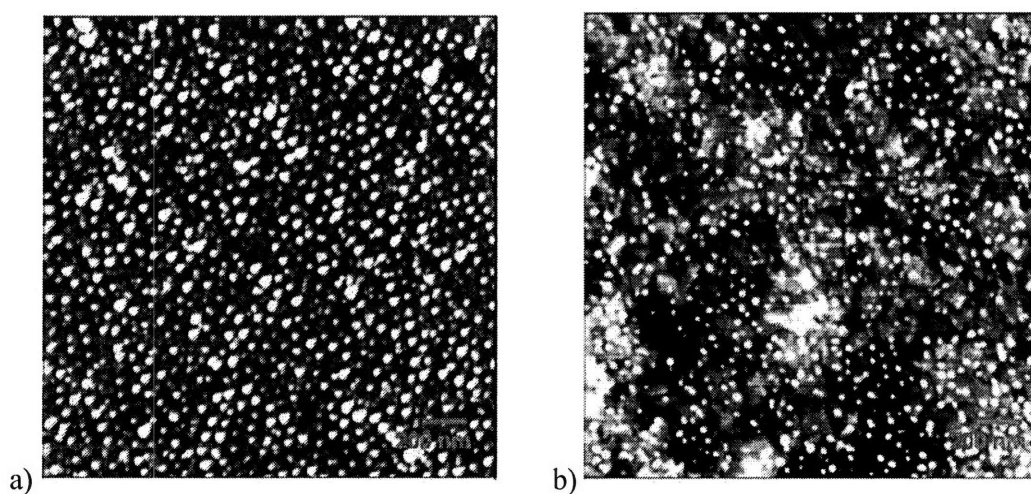


Figure 6-3. AFM height image of: a) DNA hybridized gold nanoclusters made from PS-*b*-P2VP (81/21) on a Cr-coated Si substrate (height scale = 20 nm), and b) printed DNA strands on a gold substrate following dehybridization (height scale = 5 nm).

The substrate in Figure 6-3a was then brought into contact with a gold substrate for 5 – 10 hours. The two substrates were then placed in an oven to dehybridize the DNA.

After removing the substrates from the oven, an AFM image of the resulting DNA-printed gold substrate is shown in Figure 6-3b. The image shows that features of similar size to the original gold nanoclusters have been transferred to the new substrate. The height of the features in Figure 6-3a and 6-3b decreased from 20 nm to 5 nm, which was expected because gold nanoclusters are no longer on the substrate in Figure 6-3b.

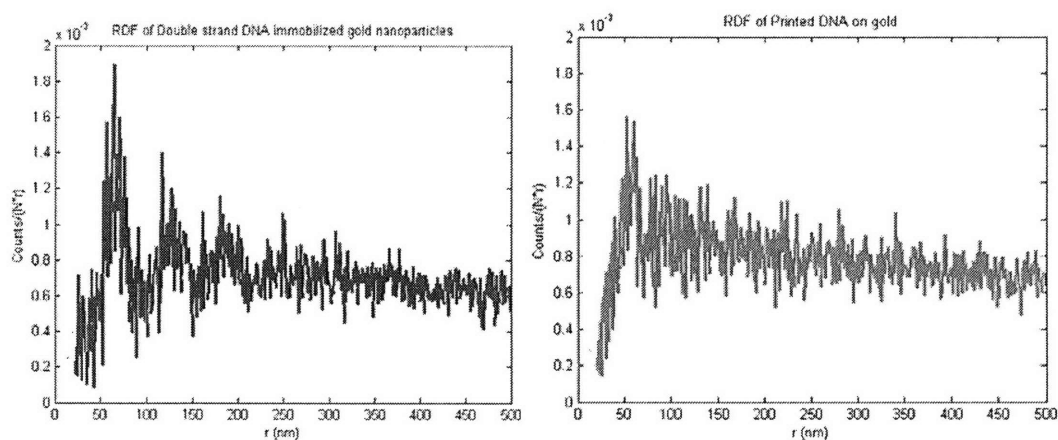


Figure 6-4. Radial distribution function of DNA hybridized gold nanoclusters on a Cr-coated Si substrate (left image) and printed DNA strands on a gold substrate following dehybridization (right image).

The graphs in Figure 6-4 show the radial distribution functions (RDF) for the AFM images in Figure 6-3a and 6-3b, respectively. By comparing the two images, it appears that the first order peak is consistent for the two samples, but the printed DNA strands don't maintain the longer range order that is characteristic of the higher order peaks.

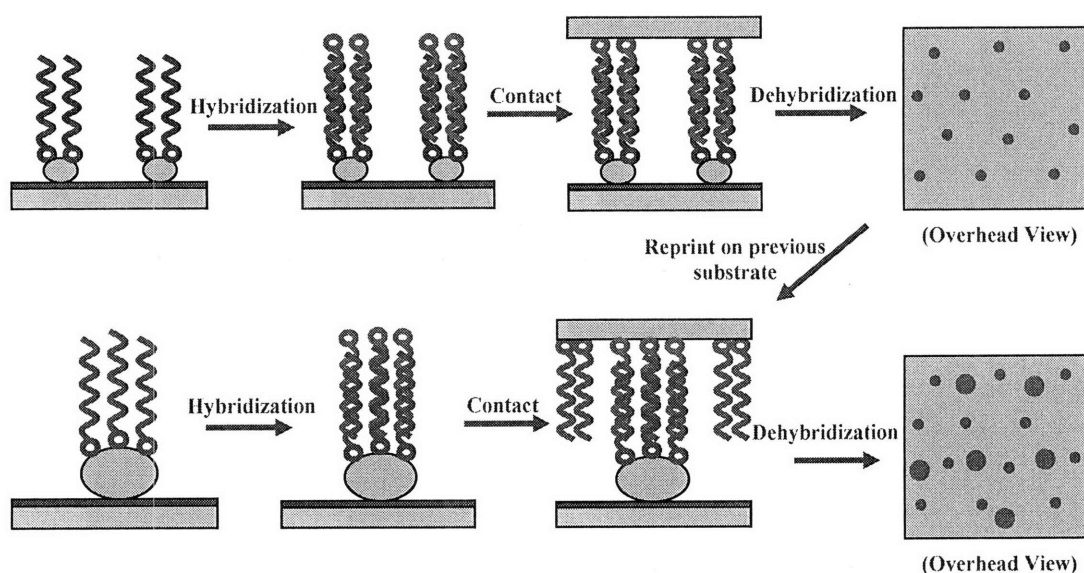


Figure 6-5. Diagram of a possible route for synthesizing more complex DNA nanoarrays using block copolymer templated gold nanocluster arrays.

The value of using PS-*b*-P2VP templated gold nanocluster arrays in DNA printing is derived from the tunability of the micellar thin film system. A possible route for using this tunability to create more complex DNA nanoarrays is shown in Figure 6-5. The top line of the diagram shows the standard printing procedure shown in Figure 6-1, along with a typical overhead view of the DNA-printed substrate. The bottom line of Figure 6-5 shows using a gold nanocluster array with larger diameters and larger center-to-center spacings to print a second DNA strand onto the original substrate. This route would lead to a substrate with different size spots of different DNA species and could allow for more advanced analysis applications.

In order to achieve more complex DNA nanoarrays, control of the size and spacing of the gold nanocluster arrays must be achieved. As was demonstrated in previous chapters, block copolymer micellar thin films offer considerable opportunities for tuning the properties via variation of the block copolymer molecular weight, the

variation of the metal loading ratio, and the addition of PS homopolymer. Figure 6-6 demonstrates the effects of varying the gold loading ratio from 0.1 to 1.0 using the PS-*b*-P2VP (325/92) micellar system. In Figure 6-6a, the loading ratio of 0.1 leads to gold nanoclusters that have diameters of 5.3 ± 0.3 nm with a center-to-center spacing of 170 ± 30 nm. By increasing the gold loading ratio to 0.35 (Figure 6-6b), the gold nanoclusters increase in diameter to 9.2 ± 0.6 nm, while the center-to-center spacing decreases to 145 ± 23 nm. An additional increase in the gold loading to 1.0 (Figure 6-6c) causes the gold nanoclusters to increase to 16.3 ± 1.3 nm in diameter, while the center-to-center spacing decreases to 107 ± 18 nm. Through variation of the gold loading ratio, the diameter was increased by a factor of three. Interestingly, the center-to-center spacing of the arrays decreased as the gold loading ratio increased. This could only occur if the aggregation number of the micelles decreased as the metal loading ratio increased, although the explanation for why this occurs is still unclear.

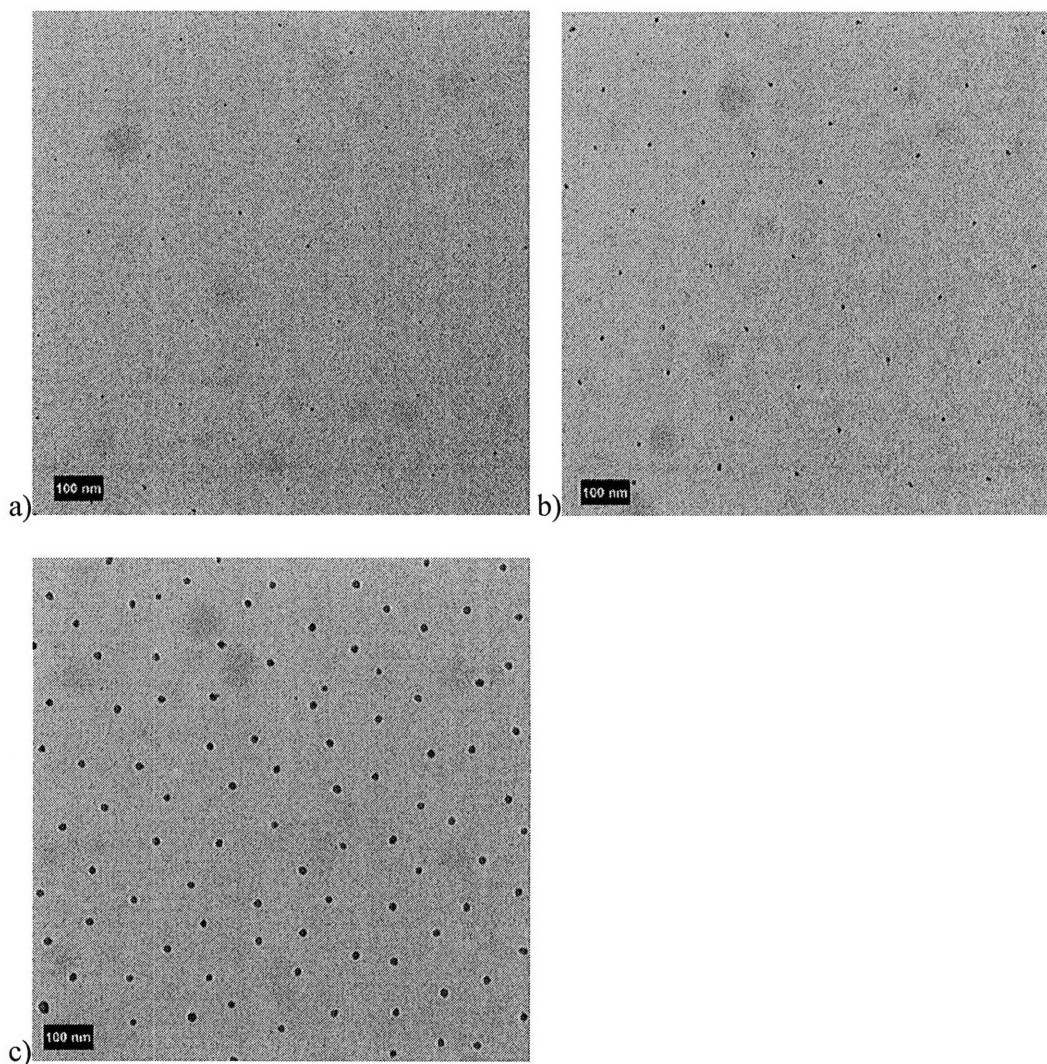


Figure 6-6. TEM images of gold nanocluster arrays created from PS-*b*-P2VP (325/92) with a gold loading ratio of: a) 0.1, b) 0.35, and c) 1.0. Scale bars = 100 nm.

Figure 6-7 demonstrates the effect of varying the molecular weight of PS-*b*-P2VP while maintaining a constant gold loading ratio of 0.35. In Figure 6-7a, the PS-*b*-P2VP (16/3.5) system leads to gold nanoclusters with diameters of 2.8 ± 0.7 nm and a center-to-center spacing of 36 ± 6 nm. The PS-*b*-P2VP (81/21) system shown in Figure 6-7b leads to gold nanoclusters with diameters of 8.6 ± 1.9 nm and a center-to-center spacing of 95 ± 14 nm. The PS-*b*-P2VP (325/92) system shown in Figure 6-7c leads to gold

nanoclusters with diameters of 9.2 ± 0.6 nm with a center-to-center spacing of 145 ± 23 nm. The variation of the PS-*b*-P2VP molecular weight led to significant variation in the center-to-center spacing of the nanocluster arrays, but the diameters of the nanoclusters were less affected. This is most obviously observed in comparing the PS-*b*-P2VP (81/21) system with the PS-*b*-P2VP (325/92) system. A fourfold increase in the PS block length led to a 50% increase in the center-to-center spacing of the nanocluster arrays; however, a similar fourfold increase in the P2VP block length led to an increase in the diameter of less than 10%.

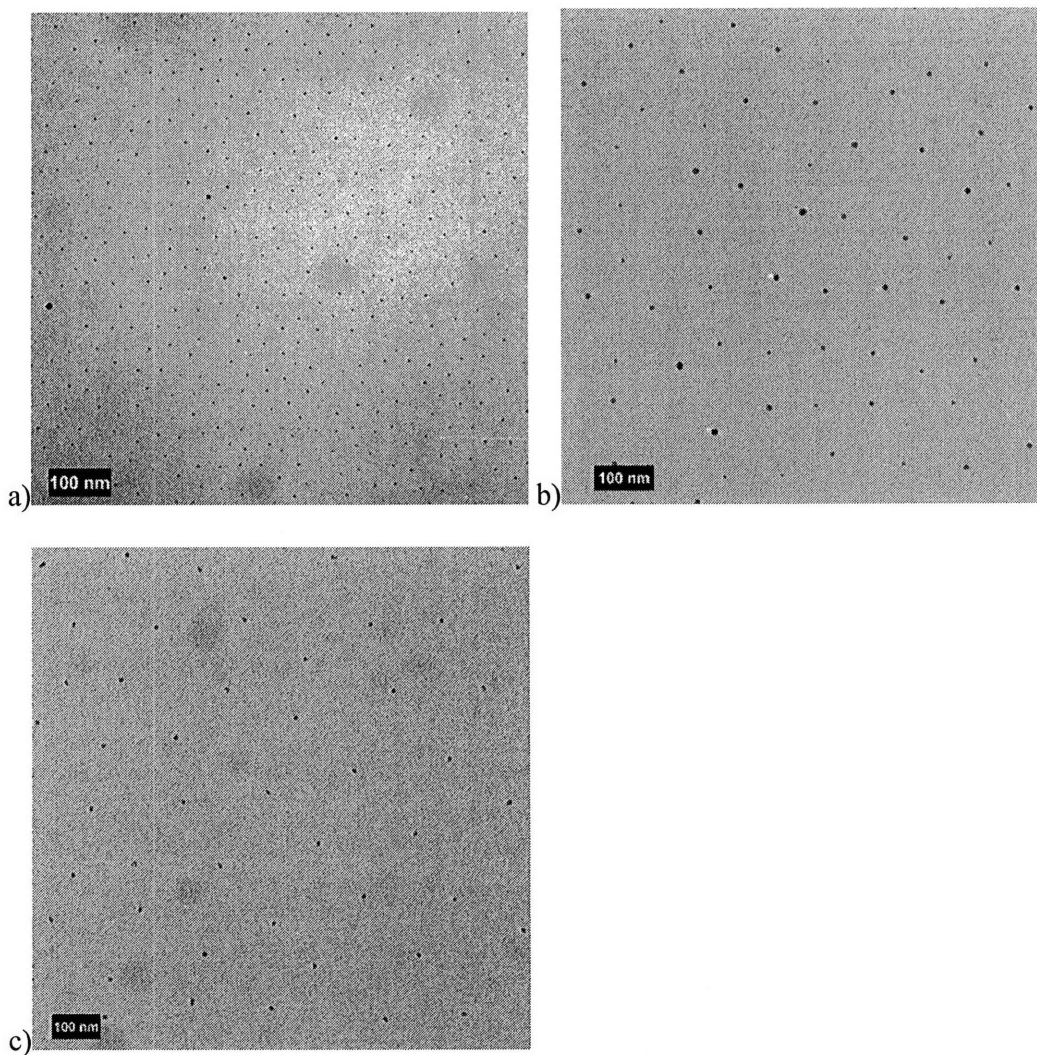


Figure 6-7. TEM images of gold nanocluster arrays created from: a) PS-*b*-P2VP (16/3.5), b) PS-*b*-P2VP (81/21), and c) PS-*b*-P2VP (325/92) with a gold loading ratio of 0.35. Scale bars = 100 nm.

Figure 6-8 demonstrates the ability to control the areal density of the gold nanoclusters through the addition of PS homopolymer into the micellar solution. Figure 6-8a shows a TEM image of a gold nanocluster array synthesized from PS-*b*-P2VP (325/92) with a gold loading ratio of 0.35 and no PS homopolymer added. The gold nanoclusters in this image have an areal density of $3 \times 10^9 \text{ cm}^{-2}$ and a center-to-center spacing of $170 \pm 30 \text{ nm}$. Figure 6-8b shows a TEM image of a gold nanocluster array synthesized from PS-*b*-P2VP (325/92) with a gold loading ratio of 0.35 and a PS homopolymer loading ratio of 20:1 (where the PS homopolymer loading ratio is defined as the molar ratio of PS homopolymer to PS-*b*-P2VP block copolymer [PS: PS-*b*-P2VP]). After the addition of PS homopolymer, the gold nanoclusters have an areal density of $1.5 \times 10^9 \text{ cm}^{-2}$ and a center-to-center spacing of $275 \pm 60 \text{ nm}$. The unique feature of the addition of PS homopolymer into the block copolymer micellar system is the ability to vary the areal density of the resulting nanocluster arrays while maintaining a constant diameter.

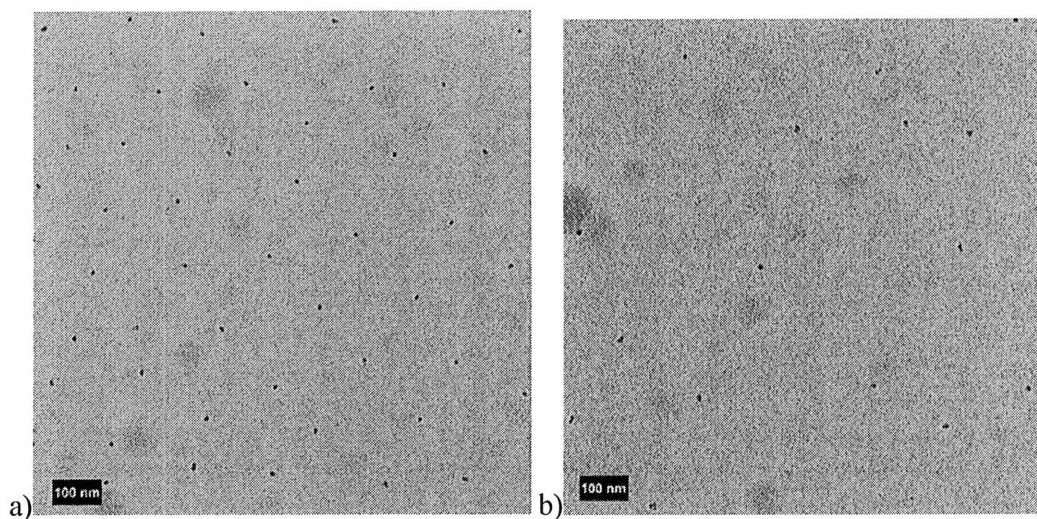


Figure 6-8. TEM images of gold nanocluster arrays created from PS-*b*-P2VP (325/92) with a gold loading ratio of 0.35 and a PS homopolymer ($M_n = 115k$) loading ratio of: a) No homopolymer added, and b) 20:1 [PS: PS-*b*-P2VP]. Scale bars = 100 nm.

To demonstrate the possible variation of the printed DNA nanoarrays using the tunability of the micellar thin film system, gold nanocluster arrays synthesized from PS-*b*-P2VP (325/92) were used to create DNA nanoarrays. Figure 6-9a shows the AFM image of the gold nanoclusters on a Cr-coated Si substrate after having been immersed in a solution of 5'-hexylthiol-modified ss-DNA for 72 hours. Figure 6-9b shows the printed DNA strands on a gold substrate after completing the contacting and dehybridization steps. By comparing Figures 6-3 and 6-9, it is clear that the PS-*b*-P2VP (325/92) system led to printed DNA nanoarrays with a larger center-to-center spacing compared to the PS-*b*-P2VP (81/21) system.

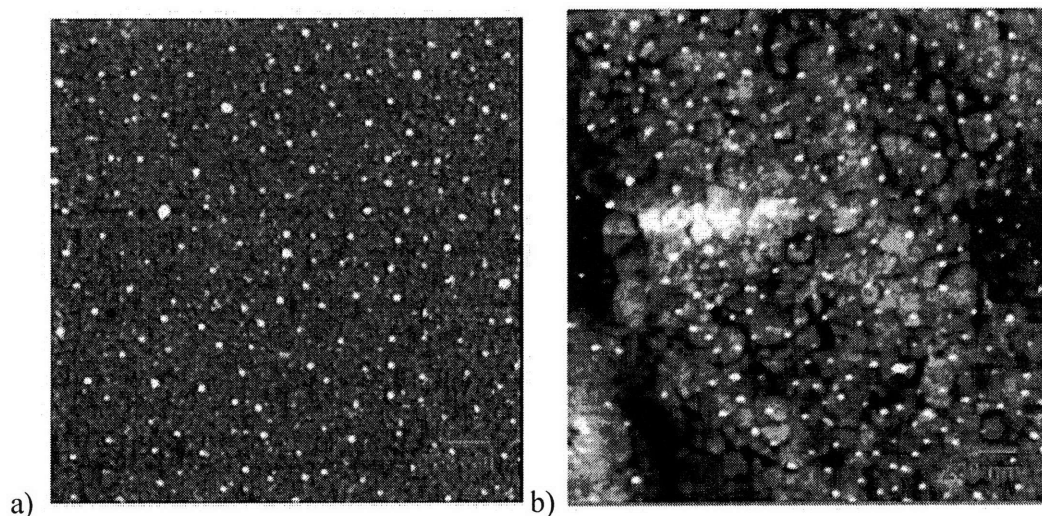


Figure 6-9. AFM height image of: a) ssDNA-hybridized gold nanoclusters on a Cr-coated Si substrate (height scale = 20 nm), and b) printed DNA strands on a gold substrate following dehybridization (height scale = 7 nm).

As demonstrated in Figure 6-5, differentiation of the gold nanoclusters via size or morphology variation could lead to the ability to create more complex analysis devices. In Figure 6-5, variation of the diameter of the nanoclusters was illustrated as one possible route to achieve nanocluster differentiation. Another possible route involves varying the morphology of the nanoclusters through the addition of a second solvent into the micellar solution prior to spin casting. Figure 6-10a shows a typical TEM image of a gold nanocluster arrays created from PS-*b*-P2VP (81/21) with a gold loading ratio of 0.35. Figure 6-10b shows the TEM image of a gold nanocluster array created from PS-*b*-P2VP (81/21) with a gold loading ratio of 0.35 and a H₂O loading ratio (defined as the molar ratio of H₂O to pyridine rings in solution) of 100:1. In the higher magnification image shown in Figure 6-10b, it was observed that the morphology of the gold nanoclusters was clearly altered due to the addition of H₂O, which sequesters within the interior of the

micelles. This could lead to another possible route for differentiating gold nanoclusters in more complex analysis applications.

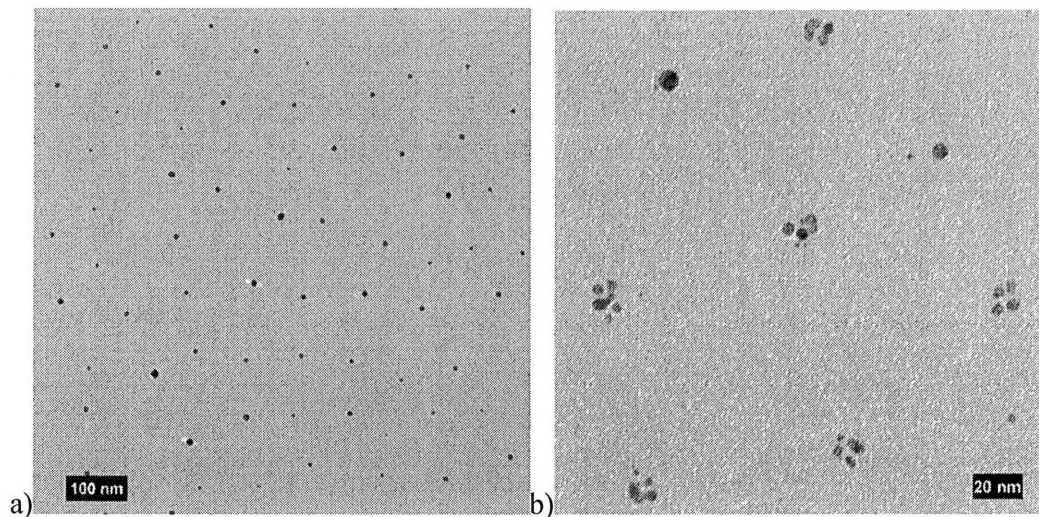


Figure 6-10. TEM images of gold nanocluster arrays created from PS-*b*-P2VP (81/21) with a gold loading ratio of 0.35 and H₂O loading ratio (number of H₂O molecules relative to the number of pyridine rings) of: a) No H₂O added, and b) 100:1.

6.4 Conclusions

This chapter demonstrated the feasibility of using gold nanocluster arrays templated from PS-*b*-P2VP micellar thin films as substrates for synthesizing printed DNA nanoarrays via the SuNS procedure. Initially the capability of creating gold nanoclusters arrays using PS-*b*-P2VP micellar thin films was demonstrated via TEM characterization. The gold nanocluster arrays were then used in the SuNS procedure to synthesize DNA printed gold substrates that were characterized using AFM. Experiments showed that a 5 nm Chromium layer evaporated onto the original Si substrate was necessary to prevent the dissociation of the gold nanoclusters from the Si substrate in the DNA solutions. Routes for creating more complex DNA nanoarrays that take advantage

of the tunability of the block copolymer micellar thin film template were also discussed. The methods for tuning the gold nanocluster arrays, such as the variation of the block copolymer molecular weight, the variation of the gold loading ratio, and the addition of PS homopolymer, were also demonstrated by TEM characterization.

6.5 References

1. Lockhart, D. J.; Dong, H.; Byrne, M. C.; Follettie, M. T.; Gallo, M. V.; Chee, M. S.; Mittmann, M.; Wang, C.; Kobayashi, M.; Horton, H.; Brown, E. L. *Nature Biotechnology* **1996**, *14*, 1675 – 1680.
2. Hacia, J. G.; Brody, L. C.; Chee, M. S.; Fodor, S. P.; Collins, F. S. *Nature Genetics* **1996**, *14*, 441 – 447.
3. Golub, T. R.; Slonim, D. K.; Tamayo, P.; Huard, C.; Gaasenbeek, M.; Mesirov, J. P.; Coller, H.; Loh, M. L.; Downing, J. R.; Caligiuri, M. A.; Bloomfield, C. D.; Lander, E. S. *Science* **1999**, *286*, 531 – 537.
4. Stegmaier, K.; Ross, K. N.; Colavito, S. A.; O'Malley, S.; Stockwell, B. R.; Golub, T. R. *Nature Genetics* **2004**, *36*, 257 – 263.
5. Pirrung, M. C. *Chemical Review* **1997**, *97*, 473 – 488.
6. Pirrung, M. C. *Angewandte Chemie, International Edition* **2002**, *41*, 1276 – 1289.
7. Lombardi, S. *PharmaGenomics* **2004**, *4*, S25.
8. Okamoto, T.; Suzuki, T.; Yamamoto, N. *Nature Biotechnology* **2000**, *18*, 438 – 441.
9. Yu, A. A.; Savas, T. A.; Taylor, G. S.; Guiseppe-Elie, A.; Smith, H. I.; Stellacci, F. *Nano Letters* **2005**, *5*, 1061 – 1064.
10. Yu, A. A.; Savas, T. A.; Cabrini, S.; diFabrizio, E.; Smith, H. I.; Stellacci, F. *Journal of the American Chemical Society* **2005**, *127*, 16774 – 16775.
11. Lin, H.; Sun, L.; Crooks, R. M. *Journal of the American Chemical Society* **2005**, *127*, 11210 – 11211.

12. Lin, H.; Kim, J.; Sun, L.; Crooks, R. M. *Journal of the American Chemical Society* **2006**, *128*, 3268 – 3272.
13. Spatz, J. P.; Herzog, T.; Mossmer, S.; Ziemann, P.; Moller, M. *Advanced Materials* **1999**, *11*, 149 – 153.
14. Haupt, M.; Ladenburger, A.; Sauer, R.; Thonke, K.; Glass, R.; Roos, W.; Spatz, J. P.; Rauscher, H.; Riethmuller, S.; Moller, M. *Journal of Applied Physics* **2003**, *93*, 6252 – 6257.
15. Spatz, J. P.; Mossmer, S.; Hartmann, C.; Moller, M.; Herzog, T.; Krieger, M.; Boyen, H. G.; Ziemann, P.; Kabius, B. *Langmuir* **2000**, *16*, 407 – 415.
16. Kastle, G.; Boyen, H. G.; Weigl, F.; Lengl, G.; Herzog, T.; Ziemann, P.; Riethmuller, S.; Mayer, O.; Hartmann, C.; Spatz, J. P.; Moller, M.; Ozawa, M.; Banhart, F.; Garnier, M. G.; Oelhafen, P. *Advanced Functional Materials* **2003**, *13*, 853 – 861.
17. Hoogvliet, J. C.; Bennekom, W. P. *Electrochimica Acta* **2001**, *47*, 599 – 611.

Chapter 7 Conclusions

7.1 Summary of Thesis Contributions

The work presented in this thesis demonstrated that block copolymer micellar thin films can be utilized as templates to synthesize tunable and patternable inorganic nanocluster arrays. The work further demonstrated that these tunable nanocluster arrays can be exploited in a variety of applications, including creating catalysts for chemical vapor deposition (CVD) growth of carbon nanotubes (CNTs) and as templates for synthesizing DNA nanoarrays using Supramolecular Nano-Stamping (SuNS).

The work presented in Chapter 2 demonstrated that a block copolymer micellar template could be used to create large-scale arrays of iron oxide nanoclusters capable of catalyzing carbon nanotube growth. This was not a trivial task because of the distinct possibility that the degraded polymer film would coat the underlying metal nanoparticle, thereby deactivating the catalyst particle. The successful growth allowed this work to be one of the first results demonstrating the production of CNT catalysts via block copolymer templating. In this chapter a unique ability to characterize the as-grown CNTs and the iron oxide nanoclusters directly on the catalyst substrate was demonstrated by utilizing Si_3N_4 window grids. This led to the interesting observation that the agglomeration of iron oxide nanoclusters at high CNT growth temperatures led to CNT diameters that were larger than the initial iron oxide nanocluster diameters.

The work presented in Chapter 3 demonstrated the tunability of inorganic nanocluster arrays created from block copolymer micellar thin films. This work demonstrated the ability to control the diameter and the areal density of the inorganic nanoparticles through the straight-forward approach of varying the molecular weight of the block copolymer, as well as by the two novel approaches of adding polystyrene homopolymer and mixing different micellar solutions. This work also presented a route for creating mixed species inorganic nanoparticles via the mixing of different micellar solutions.

The work in Chapter 4 set out to combine the catalytic abilities of the iron oxide nanoclusters arrays with the tunability demonstrated in Chapter 3. The initial section focused on optimizing the CNT growth protocol to improve the catalytic activity of the inorganic nanoparticle arrays. This led to vertical growth of CNTs from the substrate surface, which was the first demonstration of vertical CNT growth from a catalyst synthesized via a block copolymer system. These CNT thin films could have possible applications in nanoelectronics, heat dissipation, and composites. This work also utilized the capability of tuning the diameters of the nanoparticles to reinforce the notion that optimal growth conditions occur at different conditions for different sizes of catalyst particles. This work also demonstrated that the morphology of a CNT thin film could be manipulated from a thick vertical growth of CNTs to a sparse and tangled arrangement of individual nanotubes through variation of the areal density of the nanoparticle catalyst arrays. The development of this catalyst system is noteworthy because of the unique ability to control the catalyst properties relative to traditional CNT catalyst systems.

The work in Chapter 5 demonstrated the ability to pattern inorganic nanoclusters created by block copolymer micellar thin films on the micron length scale via microcontact printing (μ CP). In this chapter, the block copolymer micellar thin films are printed into patterns of various shapes and sizes to demonstrate the versatility of this μ CP approach. The patterned nanoparticle arrays were then used as catalysts to synthesize patterned CNT structures that maintained the fidelity of the pattern to form high aspect-ratio standing structures. This procedure could be very useful in the development of CNT devices using this block copolymer catalyst system in the future.

Finally, Chapter 6 provides a demonstration of the generality of the block copolymer micellar approach by creating gold nanoparticle arrays for use in synthesizing DNA arrays for sensing applications. This work initially verified that tunable gold nanocluster arrays can be synthesized from micellar thin films of PS-*b*-P2VP; subsequently, the ability to print thiol-terminated DNA molecules with a spacing of tens of nanometers via SuNS onto a gold substrate was demonstrated. These DNA arrays could have useful applications in creating low cost DNA diagnostic tools for detecting certain forms of cancer and predicting the likelihood of certain genetic diseases.

7.2 Recommendations for Future Work

There are a variety of interesting topics from this thesis that could be pursued further. A discussion of the possibilities for future work is included in the following paragraphs.

The first general area for future work focuses on the use of different species of block copolymers. In this research, all of the work was done using only two varieties of

block copolymers, PS-*b*-PAA and PS-*b*-P2VP. This work found that in certain cases, such as the synthesis of Au nanoparticles, PS-*b*-P2VP was considerably more effective than PS-*b*-PAA. Considering the large number of possible inorganic species that could be used in these systems and their different affinities to specific block copolymer segments, future research in block copolymer micellar thin film arrays would be well served by attempting to utilize the large number of possible block copolymer species commercially available.

This thesis focused exclusively on the formation of spherical micelles in order to create spherical inorganic nanoclusters. It would be interesting to investigate the feasibility of using block copolymer micelles of different assemblies (cylinders, vesicles) to create inorganic features on substrates. By using cylindrical micelles, the creation of inorganic nanowires might be relatively straightforward. As evidenced from Boontongkong's work [*Macromolecules* **2002**, 35, 3647] on PS-*b*-PAA, these cylinders will likely form overlapping structures; however, through gentle solvent or thermal annealing aligned inorganic nanowires might be possible.

In Chapter 3 of this thesis, we discussed the ability to create multi-species inorganic nanoclusters through the mixing of micellar solutions. It might be interesting to more thoroughly study the mixing of micellar solutions and the resulting inorganic nanoclusters. In this work, only two metal species (FeCl₃ and PbAc₂) were used in these experiments. It would be intriguing to study the effects of using different pairs of metal salts in these mixing experiments. Other possible studies include: mixing solutions with different metal loading ratios (as opposed to the identical loading ratios used in this work), mixing solutions of different polymers (e.g. PS-*b*-PAA loaded with FeCl₃ mixed

with PS-*b*-P2VP loaded with H₂AuCl₄), mixing three solutions loaded with different metal salts, and the simultaneous loading of two different metal species into one polymer solution. Another interesting idea would be to allow longer mixing times to determine if the system had truly equilibrated, because in this work the mixed solutions only equilibrated for 120 hrs.

In Chapter 4 of this thesis, the optimization of the MWCNT growth by varying the reactor growth conditions focused on using the 16 nm iron oxide nanoclusters. It would be interesting to do a systematic study of the optimal growth conditions for a variety of iron oxide nanoclusters with different diameters. This could lead to interesting insights as to why the optimal growth conditions change as a function of the catalyst diameter. For certain conditions that yielded vertical growth of CNTs, the catalyst efficiency could be calculated using the quantifiable areal density of the iron oxide nanoclusters and used to compare different growth conditions. Another interesting possibility would be to combine the ability to create mixed metal nanocluster arrays via micelle solution mixing with CNT growth to determine the effect of multi-species nanoclusters. Some possible candidates to combine with Fe include Mo and Al, which have been shown to improve iron oxide catalyst activity.

The work in this thesis focused on the applications of iron-loaded and gold-loaded micellar thin films. There are many other interesting applications that could be investigated by loading different metal species. This includes the synthesis of solid lubricant nanoclusters such as molybdenum disulfide and the creation of other catalytic species such as platinum, molybdenum, and titanium, for inorganic nanowire growth.

This thesis relied almost entirely on spin-casting as a route to create the block copolymer micellar thin films needed for inorganic nanocluster synthesis. Although spin casting has been an effective technique, it would be useful to also consider using dip-casting as a route for creating uniform micellar thin films. This technique was utilized by Kastle *et al* [*Adv Func Mater* 2003, 13, 853] to create uniform thin films, although work during this thesis using a suboptimal experimental setup was unable to replicate those results.

Appendix A Characterization of Carbon Nanotube Thin Films Synthesized from Block Copolymer Micellar Thin Film Catalysts using Small Angle X-Ray Scattering*

Carbon nanotube films have shown great promise for use in a wide variety of applications, including membranes, heat dissipation, nanoelectronics, and superhydrophic surfaces¹⁻⁶. In all of these proposed applications, it is important to understand the bulk morphology of the CNT thin films. Traditionally this has been accomplished through transmission electron microscopy (TEM) and scanning electron microscopy (SEM). TEM characterization allows for resolution of the CNT diameter down to the angstrom level, but it is inherently a local measurement. Another disadvantage of TEM is the inability to image the as-grown CNT thin film, thereby preventing characterization of different regions of the CNT thin film. SEM provides characterization on a larger length scale, but the resolution of CNT diameters is exceedingly difficult and quantification of CNT alignment requires subjective image analysis.

In this appendix, small angle x-ray scattering (SAXS) was used to characterize both the CNT diameters as well as the orientation of the CNTs within the thin film. The value of SAXS as a CNT characterization tool is due to the fact that millions of CNTs are sampled to give a “locally averaged” measurement. In previous work SAXS has been used to study single-wall CNT bundles⁷⁻⁸, the effect of sonication on CNT bundles⁹⁻¹⁰, and to determine CNT diameters¹¹⁻¹².

The setup for the SAXS characterization of the CNTs thin films is shown below in Figure A-1. The x-rays were passed edge-on (along the z axis) through the CNT thin film.

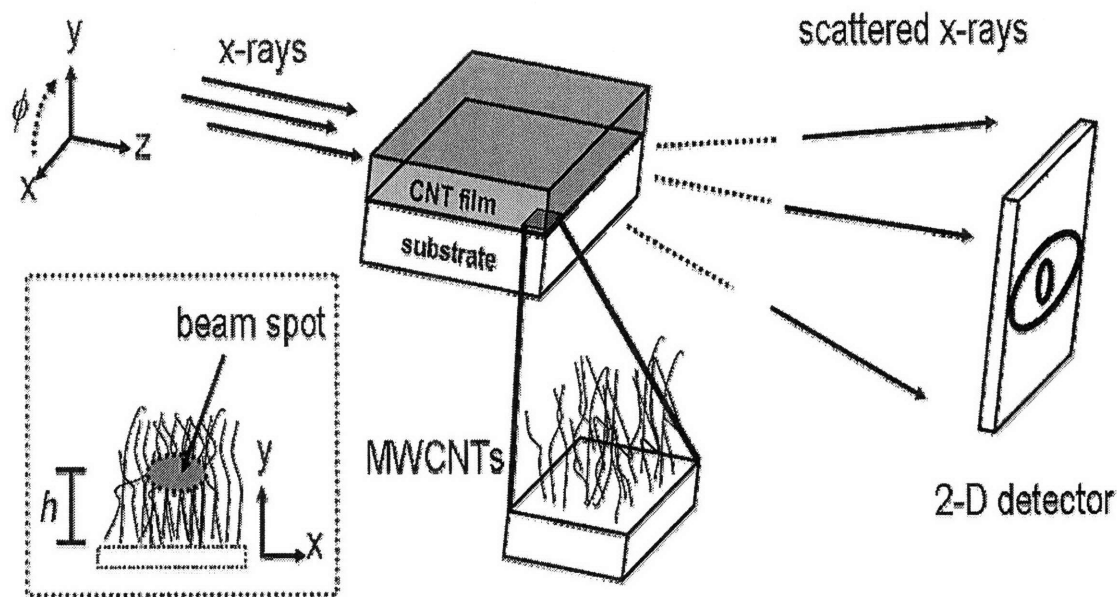


Figure A-1. Diagram of the experimental setup for analyzing CNT thin films using SAXS characterization.

In this work two different CNT thin films were synthesized using different catalyst systems and characterized using SAXS. Sample 1 consisted of a 1.5 millimeter tall film of MWCNTs grown by thermal CVD of ethylene at 750 degrees Celsius, using a catalyst film of Al_2O_3 and Fe (10/1.2 nm thickness, respectively) supported on a Si substrate. Sample 2 was a 0.5 millimeter tall film of MWCNTs grown by thermal CVD of ethylene at 750 degrees Celsius, using catalytic iron oxide nanocluster arrays that were templated by a PS-*b*-PAA micellar film onto an Al_2O_3 -coated Si substrate. SAXS data was then collected for each of the substrates at various values of h , where $h = 0$ corresponds to the substrate surface. Figure A-2 and A-3 contain azimuthally integrated

SAXS intensities versus scattering vector q extracted from the 2-D SAXS images for Sample 1 and 2, respectively; the intensities were obtained for conical slices around 180 ± 10 degrees. In this notation $\phi = 0$ deg corresponds to the x-axis and increases in a counter-clockwise rotation.

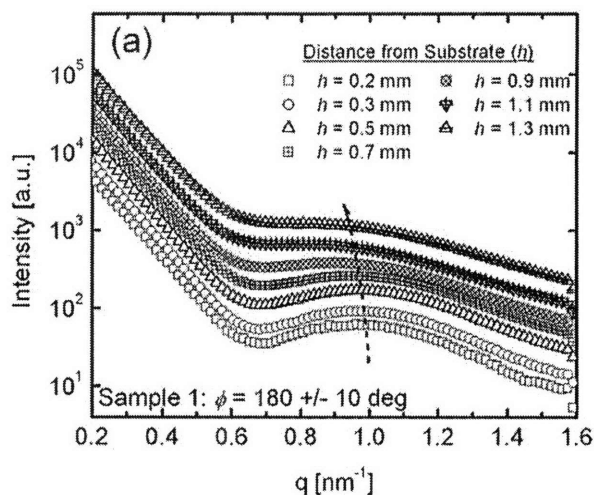


Figure A-2. SAXS intensities as a function of scattering vector for Sample 1 obtained by integrating over ± 10 degree conical slices around $\phi = 180$ deg.

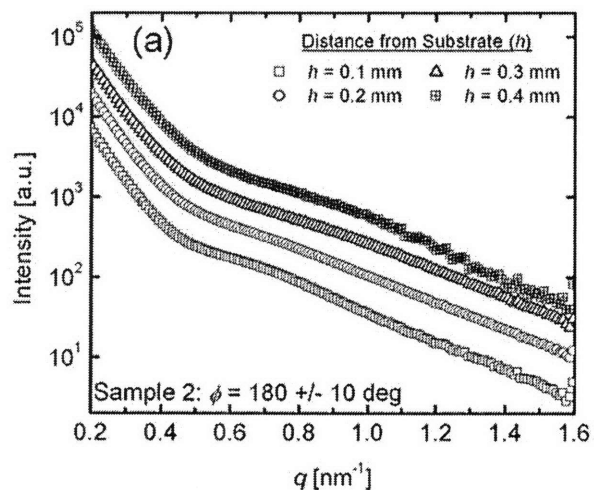


Figure A-3. SAXS intensities as a function of scattering vector for Sample 2 obtained by integrating over ± 10 degree conical slices around $\phi = 180$ deg.

The SAXS intensities for Sample 1 shown in Figure A-2 show a feature in the range of $q \sim 1.0$ that corresponds to the characteristic outer diameter of the CNTs. As h is increased, the peak shifts to smaller q values, suggesting that the CNT diameter is larger at the top of the CNT thin film. The SAXS intensities for Sample 2 shown in Figure A-3 show a more diffuse peak in the range of $q \sim 0.6 - 0.8$. The broadening of the peak is likely caused by the increase in polydispersity of CNT diameters in Sample 2 as h is increased.

The CNT diameters can be extracted from the SAXS data by defining the intensity as a combination of the intra-particle form factor and the inter-particle structure factor. The results are shown in Figure A-4. For Sample 1, it is clear that the CNT diameter increases by approximately 10% from the bottom to the top of the thin film. The same trend is observed for the CNT diameter in Sample 2. In both cases, the CNT diameters determined from SAXS match very closely with the CNT diameters determined using TEM.

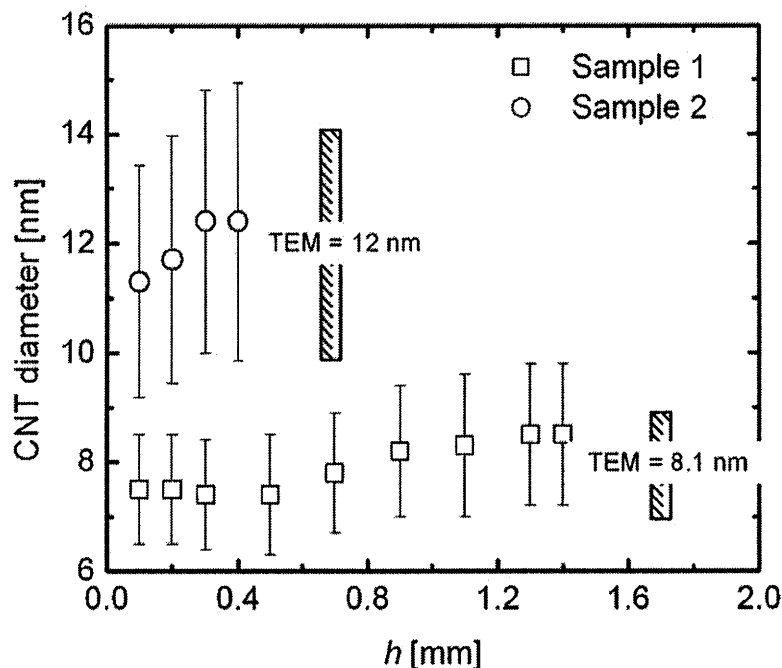


Figure A-4. Summary of the mean and standard deviation of CNT diameters at varying distances above the substrate (h) as measured by SAXS and compared against TEM measurements.

The orientation of the CNT thin films can be quantified by calculating the Hermans' orientation parameter. The limiting values of $f = 1$, $f = 0$, and $f = -1/2$ correspond to perfect vertical alignment, random orientation, and perfect horizontal alignment, respectively. Figure A-5 plots the Hermans' orientation parameter (f) as a function of distance from the substrate for Sample 1 and 2. It is clear that Sample 1 shows considerably more alignment than Sample 2, which appears to show only slight vertical alignment. In particular, Sample 1 shows a significant increase in the vertical alignment of the CNTs in the middle of the thin film, but lower orientation at the bottom and top of the film. To confirm these results, SEM was used to characterize the different regions of the film. The resulting SEM images are shown in Figure A-6. Figure A-6 shows SEM

images from the: a) bottom, b) middle, c) top of the CNT thin film for Sample 1 as well as an SEM image of representative of the entire thin film for Sample 2. Clearly Figure A-6b) shows more vertical alignment than Figure A-6a) and Figure A-6c), confirming the SAXS results. By comparing the SEM micrographs for Sample 1 and 2, it is also clear that Sample 1 has significantly more vertical alignment than Sample 2, as demonstrated using SAXS characterization.

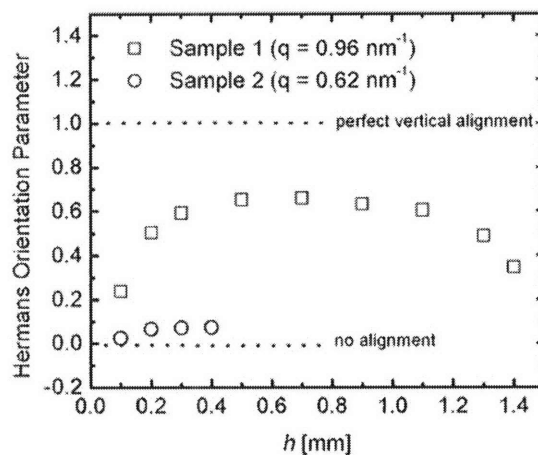
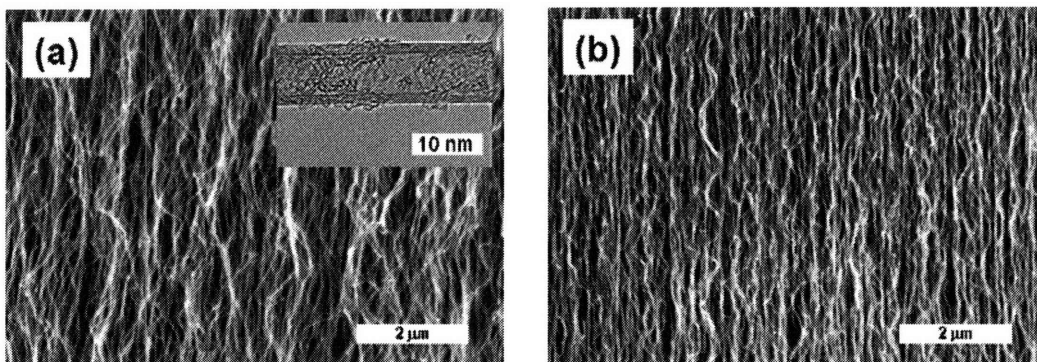


Figure A-5. Hermans' orientation parameter (f) as a function of distance from substrate (h).



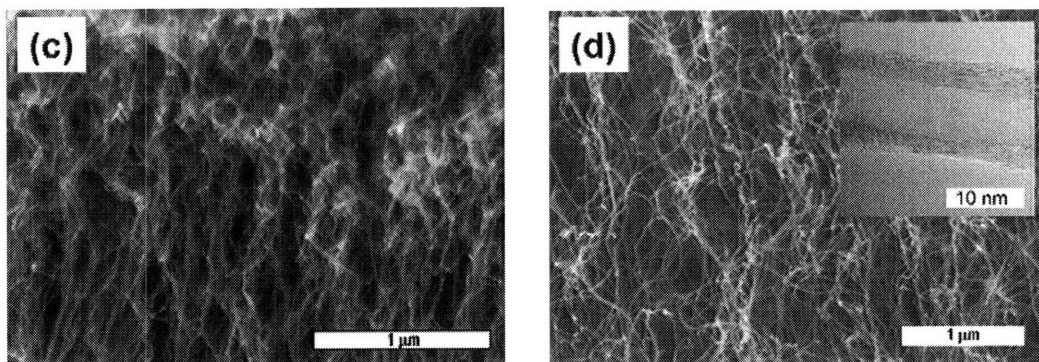


Figure A-6. Representative SEM micrographs of MWCNT films taken edge-on. Figure (a) is a micrograph of Sample 1, close to the substrate ($h = 0.2$ mm). Figure (b) is an image of Sample 1, taken from the middle of the film ($h = 0.9$ mm). Figure (c) is an image of Sample 1, taken near the top of the film ($h = 1.4$ mm). Sample 2 is shown ($h = 0.4$ mm) in Figure (d). HRTEM micrographs are shown inset reflecting typical CNT diameters.

In conclusion, this work has demonstrated that SAXS can be a very effective tool in studying the morphology of CNT thin films. This work demonstrated that SAXS is capable of quantifying both an average CNT diameter as well as the orientation of the CNTs within the thin film. In continuing work, SAXS will be used to study the mechanical manipulation of CNT thin films via uniaxial compression and solvent evaporation.

References

- 1) Hinds, B.J.; Chopra, N.; Rantell, T.; Andrews, R.; Gavalas, V.; Bachas, G. *Science* **2004**, *303*, 62.
- 2) Dresselhaus, M. S.; Dresselhaus, G.; Avouris, P. *Carbon Nanotubes: Synthesis, Structure, Properties, and Applications*; Springer: New York, 2001.

- 3) Baughman, R. H.; Zakhidov, A. A.; de Heer, W. A. *Science* **2002**, *297*, 787-792.
- 4) Huang, H.; Liu, C. H.; Wu, Y.; Fan, S. S. *Advanced Materials* **2005**, *17*, 1652.
- 5) Horibe, M.; Nihei, M.; Kondo, D.; Kawabata, A.; Awano, Y. *Japanese Journal of Applied Physics Part I* **2005**, *44*, 5309-5312.
- 6) Lau, K. K. S.; Bico, J.; Teo, K. B. K.; Chhowalla, M.; Amaratunga, G. A. J.; Milne, W. I.; McKinley, G. H.; Gleason, K. K. *Nano Letters* **2003**, *3*, 1701.
- 7) Wei, B.; Vajtai, R.; Choi, Y. Y.; Ajayan, P. M.; Zhu, H.; Xu, C.; Wu, D. *Nano Letters* **2002**, *2*, 1105.
- 8) Bendiab, N.; Almairac, R.; Sauvajol, J. L.; Rols, S.; Elkaim, E. *Journal of Applied Physics* **2003**, *93*, 1769.
- 9) Schaefer, D. W.; Zhao, J.; Brown, J. M.; Anderson, D. P.; Tomlin, D. W. *Chemical Physics Letters* **2003**, *375*, 369.
- 10) Brown, J. M.; Anderson, D. P.; Justice, R. S.; Lafdi, K.; Belfor, M.; Strong, K. L.; Schaefer, D. W. *Polymer* **2005**, *46*, 10854.
- 11) Burian, A.; Dore, J. C.; Hannon, A. C.; Honkimaki, V. *Journal of Alloys and Compounds* **2005**, *401*, 18.
- 12) Hough, L. A.; Islam, M. F.; Hammouda, B.; Yodh, A. G.; Heiney, P. A. *Nano Letters* **2006**, *6*, 313.

Appendix B Synthesis of Zinc Oxide Nanowires from Au Nanoparticle Arrays Created Using PS- *b*-PAA Micellar Thin Films

Recently there has been considerable progress in the synthesis of nanowires due to the novel properties that these one-dimensional nanoscale materials possess. ZnO nanowires have been demonstrated to exhibit room-temperature ultraviolet lasing, which could have substantial applications in fields such as optical computing, information storage, and microanalysis². ZnO nanowires are commonly synthesized via the vapor-liquid-solid (VLS) mechanism. In this mechanism, a Au thin film is placed in a reactor downstream of an alumina boat containing ZnO and graphite powder. A constant flow of argon between 800 - 1000 °C is then added to the reactor. The proposed mechanism for the reaction is explained elsewhere³. By using (110) sapphire substrate to support the Au thin film, vertical orientation of ZnO nanowires can be achieved through epitaxial growth³.

Because of the generality of our micellar approach for synthesizing arrays of inorganic nanoclusters, PS-*b*-PAA micellar thin films can be utilized to create Au nanocluster arrays for ZnO nanowire growth. This was achieved using the same procedure as described in Chapter 2 of this thesis, with a few minor adjustments. To create gold nanoclusters, the AuCl₃ was added to a solution of PS-*b*-PAA micelles in toluene. Because the loading of the micelles relies on the electrostatic interaction between the metal ion and the carboxylic acid group of the PAA unit, it is necessary to perform the loading in dark conditions to prevent the light-induced reduction of Au³⁺ to Au⁰. The

PS-*b*-PAA micellar thin film was submerged in a 7 mM AuCl₃ aqueous solution for between 18 – 24 hours. The thin film was then rinsed for 1 min in deionized water. Following rinsing, the film was reduced in H₂ at 80 °C for 24 – 72 hours. The film was then oxygen plasma etched for 12 minutes to remove the polymer thin film. The resulting Au nanocluster array is shown in Figure B-1.

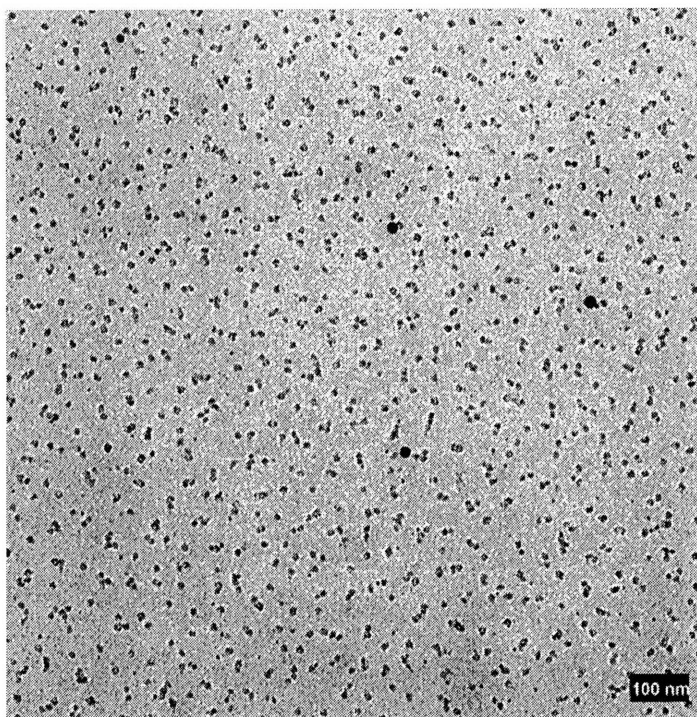


Figure B-1. TEM image of Au nanocluster arrays created from PS-*b*-PAA micellar thin film submerged in a 7 mM AuCl₃ aqueous solution.

The resulting Au nanocluster arrays were created on both a Si substrate and a sapphire (110) substrate. The substrates were then placed in a reactor and subjected to the ZnO nanowire growth conditions described previously. The resulting ZnO nanowires on a Si substrate are shown in the SEM image in Figure B-2.

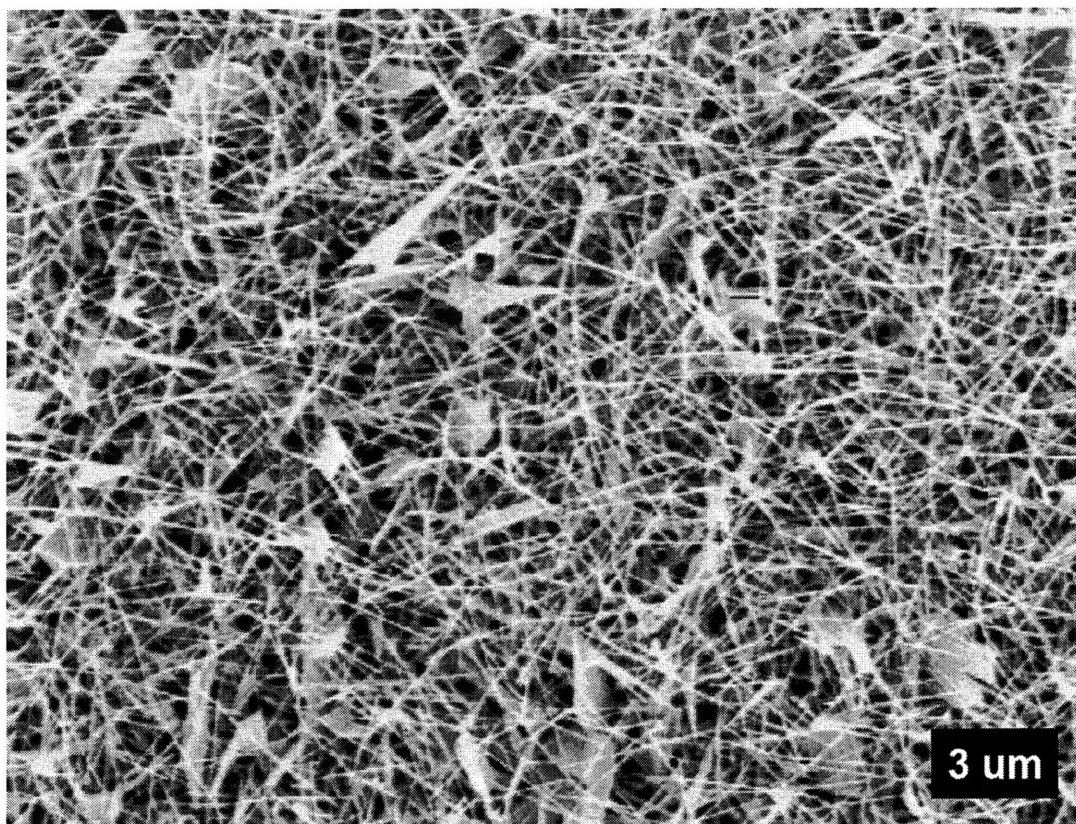


Figure B-2. SEM image of ZnO nanowires grown from PS-*b*-PAA templated Au nanoclusters on a Si substrate.

Through SEM characterization, the average diameter of the ZnO nanowires was determined to be approximately 50 nm. This is considerably larger than the original nanocluster diameter of approximately 10 nm prior to growth. It is well known that Au nanoclusters have considerable mobility at high temperatures, so it is likely that the Au nanoclusters coalesced during the growth to give larger Au nanoclusters that catalyzed ZnO nanowire growth. The apparent planes observed in Figure B-2 are referred to as “nanowalls”, and are also likely due to the rearrangement of the Au nanoclusters on the substrate.

In an attempt to create vertically aligned ZnO nanowires, the same growth conditions were applied to Au nanocluster arrays that were created on a sapphire (110) substrate. As shown in Figure B-3, the ZnO nanowires grow epitaxially from the sapphire substrate, resulting in primarily vertically-aligned ZnO nanowire arrays.

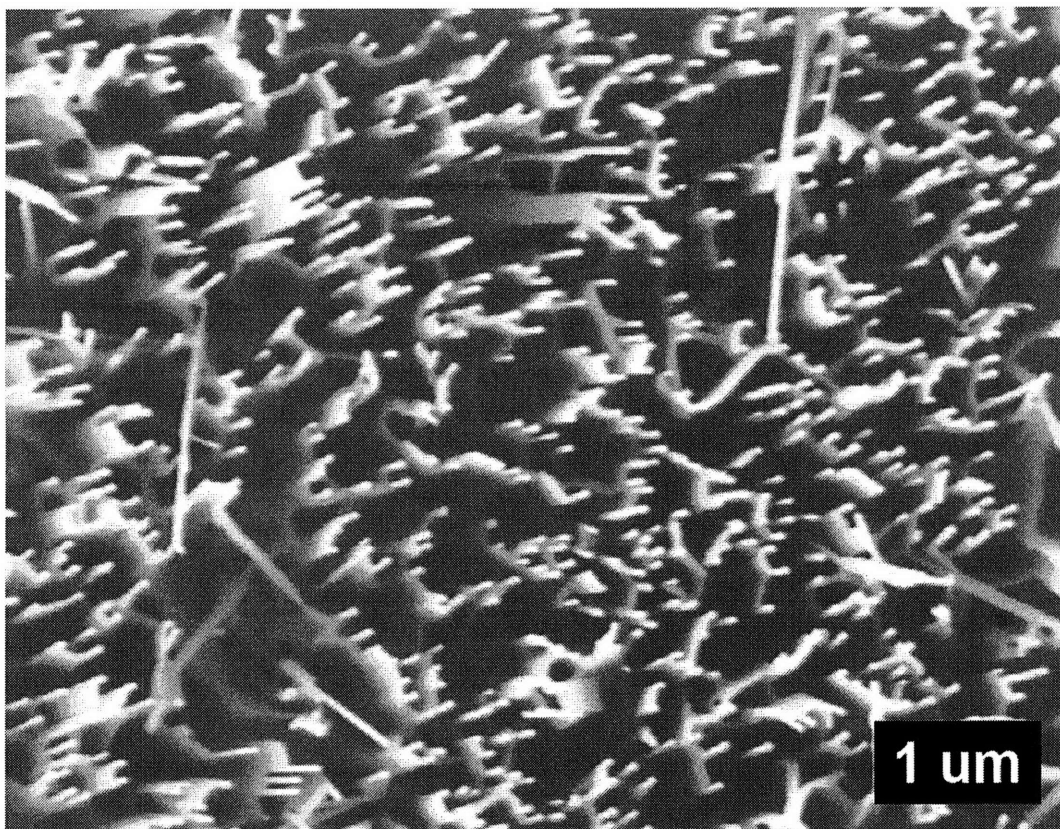


Figure B-3. SEM image of ZnO nanowires vertically grown from PS-*b*-PAA templated Au nanoclusters on a sapphire (110) substrate.

References

- 1) Huang, M. H. *et al.*, *Adv. Mater.* **2001**, *13*, 113 – 116.
- 2) Huang, M. H. *et al.*, *Science* **2001**, *292*, 1897 – 1899.
- 3) Yang, P. *et al.*, *Adv. Func. Mater.* **2002**, *12*, 323 – 331.

Appendix C Patterning of Block Copolymer Micelles and Inorganic Nanoclusters via the Self- Assembly of PS-*b*-PMMA

As demonstrated in this thesis, block copolymer micellar thin films can be used as templates to create quasi-hexagonally patterned inorganic nanocluster arrays. This system allows for the possibility of using the self assembly of a second block copolymer to pattern the original block copolymer micelles on a second length scale. The introduction to this approach was provided through work by Wang *et al.*¹, where PMMA homopolymer was added to a PS-*b*-PAA micellar toluene solution and then spin cast onto a substrate. Initially the PMMA homopolymer is fully miscible in the toluene solution. When the solution is spin cast and the toluene evaporates, the PMMA and the PS-*b*-PAA micelles phase separate to create an irregular and uncontrollable pattern of PS-*b*-PAA micelles on the micron length scale. In contrast, the idea for our work was to add PS-*b*-PMMA block copolymer, rather than PMMA homopolymer, to the PS-*b*-PAA micellar toluene solution. In this case, both blocks of PS-*b*-PMMA are soluble in toluene initially. Once spin casting occurs, the toluene will evaporate and the PS-*b*-PMMA will begin to phase separate. In this case, as opposed to the PMMA homopolymer case, the blocks of PS-*b*-PMMA are covalently bonded and will therefore exhibit traditional block copolymer self assembly. Because the PS-*b*-PAA micelles only expose PS units in toluene, the iron-loaded micelles should be sequestered in the PS region of the PS-*b*-PMMA morphology. This is demonstrated in the diagram in Figure C-1.

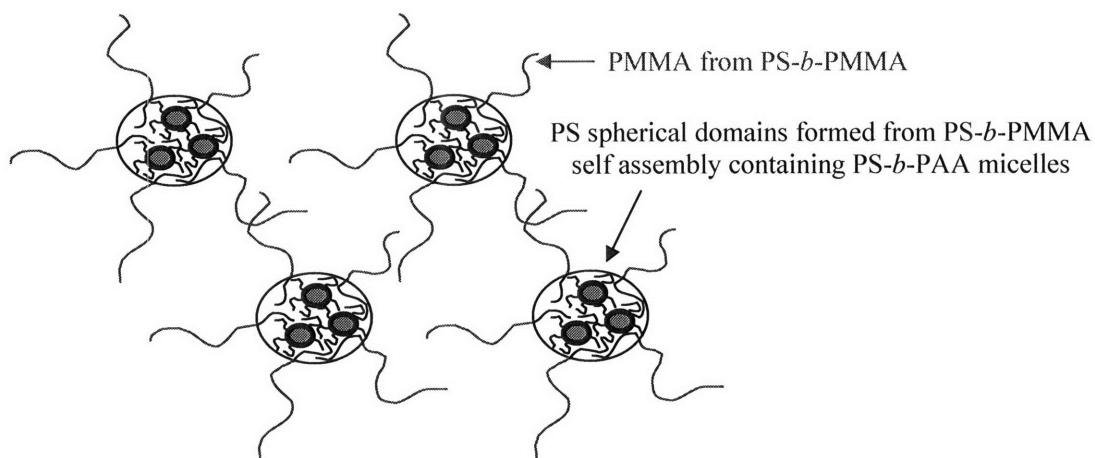


Figure C-1. Diagram illustrating the proposed utilization of the self assembly of PS-*b*-PMMA to pattern PS-*b*-PAA micelles on a nanometer length scale.

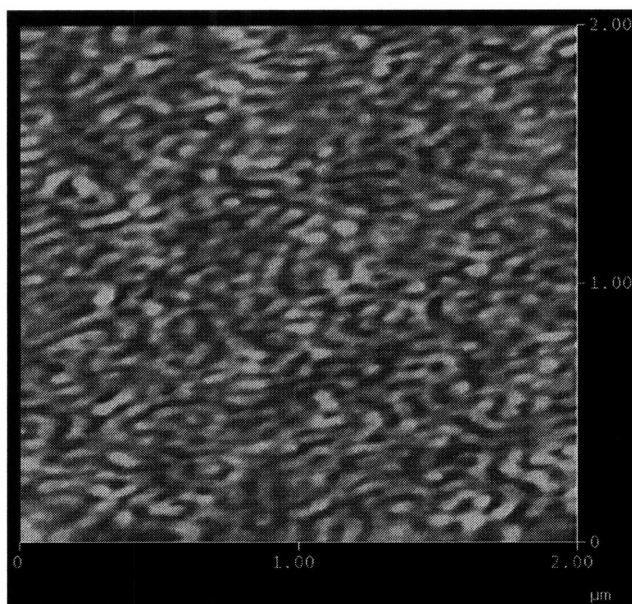


Figure C-2. AFM height image of a PS(170k)-*b*-PMMA(168k) thin film after spin casting onto a Si substrate.

The first PS-*b*-PMMA block copolymer used was PS(170k)-*b*-PMMA(168k). An AFM image of the resulting block copolymer thin film after spin casting is shown in

Figure C-2. The PS-*b*-PMMA thin film was then annealed in acetone vapor for 3.5 hours and 19 hours as shown in Figure C-3.

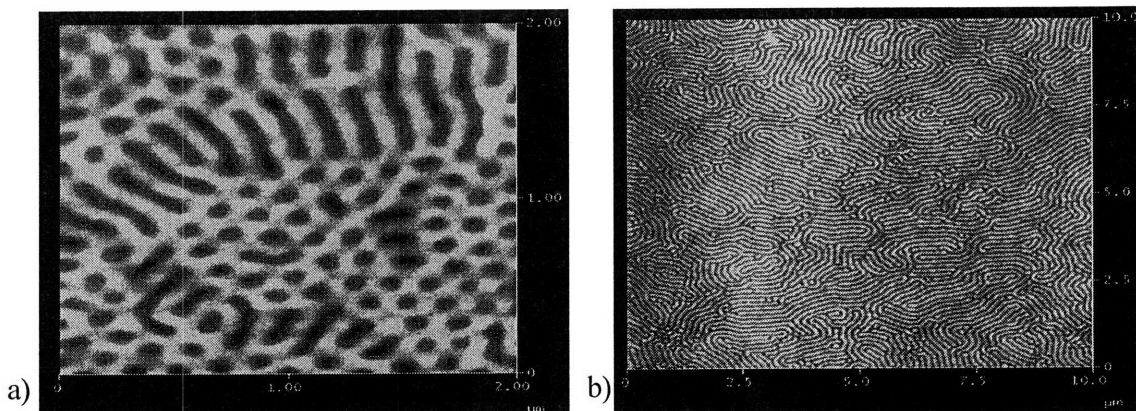


Figure C-3. AFM height image of a PS(170k)-*b*-PMMA(168k) thin film after spin casting onto a Si substrate and annealing in toluene for: a) 3.5 hours, b) 19 hours.

A solution of PS-*b*-PAA micelles in toluene (FeCl_3 loading ratio of 0.3) was then added to a PS-*b*-PMMA toluene solution. The molar ratio of [PS-*b*-PMMA / PS-*b*-PAA] was used to control the number of micelles within the block copolymer micellar thin films. In this experiment [PS-*b*-PMMA / PS-*b*-PAA] ratios of 25, 10, and 5 were used. After spin casting the solutions on a Si substrate, the films were characterized using AFM prior to acetone annealing. Figures C-4, C-5, and C-6 show AFM images of the as-cast films with [PS-*b*-PMMA / PS-*b*-PAA] ratios of 25, 10, and 5, respectively.

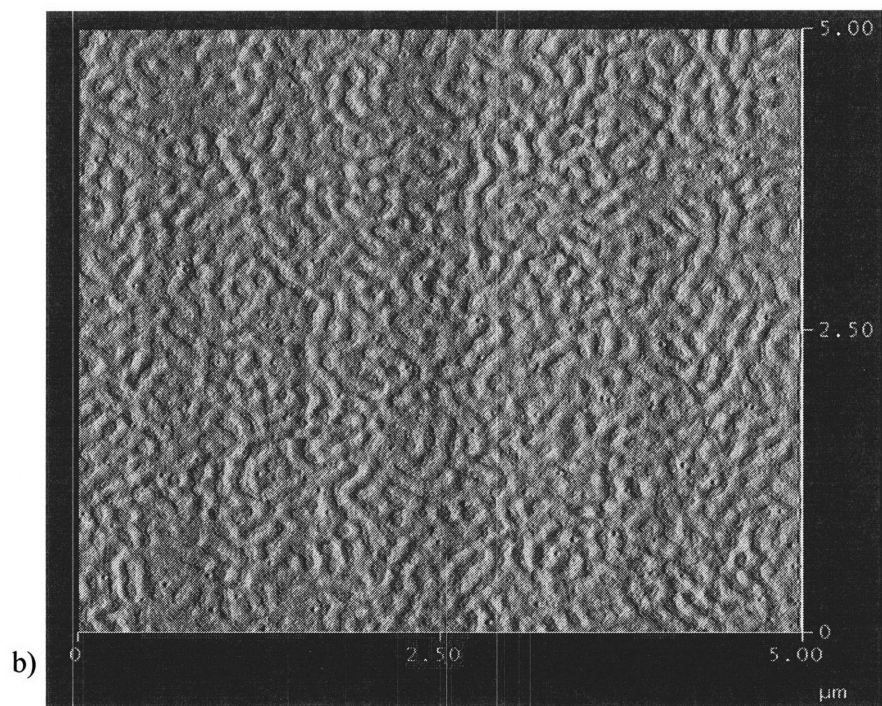
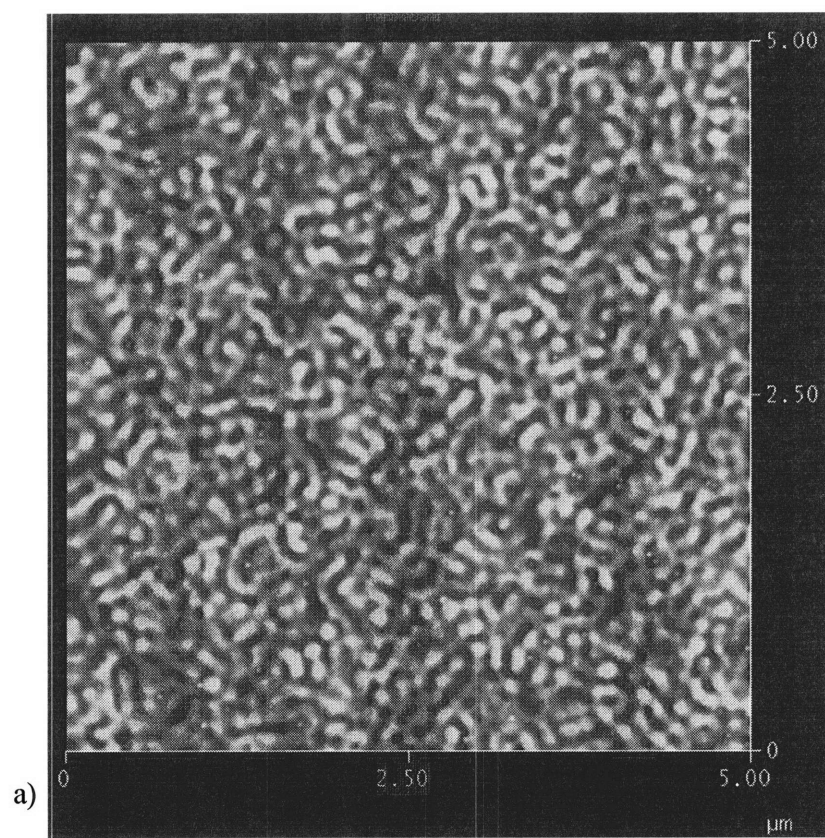
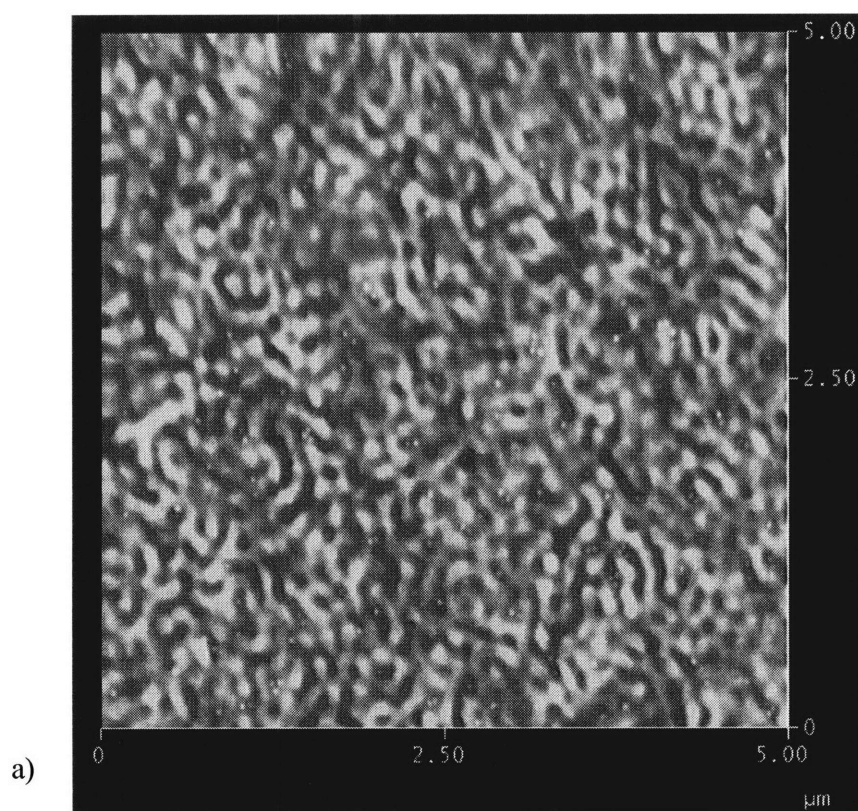


Figure C-4. AFM height (a) and phase (b) images of a PS(170k)-*b*-PMMA(168k) thin film loaded with PS-*b*-PAA iron loaded micelles with a ratio of [PS-*b*-PMMA / PS-*b*-PAA] = 25 after spin casting onto a Si substrate.



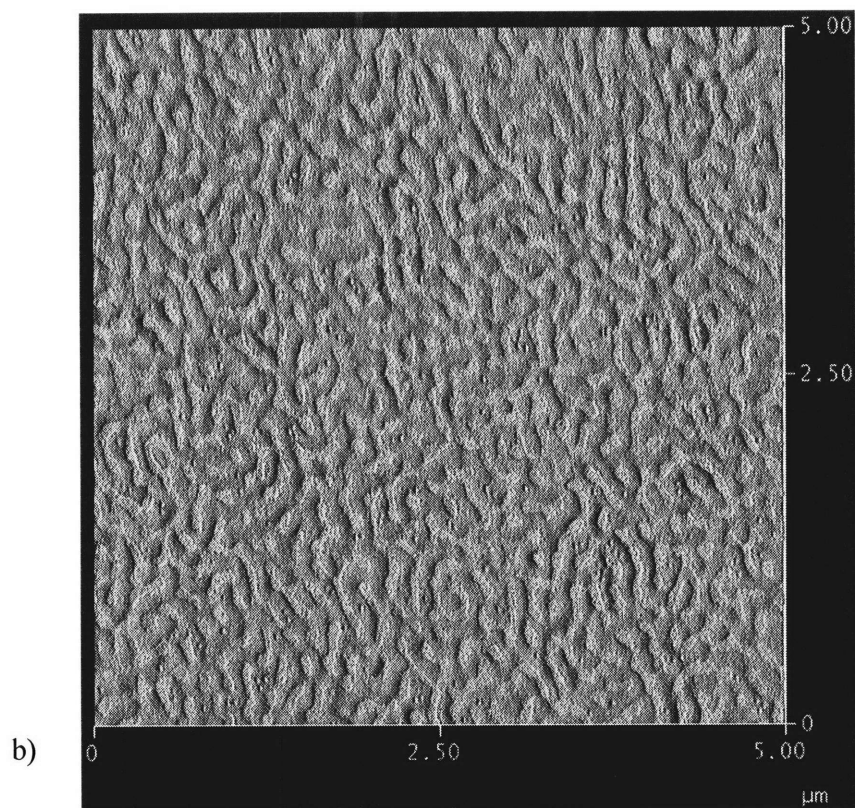


Figure C-5. AFM height (a) and phase (b) images of a PS(170k)-*b*-PMMA(168k) thin film loaded with PS-*b*-PAA iron loaded micelles with a ratio of [PS-*b*-PMMA / PS-*b*-PAA] = 10 after spin casting onto a Si substrate.

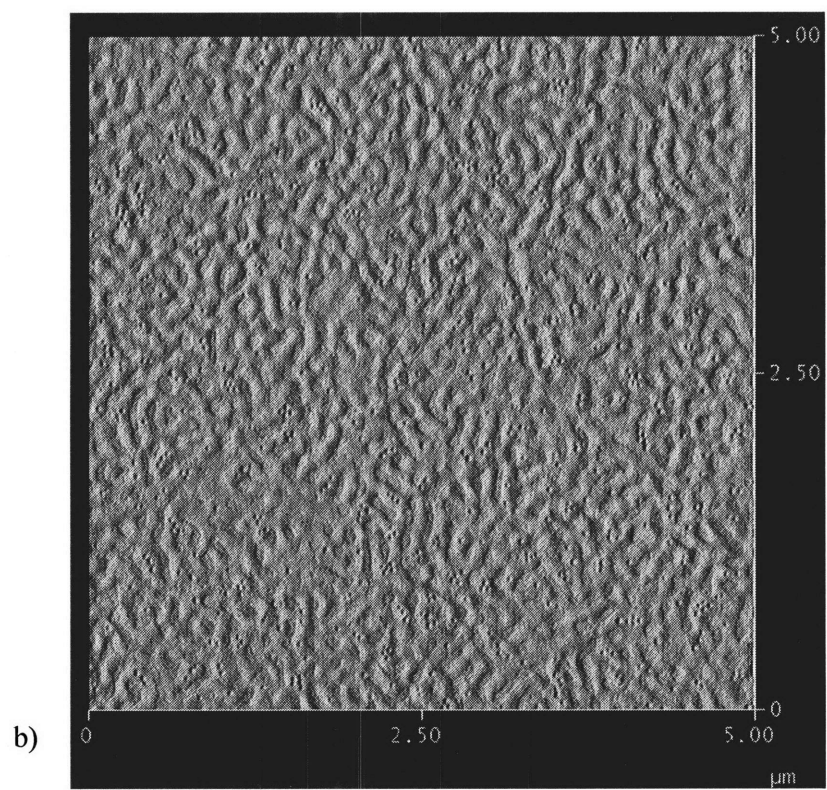
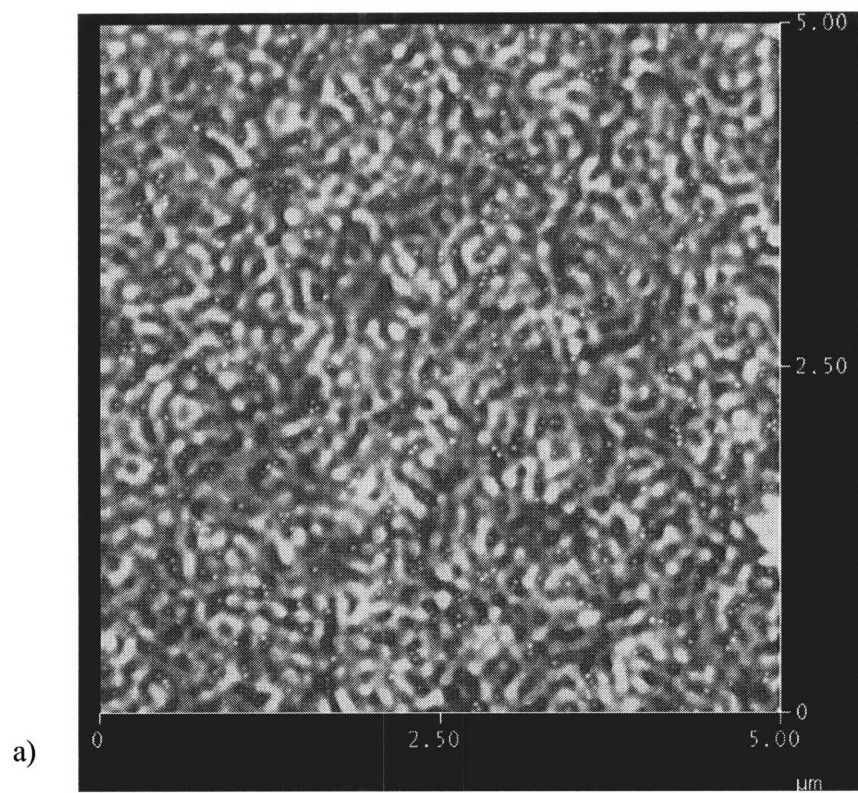


Figure C-6. AFM height (a) and phase (b) images of a PS(170k)-*b*-PMMA(168k) thin film loaded with PS-*b*-PAA iron loaded micelles with a ratio of [PS-*b*-PMMA / PS-*b*-PAA] = 5 after spin casting onto a Si substrate.

From Figures C-4, C-5, and C-6 it is clear that the circular dots on the AFM image are the iron-loaded PS-*b*-PAA micelles. This is supported by the following two observations: 1) the PS-*b*-PAA micelles are all sequestered within the PS phase of the PS-*b*-PMMA block copolymer, which appears red on the AFM images, and 2) as the ratio of [PS-*b*-PMMA / PS-*b*-PAA] is decreased the density of the dots clearly increases in the AFM images.

The next step of the experiment was to anneal the PS-*b*-PMMA thin films loaded with the PS-*b*-PAA micelles to create patterned arrays of PS-*b*-PAA micelles using the self assembly of PS-*b*-PMMA. Unfortunately the results we observed after annealing did not match our expected outcome. Figure C-7 shows an AFM image of the PS-*b*-PMMA film with a [PS-*b*-PMMA / PS-*b*-PAA] = 5 after acetone annealing for 3.5 hours. While the PS-*b*-PMMA self assembled into an equilibrium structure, there are very few iron loaded PS-*b*-PAA micelles in the image. We are unsure of the explanation for this and we suspect that through optimization of the annealing procedure the final goal could still be attained.

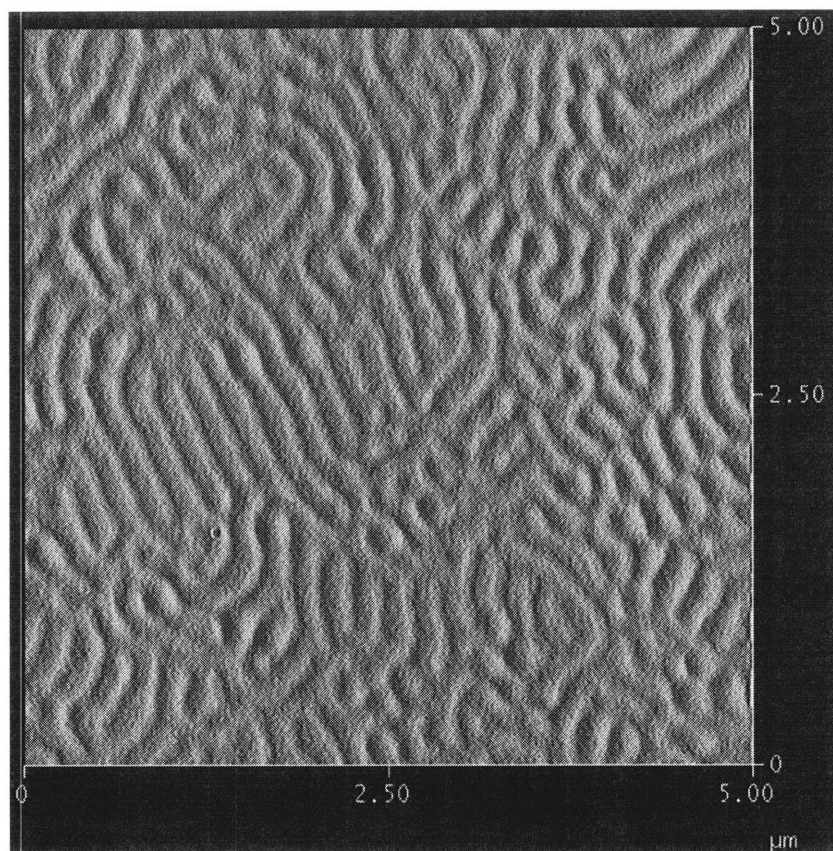


Figure C-7. AFM phase image of a PS(170k)-*b*-PMMA(168k) thin film loaded with PS-*b*-PAA iron loaded micelles with a ratio of [PS-*b*-PMMA / PS-*b*-PAA] = 5 after spin casting onto a Si substrate and annealing in acetone for 3.5 hours.

References

- 1) Wang, C. W.; Moffitt, M.G. *Chem. Mater.* **2005**, *17*, 3871 – 3878.

Appendix D Effects of Block Copolymer Micellar Thin Film Thickness on Inorganic Nanocluster Morphology

The thickness of the micellar thin film plays a critical role in the shape of the resulting nanoclusters. This effect is demonstrated using a PS-*b*-PAA micellar thin film loaded with a FeCl₃ loading ratio of 0.3 that was oxygen plasma etched for 12 – 15 minutes. In this appendix, PS-*b*-PAA will refer to PS(M_n = 16,400)-*b*-PAA(M_n = 4,500). Figure D-1 shows an area of the substrate where the micellar thin film was a monolayer prior to oxygen plasma etching. This leads to a quasi-hexagonal array of iron oxide nanoclusters on the substrate surface.

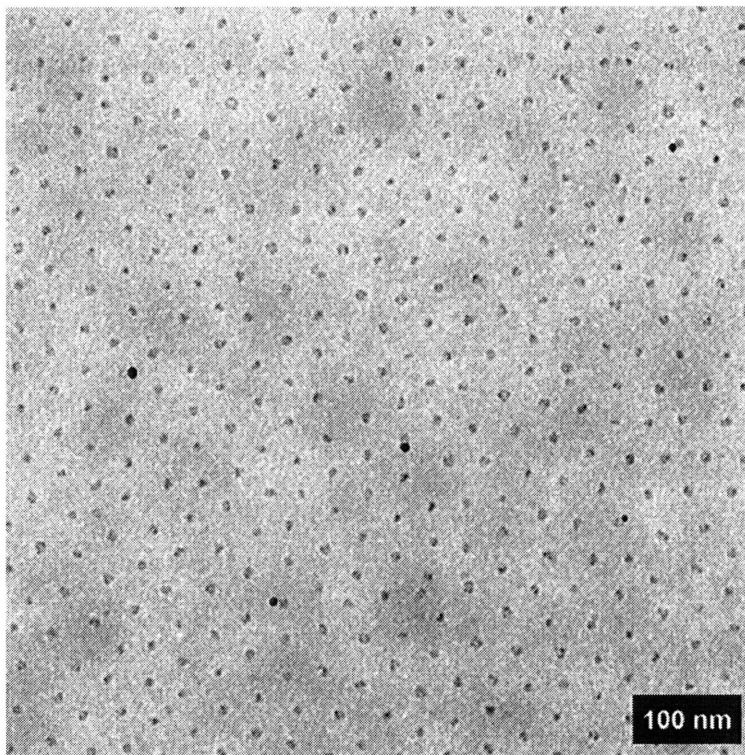


Figure D-1. TEM image of iron oxide nanoclusters synthesized from a monolayer of PS-*b*-PAA with a FeCl₃ loading ratio of 0.3.

As the thickness of the PS-*b*-PAA micellar thin film increases, the quasi-hexagonal arrangement is lost and the areal density of nanoclusters increases noticeably, as shown in Figure D-2. In this image the areal density has approximately doubled, which suggests that the PS-*b*-PAA micellar thin film was approximately twice the thickness of a PS-*b*-PAA monolayer (approximately 20 nm).

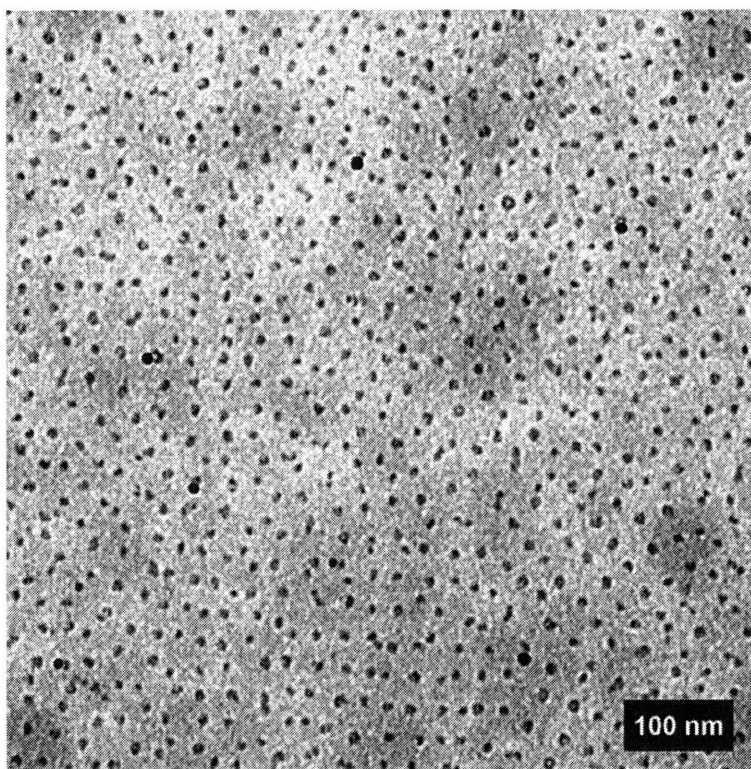


Figure D-2. TEM image of iron oxide nanoclusters synthesized from a bilayer of PS-*b*-PAA with a FeCl₃ loading ratio of 0.3.

When the thickness of the PS-*b*-PAA micellar thin films increases further, aggregation of the nanoclusters occurs and leads to the creation of large iron oxide

formations. This result is observed in the TEM image in Figure D-3 shown below. It is believed that the individual iron oxide nanoclusters fuse together to form aggregate structures as the PS-*b*-PAA micellar thin film is degraded by oxygen plasma etching.

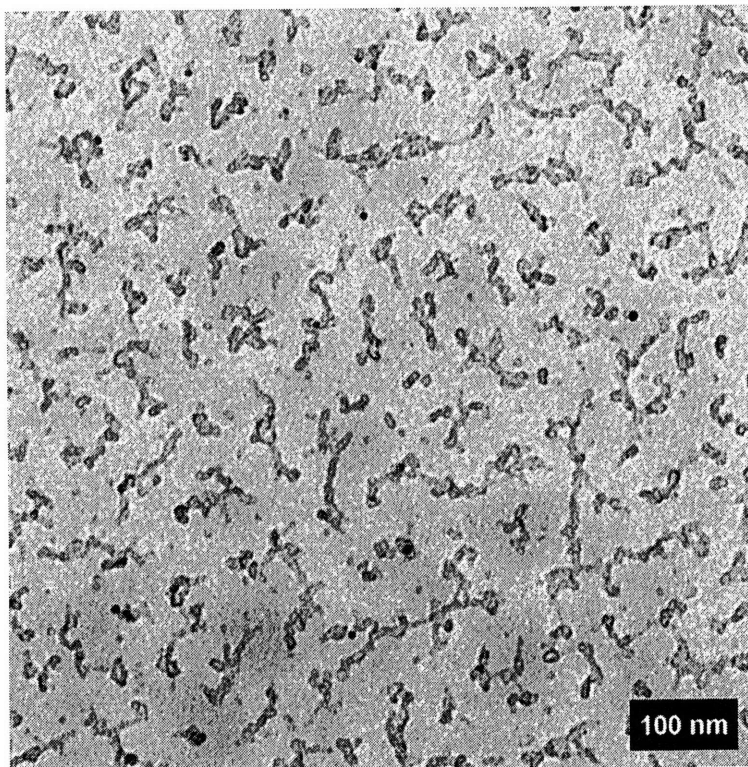


Figure D-3. TEM image of iron oxide nanoclusters synthesized from a PS-*b*-PAA micellar thin film with a thickness of at least four monolayers and a FeCl_3 loading ratio of 0.3.

This effect has also been observed using the PS-*b*-P2VP micellar system loaded with HAuCl_4 . Figure D-4 shows the typical gold nanocluster array created from a PS-*b*-P2VP monolayer thin film with a HAuCl_4 loading ratio of 0.35 after oxygen plasma etching. All PS-*b*-P2VP films in this appendix will be referring to PS($M_n = 81,000$)-*b*-P2VP($M_n = 21,000$).

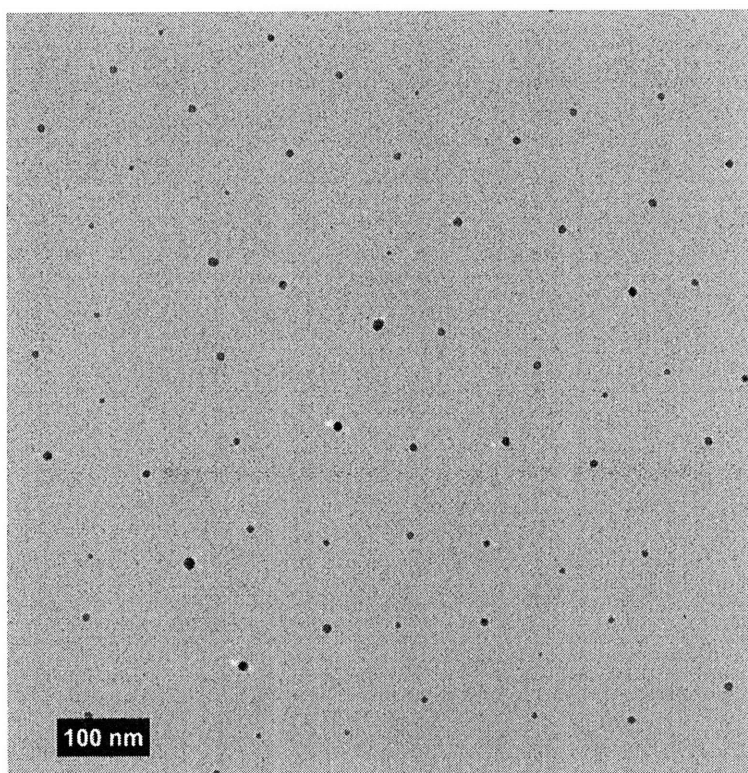


Figure D-4. TEM image of gold nanoclusters synthesized from a PS-*b*-P2VP monolayer micellar thin film with a HAuCl₄ loading ratio of 0.35.

Just as with the PS-*b*-PAA case, when the PS-*b*-P2VP micellar thin film becomes considerably thicker than the monolayer thickness the gold nanoclusters appear to fuse during the oxygen plasma etching process to form large gold aggregates. This is demonstrated in the TEM image in Figure D-5.

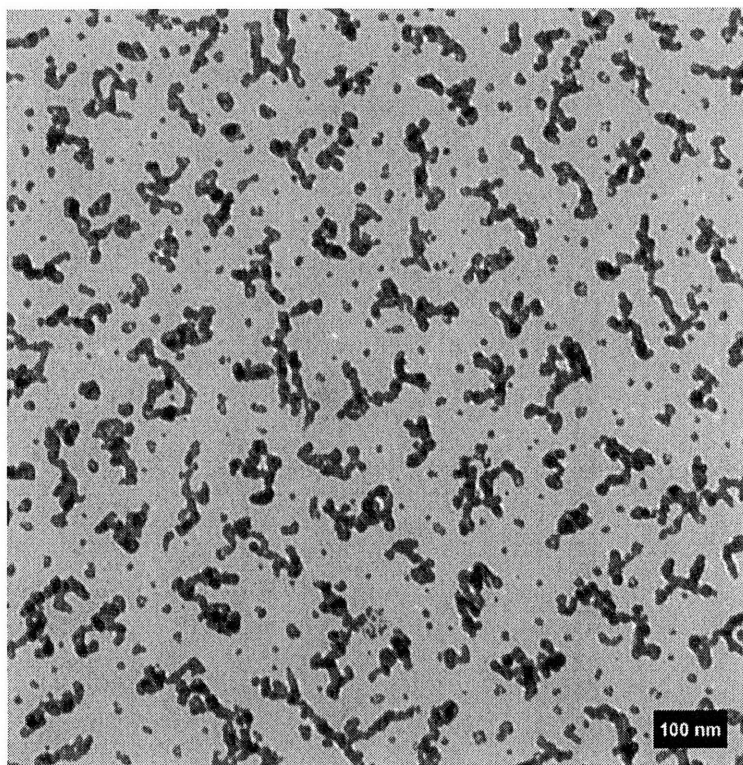


Figure D-5. TEM image of gold nanoclusters synthesized from a PS-*b*-P2VP micellar thin film with a thickness greater than four monolayers and a HAuCl₄ loading ratio of 0.35.

Appendix E Comparisons Between the Loading of PS- b-PAA Micelles in Aqueous or Toluene Solution

In Chapter 2 of this thesis, inorganic nanocluster arrays were created by spin casting PS-*b*-PAA micellar thin films onto a substrate. The micellar thin films were then submerged into an aqueous 0.5 mM FeCl₃ solution for 60 min, as described in Section 2.2.2. The resulting iron oxide nanoclusters were characterized using TEM as shown in Figure E-1.

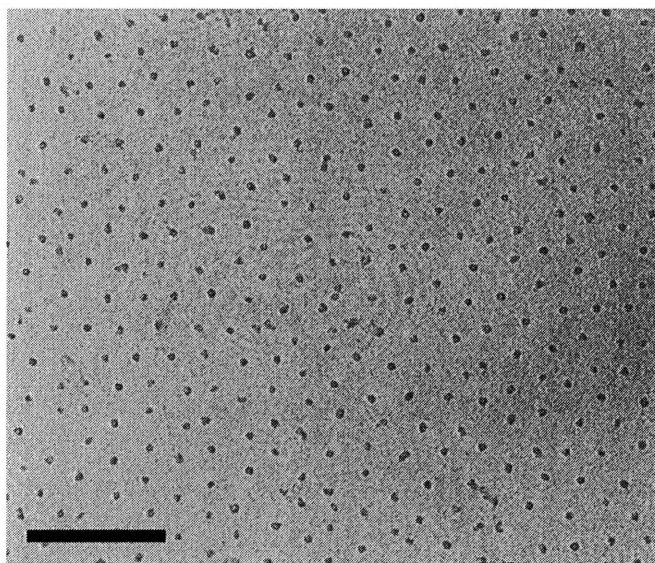


Figure E-1. TEM image of iron oxide nanocluster synthesized by submerging a PS-*b*-PAA micellar thin film into 0.5 mM FeCl₃ for 60 min.

When the PS-*b*-PAA micellar thin films were submerged into an aqueous 5 mM FeCl₃ solution for approximately 19 hours, large iron oxide aggregate structures were observed on the surface of the polymer thin film. The resulting TEM image of the iron oxide aggregates is shown in Figure E-2. It is believed that these iron aggregates are

formed in the aqueous FeCl_3 solution and then adsorb to the polymer surface. The formation of iron aggregates was found to be minimized by decreasing the concentration of FeCl_3 and by decreasing the dipping time of the substrate.

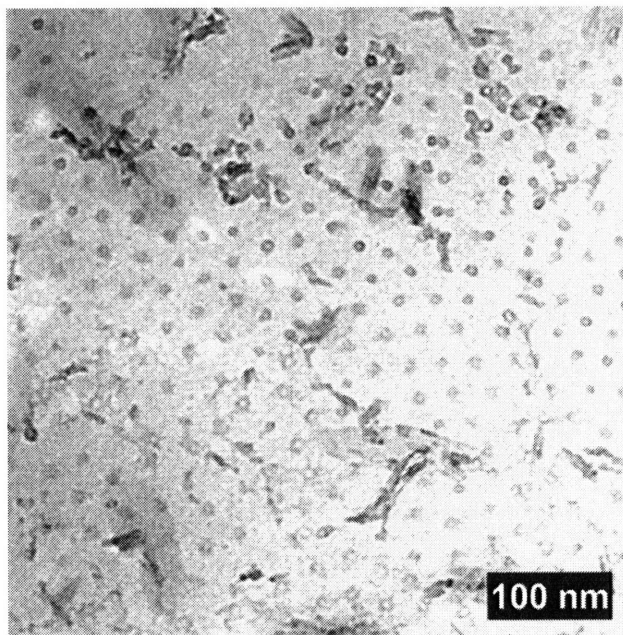


Figure E-2. TEM image of iron oxide nanocluster synthesized by submerging a PS-*b*-PAA micellar thin film into 5.0 mM FeCl_3 for 19 hours.

The composition of the aggregates was determined to contain iron using a scanning transmission electron microscope (STEM) with energy dispersive x-ray analysis.

Because of the difficulties associated with loading iron into the micellar thin films using aqueous FeCl_3 , beginning in Chapter 3 the FeCl_3 was loaded directly into the PS-*b*-PAA toluene solution prior to spin casting. This prevented the formation of iron aggregates and also allowed for controlling the size of the iron oxide nanoclusters by varying the metal loading ratio.

Appendix F Contrast of Various Metal Salts Loaded in PS-*b*-PAA Micellar Thin Films in TEM Imaging Using Si₃N₄ Substrates

Throughout this thesis the inorganic nanocluster arrays were synthesized on Si₃N₄ window grid substrates and then characterized using TEM imaging. It was observed that there were often differences in the contrast between different metal salts, and this appendix serves to highlight these observations. Lead acetate trihydrate (PbAc₂) was found to be a very effective metal salt for generating contrast in TEM imaging. This is not altogether surprising considering the atomic number of Pb relative to other common metal salts used. PbAc₂ was found to be effective for creating Pb-containing nanoclusters, as well as for staining the PAA region of the micellar thin film for TEM on the as-cast micellar thin films. In contrast, it was observed that while FeCl₃ is effective for the synthesis of iron oxide nanoclusters, it offers no contrast in TEM imaging for an as-cast micellar thin film. This can be explained by noting that the nanoclusters exposed to an oxygen plasma etch are converted to iron oxide, while the as-loaded micellar thin prior to oxygen plasma etching contains only Fe³⁺ ions. From our work using HAuCl₄, it appears that Au also offers significant contrast both as Au nanoclusters and within a micellar film prior to oxygen plasma etching.

It should also be noted that differences were observed between the various Si₃N₄ substrates that are commercially available. Throughout this thesis we primarily used the Si₃N₄ substrates with 200 μ m thick frames, 0.5 mm window size, and membrane window thickness of 100 nm. At certain points throughout the thesis we also used Si₃N₄ window

grids that were identical to the previously mentioned substrates except for a membrane window thickness of either 50 nm or 20 nm. As expected, as the membrane window thickness decreases, the number of scattered electrons from the beam decreases and the potential quality of the resulting TEM image increases. On the other hand, as the membrane window thickness decreases, the membranes become considerably more fragile, although still manageable. It was also observed that the membrane film thickness affected the spin casting process. Spin casting conditions that created reasonable micellar thin films on the Si_3N_4 substrates with 100 nm film thicknesses did not create acceptable micellar thin films on Si_3N_4 substrates with 20 nm film thicknesses. This cause of this disparity is unclear, but it might involve the differences in surface roughness or inherent stresses within the different Si_3N_4 film thicknesses.